# Simulation-Based Analysis of a Sabatier Reactor for Conversion of $CO_2$ into Renewable Natural Gas

by

Duo Sun

A thesis
presented to the University of Waterloo
in fulfillment of the
thesis requirement for the degree of
Master of Applied Science
in
Chemical Engineering

Waterloo, Ontario, Canada, 2016

## AUTHOR'S DECLARATION

I hereby declare that I am the sole author of this thesis. This is a true copy of the thesis, including any required final revisions, as accepted by my examiners.

I understand that my thesis may be made electronically available to the public.

## Abstract

Converting $CO_2$-rich waste streams such as raw biogas, landfill gas and power plant flue gas into synthetic fuels and chemicals will reduce greenhouse gas emissions, and provide revenue at the same time. One option is to convert $CO_2$ into $CH_4$ by hydrogenation via Sabatier reaction. This synthetic methane is renewable if the $H_2$ required for the reaction is generated via water electrolysis using solar and wind energy or hydroelectricity. However, to realize the potential of this approach, a number of technological challenges related to the Sabatier reactor design have to be resolved, including thermal management and catalyst deactivation. The high exothermic nature of the Sabatier reaction can lead to reactor overheating while high temperatures are unfavorable to the exothermic and reversible methanation process, resulting in low $CO_2$ conversions and methane production. In addition, catalyst coking deactivation due to filamentous carbon accumulation caused by methane cracking at high temperature can also lead to low methane production and short operation period. A simulation-based study of a Sabatier reactor was performed in order to optimize the removal of heat, while maximizing $CO_2$ conversion and $CH_4$ production and minimizing deactivation at the same time. The heat exchanger type packed bed reactor with internal cooling by a molten salt was simulated using a transient, pseudo-homogeneous mathematical model. Reactor performance was evaluated in terms of $CO_2$ conversion and $CH_4$ yield. The simulation results showed that feed temperature, feed flow rate and molten salt flow rate are the crucial parameters affecting the reactor performance and catalyst activity. For the optimized operating conditions, the model predicts $CO_2$ conversions and $CH_4$ yields above 90% at high reactor throughputs, with space velocities up to 10,000 $h^{-1}$. A preliminary techno-economic evaluation is provided and opportunities and challenges are outlined.



*Keywords*: $CO_2$ conversion; renewable natural gas; Sabatier reactor; packed bed reactor; catalyst deactivation

## Acknowledgements

My most incompetent gratitude is to my supervisors, Professor David Simakov for his continuous support and guidance during the course of my Master studies.

I would like to express my sincere gratitude to my supervisory committee members: Professor Mark Pritzker, Professor Ali Elkamel for their precious comments and suggestions.

My special thanks goes to my parents, my wife and all of my friends for their love, support and encouragement.

Finally, I also acknowledge the support of the Waterloo Institute of Sustainable Energy (WISE) through the WISE – Cisco Systems Smart Grid Research Fund.

# Table of Contents

# List of Figures

# List of Tables

# Nomenclature

| | |
|---|---|
| $a$ | activity factor |
| $a_r$ | reactor compartment surface-to-volume ratio, $m^{-1}$ |
| $a_c$ | coolant compartment surface-to-volume ratio, $m^{-1}$ |
| $A_c$ | total cross-sectional area of cooling tubes, $m^2$ |
| $A_j$ | pre-exponential factor of the rate coefficient of reaction *j*, units of $k_j$ |
| $B_j$ | pre-exponential factor of the adsorption coefficient of species *i*, units of $K_j$ |
| $C_i$ | molar concentration of species i, $mol/m^3$ |
| $C_t$ | total molar concentration, $mol/m^3$ |
| $C_{pc}$ | coolant heat capacity, kJ/(kg K) |
| $C_{pg}$ | gas heat capacity, kJ/(mol K) |
| $d$ | wall thickness, m |
| $d_p$ | catalytic pellet diameter, m |
| $D$ | diameter, m |
| $D_{ae}$ | effective axial diffusion coefficient, $m^2/s$ |
| $D_m$ | gas molecular diffusivity, $m^2/s$ |
| $E_j$ | activation energy of reaction *j*, kJ/mol |
| $G_{MS}$ | molten salt gravimetric (mass) flow rate, kg/s |
| $h_{nc}$ | natural convection heat transfer coefficient, $kJ/(m^2\ s\ K)$ |
| $h_w$ | effective wall heat transfer coefficient, $kJ/(m^2\ s\ K)$ |
| $\Delta H_i$ | adsorption enthalpy change of species *i*, kJ/mol |
| $k_{ae}$ | effective axial thermal conductivity, kJ/(m s K) |
| $k_j$ | rate constant of reaction *j* |
| $K_i$ | adsorption constant of species *i*, $bar^{-1}$ |
| $K_{j,eq}$ | equilibrium constant of reaction *j* |
| $L$ | reformer length, m |
| $LHV$ | lower heating value, kJ/mol |
| $N_c$ | coolant tubes number |
| $Nu$ | Nusselt number |
| $p_i$ | partial pressure of gaseous species *i*, bar |
| $P$ | reactor pressure, bar |
| Pr | Prandtl number |
| $P_{tf}$ | total feed gas pressure, bar |
| Re | Reynolds number |
| $R_j$ | rate of reaction *j*, mol/(kg s) |

| | |
|---|---|
| $R_g$ | gas constant, kJ/(mol K) |
| $SV$ | gas hourly space velocity, $h^{-1}$ |
| $t$ | time, s |
| $T$ | reactor temperature, K |
| $T_c$ | coolant temperature, K |
| $T_e$ | environment temperature, K |
| $U_w$ | overall effective wall heat transfer coefficient, kJ/($m^2$ s K) |
| $v$ | fluid velocity, m/s |
| $V$ | compartment volume, $m^3$ |
| $z$ | reactor length coordinate, m |

***Greek letters***

| | |
|---|---|
| $\varepsilon$ | catalyst bed porosity |
| $\phi$ | Thiele modulus |
| $\eta_j$ | effectiveness factor of reaction *j* |
| $\lambda$ | thermal conductivity, kW/(m K) |
| $\mu$ | viscosity, kg/(m s) |
| $\rho_c$ | coolant density, $kg/m^3$ |
| $\rho_g$ | gas molar density, $mol/m^3$ |
| $\rho_s$ | solid density, $kg/m^3$ |
| $\tau_b$ | catalyst bed tortuosity |

***Subscripts***

| | |
|---|---|
| *c* | coolant |
| *eff* | effective |
| *eq* | equilibrium |
| *f* | feed |
| *g* | gas |
| *HE* | heat exchange |
| *HL* | heat loss |
| *int* | initial |
| *nc* | natural convection |
| *p* | packed bed |
| *s* | solid |
| *r* | reactor |

# 1. Introduction

## 1.1 Problem statement and motivation

The intensive use of fossil fuels leads to growing $CO_2$ emissions that accelerate global warming. It is absolutely necessary to capture anthropogenic $CO_2$. Once captured, $CO_2$ can be stored (e.g., in geological formations) but this approach requires high capital and operating costs, hindering its widespread commercialization. The alternative to $CO_2$ storage is $CO_2$ conversion into synthetic fuels and chemicals that closes the artificial carbon cycle, and also provide additional revenues. Being a harmful greenhouse gas, $CO_2$ is also an excellent source of carbon, non-flammable and non-corrosive. Resources are abundant, including flue gases from coal- and natural gas-fired power plants, biogas and landfill gas (up to 40% $CO_2$) and off-gas streams in several industrial processes such as ammonia production and fermentation. Large resources of $CO_2$ exist in natural gas and oil production wells, which is typically flared or even vented into the atmosphere.

Since conversion of captured $CO_2$ into synthetic fuels and chemicals is an attractive avenue for reduction of $CO_2$ emissions, this topic has attracted the interest of many research groups around the world [1-3]. Many research efforts have focused on photochemical and electrochemical reduction of $CO_2$ in an aqueous environment using water as a source of $H_2$ for $CO_2$ reduction [1, 2]. This approach is apparently attractive as it only uses water and $CO_2$ as the starting materials and solar energy and (potentially) renewable electricity. However, photochemical $CO_2$ reduction has inherent limitations of solar energy utilization, while electro-chemical reduction of $CO_2$ has low efficiencies of electricity utilization. Both processes are limited by low $CO_2$ solubility in water and have severe diffusion limitations [1, 2]. Thermocatalytic conversion combines high

temperatures with the use of a heterogeneous catalyst, providing fast reaction rates and, therefore, allowing for large volume production [3].

One of the thermocatalytic routes is $CO_2$ methanation, also called the Sabatier reaction [3, 4]. The strongly exothermic Sabatier reaction, Eq. (1), is typically accompanied by the mildly endothermic reverse water gas shift, Eq. (2), and exothermic CO methanation, Eq. (3).

$$CO_2 + 4H_2 \rightleftarrows CH_4 + 2H_2O \qquad \Delta H^\circ_{298} = -164.9 \text{ kJ/mol} \tag{1}$$

$$CO_2 + H_2 \rightleftarrows CO + H_2O \qquad \Delta H^\circ_{298} = 41.2 \text{ kJ/mol} \tag{2}$$

$$CO + 3H_2 \rightleftarrows CH_4 + H_2O \qquad \Delta H^\circ_{298} = -206.1 \text{ kJ/mol} \tag{3}$$

Historically, methanation systems were designed for conversion of synthesis gas [5], but, recently, $CO_2$ was also considered as a feedstock for methanation [6]. The overall process is highly exothermic which requires efficient heat removal, in order to facilitate $CH_4$ production. In addition to this thermodynamic constraint, reactor overheating can also lead to fast catalyst deactivation by sintering and coking resulting in reduction of methane production, $CO_2$ conversion, and reactor service life. The nickel-based catalysts should be operated at temperatures below 550 °C to prevent their deactivation [6].

The actively-cooled packed bed reactor design can potentially provide a low-cost solution for single-pass $CO_2$ methanation process. However, improvement of the reaction heat removal efficiency and optimization of operating conditions are required to promote methane production and to prevent catalyst deactivation. In this study, a heat-exchanger type packed bed reactor is simulated using a mathematical model. The reactor is assumed to be internally cooled by molten salt flowing through multiple cooling tubes.

## 1.2 Project objectives

Recently reported modeling studies did not account for coolant temperature variations, assuming constant temperature of the heat transfer fluid [7, 8]. Such a situation is achievable only when the heat transfer fluid flow rate is very high [9]. On the other hand, process optimization will require minimization of the coolant flow rate to enhance the reactor performance. In the presented herein study, the heat-exchanger type Sabatier reactor cooled by a molten salt is investigated via numerical simulations in order to optimize the removal of heat, while maximizing $CO_2$ conversion and $CH_4$ production rate. Molten salts are advantageous over conventional heat carriers, such as steam and mineral oils, due to their ability to operate at higher operating temperatures, low working pressure, high density, high heat capacity and non-flammability [9].

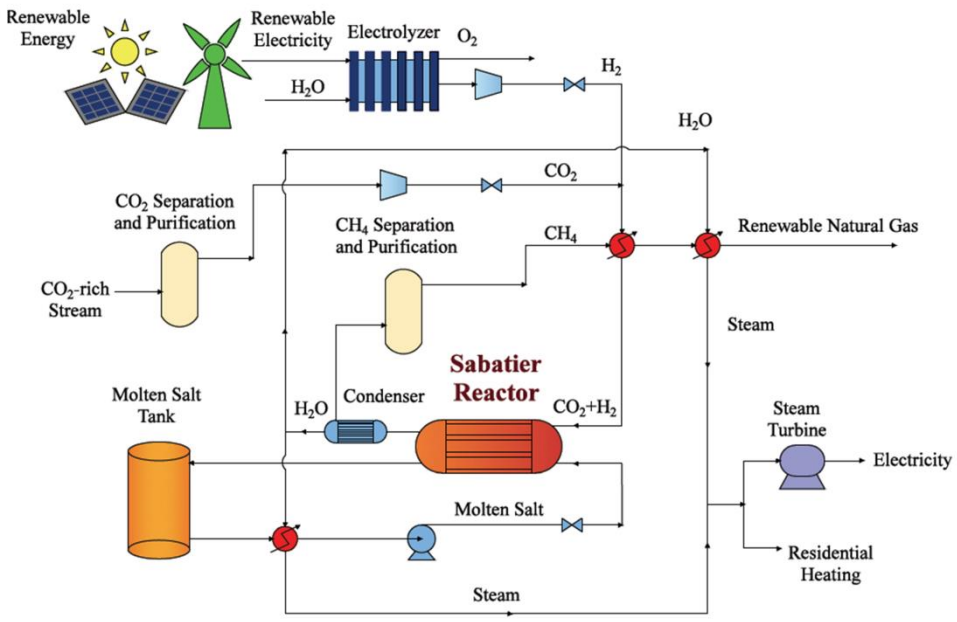


**Fig. 1.** Conceptual process flow diagram of the renewable natural gas generation system.

A conceptual representation of the complete $CO_2$ methanation system comprising such a reactor is shown in Fig. 1. The Sabatier reactor converts a mixture of $CO_2$ and $H_2$ into $CH_4$ and water. Hydrogen which is required for the Sabatier reaction can be generated using renewable energy [10, 11]. The reaction heat is removed from the reactor by the molten salt recirculation system which can be used to preheat the feed, and can be utilized as well for electricity generation and residential heating.

The project presented herein focused on the design and thermal management of the Sabatier reactor, which was evaluated in terms of $CO_2$ conversion and $CH_4$ yield as a function of operating parameters, such as feed temperature, feed flow rate and molten salt flow rate. In addition, the influence of catalyst deactivation on reactor performance was investigated and crucial parameters affecting reactor performance decay were identified.

## 2. Literature review

### 2.1 Methanation process and reactor design

Methanation of $CO_2$ has been studied for decades [12-14] but a number of technological issues remain to be resolved in order to make this technology economically viable. Because of the highly exothermic nature of the methanation reaction, reactor temperature control becomes a major concern in the design of methanation systems [15-18]. Several reactor designs and corresponding process concepts that focus on thermal management, cost efficiency and process flexibility have been proposed.

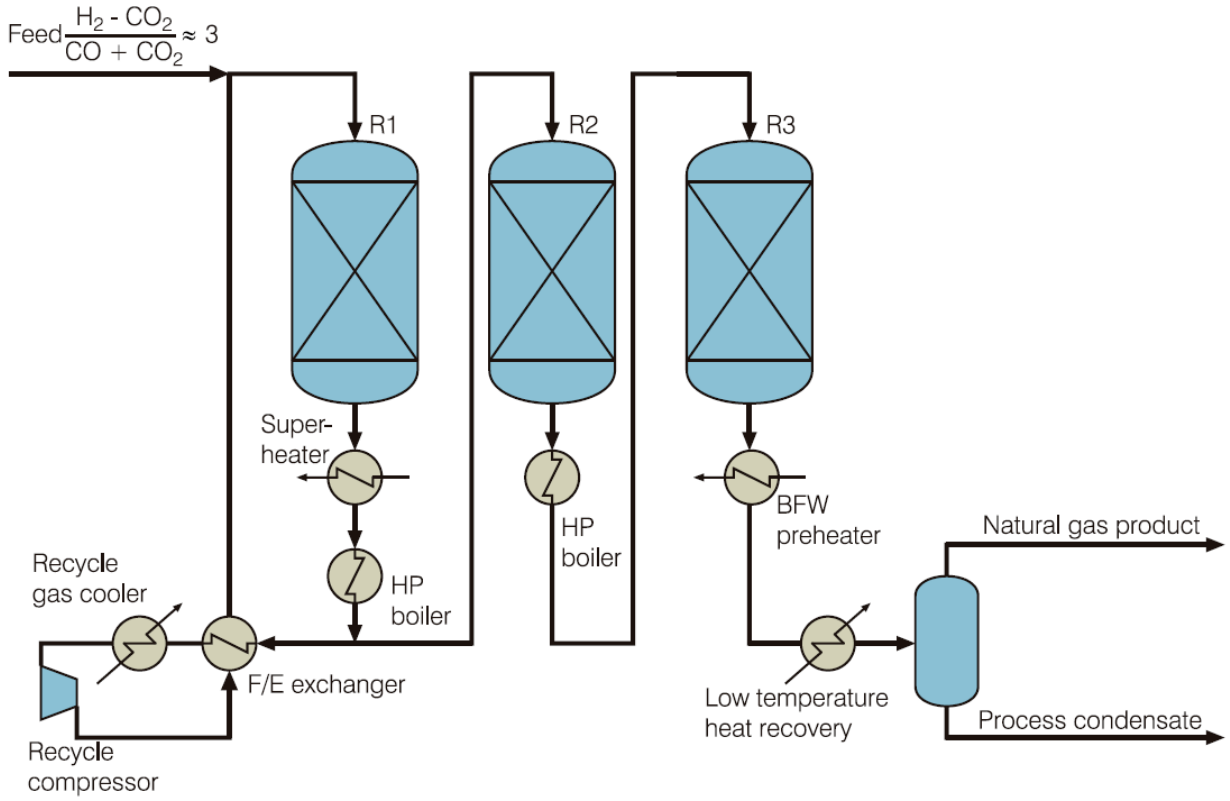


**Fig. 2.** Packed-bed reactors with intermediate cooling and gas recirculation (TREMP™). Adapted from [21].

A typical approach is the use of the adiabatic packed-bed reactor. Such systems are based on cascades of adiabatic reactors (typically 2-6) with intermediate cooling and sometimes gas recycling. A methanation unit including two adiabatic packed bed reactors with internal cooling and gas recirculation was developed by Lurgi company back in the 1960s and 1970s. Practical experience was gained by applying this technology in industry [19, 20]. In the 1980s, Haldor Topsøe developed a similar methanation process consisting of 3-4 instead of 2 packed-bed reactor. The so-called TREMP (Topsøe Recycle Energy-Efficient Methanation) system [21] is commercially available, shown in Fig. 2. In this process, gas recirculation is used for temperature control of the first methanation reactor, keeping the reactor temperature below 700 °C. The effluent gas exiting from the first reactor is cooled by a heat exchanger and fed into the subsequent methanation stages in order to maximize methane production. The process configuration and the number of reactors depends on the specific application. Capital cost investment and energy consumption for operation are main concerns.

Ralph M. Parson suggested a high temperature methanation concept (RMP process [22]) consisting of 4-6 adiabatic packed-bed reactors in series with steam addition and intermediate cooling between reactors. Another similar once-through methanation process (ICI/Koppers process) was proposed by Imperial Chemical Industries aiming to convert syngas from a Koppers-Totzek gasifier to synthetic natural gas [23, 24]. Steam addition prevents reactor from overheating. Methane production is promoted with respect to thermodynamic limits through intermediate cooling and a staged gas feed into the reactor. Though this technology was developed mainly for CO methanation, it could be adapted for $CO_2$ methanation with some modification on operating conditions.

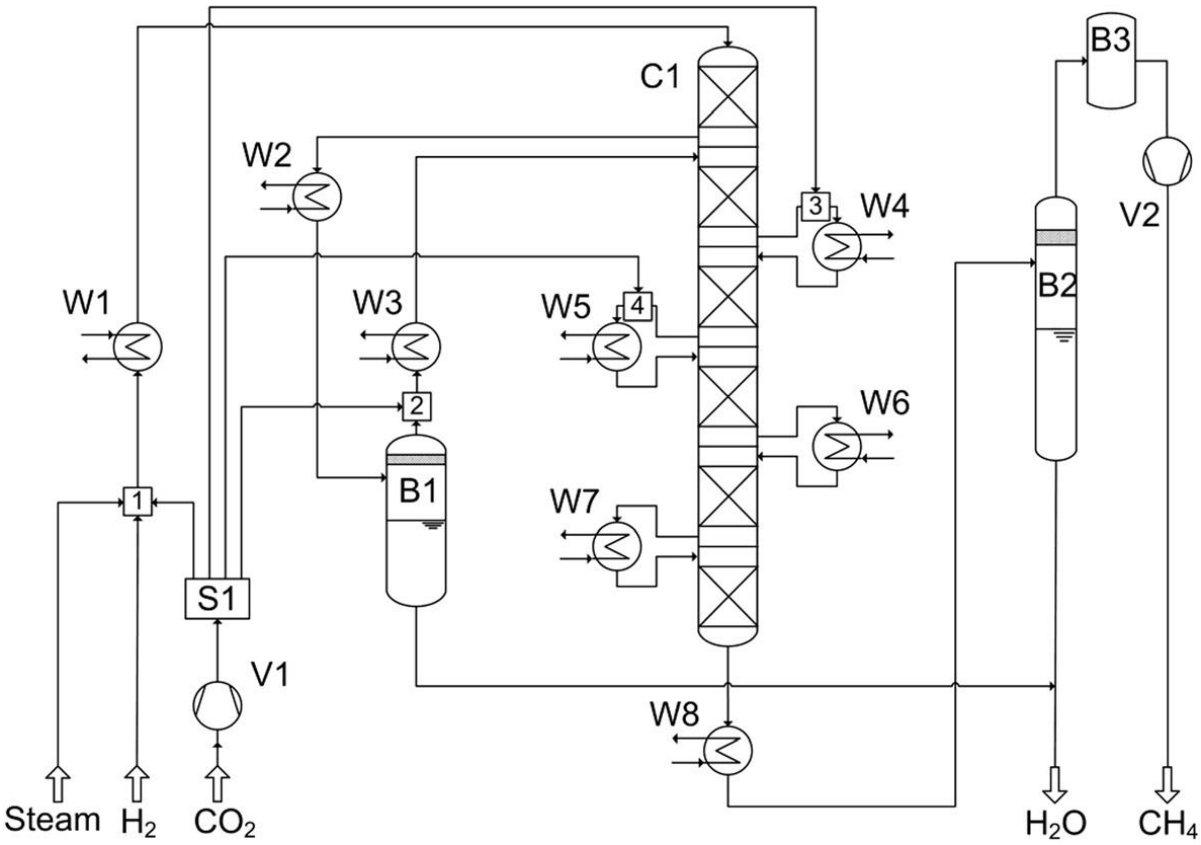


**Fig. 3.** Multiple-stage packed-bed reactor methanation system. Adapted from [6].

Despite a number of processes have been developed, widespread commercialization has not been realized. Recently, Schaaf et al. proposed a $CO_2$ methanation plant in which the process is divided into 6 reaction stages in series with inter-stage heat exchangers [6], as illustrated in Fig. 3. Temperature control is accomplished by intermediate gas coolers and staged gas feeding system. The four-stage feeding system distributes $CO_2$ in the feed gas in defined fractions to control the temperature of each stage below 550°C, so that gas recirculation devices are not necessary for the first-stage reactor. This concept still needs to be verified by practical implementation.

Although such systems can efficiently control the process temperature, the use of multiple reactors, recycle compressors, heat exchangers etc. result in system complexity and high capital cost investment. An alternative approach is to use a cooled packed-bed reactor [7, 8]. This method could potentially allow methanation to be conducted in a single-stage process, but heat removal optimization to avoid hot spot formation is a difficult task. Several alternative reactor designs have been suggested, aiming to achieve isothermal conditions. These alternative configurations include a heat-exchanger type packed-bed reactor with cooling tube bundles embedded in the catalytic bed [25], a structured microchannel reactor [26] and a honeycomb [27]. These methanation reactors have been developed to overcome the typical problem of temperature control and overheating in conventional packed-bed reactors. While isothermal operation makes the process design much simpler, the reactor itself becomes much more expensive because of the more complicated deposition of the metallic structure and the difficulty of replacing deactivated catalyst, especially for microchannel and honeycomb catalyst coating.

Fluidized-bed reactors are also widely suggested as ideal isothermal reactors due to the excellent mixing of gas and catalyst particles and efficient heat removal, which potentially allows for the use of a single reactor and a simple process to control [28-30], shown in Fig. 4 and Fig. 5. Since 1952, process design with fluidized–bed reactors has been investigated and between 1975 and 1986 a pilot methanation plant was built in Germany by Thyssengas and the University of Karlsruhe [31]. In this process, the problem of heat removal was resolved with a single fluidized-bed reactor instead of using multiple adiabatic packed-bed reactors. However, attrition and entrainment of the catalyst in fluidized-bed reactors caused by high mechanical stress between the catalyst particles and the reactor wall remains a major problem which has not been resolved yet

[32, 33]. Another disadvantage is that fluidized-bed reactors can only be operated in a narrow range of operating conditions dictated by the fluidization velocity, restricting reactor throughputs.

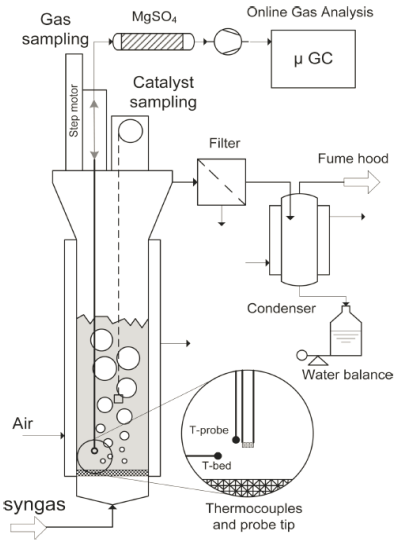


**Fig. 4.** A fluidized-bed methanation reactor experimental system. Adapted from [30].

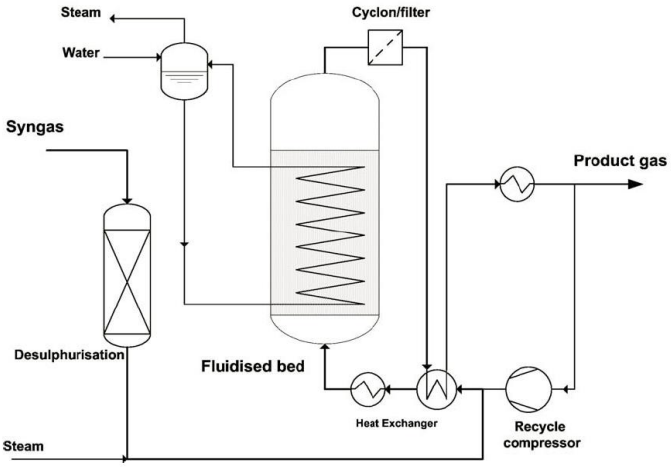


**Fig. 5.** A flow diagram of the methanation process based on a fluidized bed reactor. Adapted from [31].

Another proposed design is a three-phase methanation reactor [34, 35], e.g. a slurry reactor shown in Fig. 6. Among the major drawbacks related to this reactor design are the gas-to-liquid mass transfer resistance and the decomposition and evaporation of the heat transfer liquid. In 2014, Gtöz et al. [36] suggested an innovative methanation process combining a three-phase methanation (3PM) reactor with a honeycomb methanation (HCM) reactor, as illustrated in Fig. 7. The 3PM reactor can be operated nearly isothermally. The HCM reactor is used for producing methane that reach the requirements for

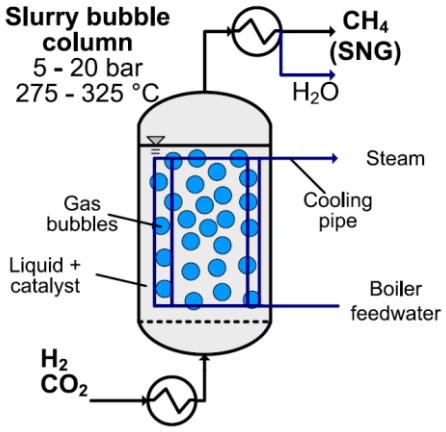


**Fig. 6.** Three-phase $CO_2$ methanation reactor. Adapted from [35].

injection into the gas grid without costly gas separation or recycle unit. Due to the tolerance to reactor load variations in the 3PM reactor, the system can be operated under both steady state and dynamic conditions.

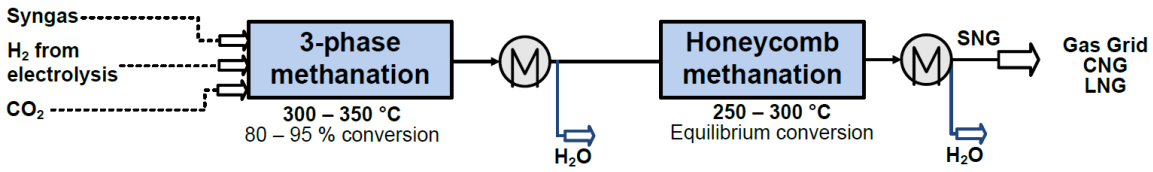


**Fig. 7.** The hybrid three-phase/honeycomb reactor methanation system. Adapted from [36].

In order to make the $CO_2$ methanation technology economically viable, the problems of thermal management and catalyst deactivation have to be resolved. One approach relies on the use of conventional packed-bed reactors, while resolving temperature control by intermediate cooling, gas recycle, and steam addition. This methodology involves a complicated system design and requires substantial capital and operating cost investments. An alternative approach for thermal management is the use of structured, fluidized-bed and three-phase reactors that can provide nearly-isothermal conditions. However, these reactor configurations incur significant transport limitations restricting the system throughput.

In this study, a heat-exchanger type Sabatier reactor is suggested, providing a low-cost solution for a single-pass methanation process due to system simplification and low capital cost investment. The reactor is cooled by a molten salt flowing through multiple tubes in order to optimize heat removal, while maximizing $CO_2$ conversion and $CH_4$ production rate. From the point of view of reduction of operating cost, we also suggested that the coolant flow rate be minimizing and the reactor performance be optimized.

## 2.2 Catalyst deactivation

Catalyst deactivation by poisoning, sintering and coking is another concern for Sabatier reaction [37]. The use of various catalysts and supports for $CO_2$ methanation has been extensively studied [38-42]. All metals located in groups 8-10 of the periodic table can catalyze the methanation reaction, with the activity decreasing in order Ru > Fe > Ni > Co > Mo and the selectivity order following a different trend: Ni > Co > Fe > Ru [43]. Accordingly, Ni-based catalysts are generally applied in commercial plants due to their relatively high activity, excellent selectivity and comparatively low price; γ-$Al_2O_3$ is typically used as a support, the γ-modification in particular [44]. However, Ni-based catalysts undergo serious deactivation by poisoning [37], sintering [45] or coking at high temperature [46].

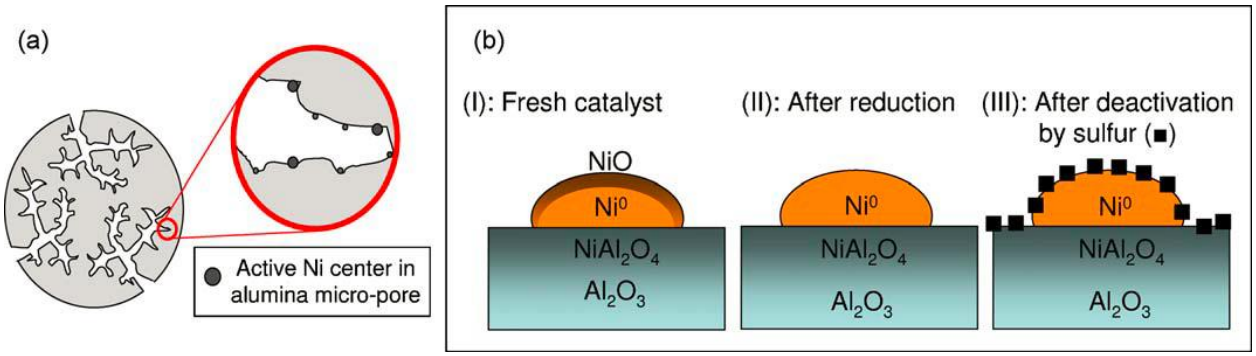


**Fig. 8.** The mechanism of sulphur poisoning of Ni/γ-$Al_2O_3$ catalyst. Adapted from [49].

Poisoning of Ni-based catalysts generally occurs in the presence of sulphur compounds in feed gas stream, e.g. $H_2S$ in biogas, due to the loss of catalyst active sites shown in Fig. 8. Relevant studies [47-49] have been conducted to investigate the deactivation of Ni-based catalysts. Poisoning deactivation can be prevented through desulfurization treatments. Along with poisoning, sintering of Ni-based catalysts also plays an important role in the deactivation [50], Fig. 9. Studies by Agnelli et al have indicated that sintering of catalyst proceeds by the formation of

$Ni(CO)_4$. This mechanism often called chemical sintering is quite unique as the rate of sintering decreases at higher temperatures [45].

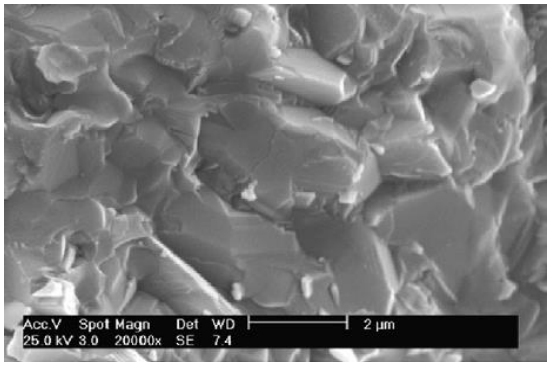


**Fig. 9.** SEM images of sintered catalyst. Adapted from [50]

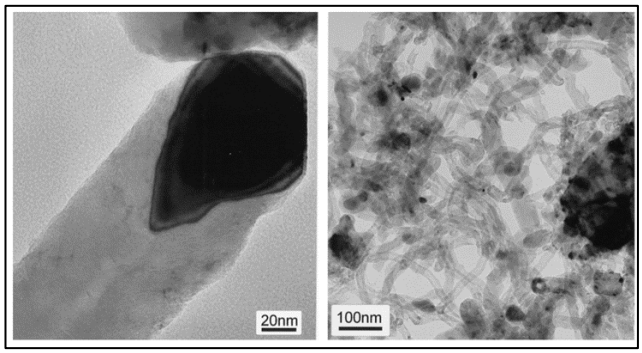


**Fig. 10.** TEM images of carbon fibers deposited on catalysts surface. Adapted from [51].

When operating in the temperature range generally employed for $CO_2$ methanation (700-800 K) and in the absence of catalytic poisons, the catalytic activity of Ni is mainly reduced by carbon deposition. Carbon deposition deactivates the catalyst by fouling the catalyst surface, blocking catalyst pores and disintegrating the catalyst support [37, 51], as illustrated in Fig. 10. The three major forms of carbon deposition on Ni-based catalyst are whisker-like carbon formed at temperatures greater than 450ºC, encapsulating hydrocarbon films formed by polymerization at temperatures below 500 ºC and pyrolytic carbon formed by cracking of hydrocarbons above 600 ºC [37]. The reactions leading to carbon deposition in the methanation process [52] are

Methane cracking

$$CH_4 \rightleftarrows C + 2H_2 \qquad \Delta H^{\circ}_{298} = -123.3 \text{ kJ/mol} \tag{4}$$

Boudouard reaction

$$2CO \rightleftarrows C + CO_2 \qquad \Delta H^{\circ}_{298} = -125.2 \text{ kJ/mol} \tag{5}$$

CO reduction

$$CO + H_2 \rightleftarrows C + H_2O \qquad \Delta H^{\circ}_{298} = -84.0 \text{ kJ/mol} \qquad (6)$$

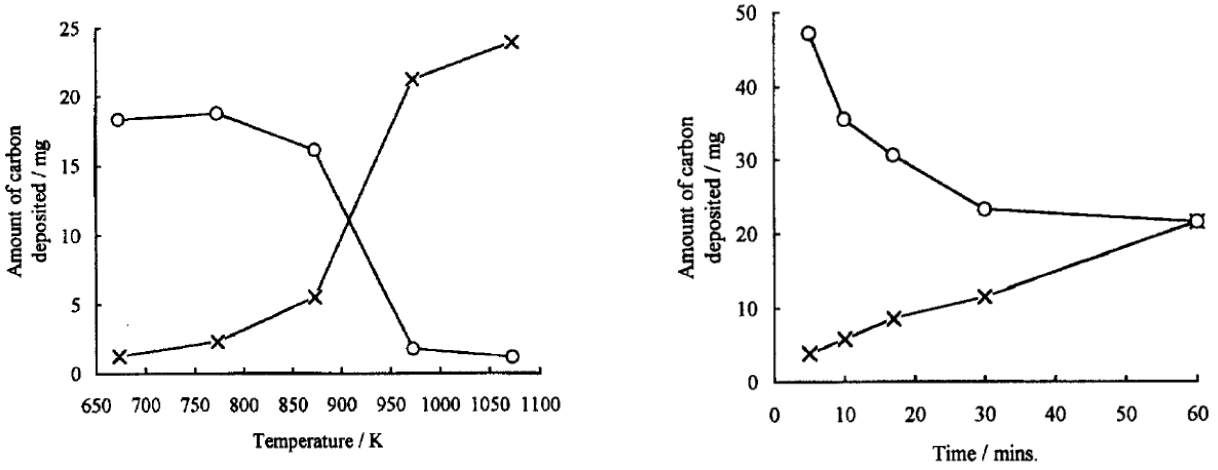


**Fig. 11.** The effect of temperature on (×) total amount of C deposited (mg) and (o) rate of C deposition (mg $h^{-1}$). Adapted from [53].

Claridge et al. investigated the effect of temperature on the rate of carbon deposition by the Boudouard reaction and methane cracking reaction, Fig. 11. Their results indicated that carbon deposition by methane cracking dominates at high temperature and the Boudouard reaction dominates at lower temperature with both process contributing equally to carbon formation at 890 K [53]. Other studies investigating the effect of different feed conditions have shown that low partial pressure of CO, high $CO_2$ partial pressure and high $H_2$/CO ratio reduce the rate of carbon formation by the Boudouard reaction. This indicate that the major cause of carbon deposition on Ni-based catalyst in the $CO_2$ methanation process is methane cracking [50, 54]. Analysis of the reaction mechanism involved in carbon deposition by methane cracking indicated that the rate limiting step in the process was the dissociative adsorption of methane on the catalyst with

hydrogen adsorption acting in competition. The rate of the reaction was found to depend on temperature and partial pressure of hydrogen and methane [55].

In recent years, methane cracking on Ni catalyst has been studied as a method to generate carbon nanotubes and hydrogen. The research in the development of carbon nanotubes has provided some interesting results. Nickel particles with an average size of 20-60 nm showed the greatest yield of carbon nanofibers [56]. These results are not surprising as it was reported previously that the thermodynamic equilibrium constant or the coking threshold during methane decomposition can be directly affected by the crystal size of nickel [57]. Addition of dopants [58] and the use of noble metal catalysts (e.g. Ru [59], Pt [60]) were also implemented to resolve catalyst deactivation issues.

In the present study, as the amount of CO formed during the course of $CO_2$ methanation was found to be almost negligible, we assume that the Boudouard reaction and CO reduction do not contribute to catalyst deactivation significantly. Thus the catalyst deactivation analysis focuses on $CH_4$ cracking. In order to minimize the effect of catalyst deactivation on reactor performance, while maximizing the $CH_4$ production and operation period duration (reactor lifetime), optimization of operating parameters is required. In this study, the reactor performance is analyzed as a function of parameters such as space velocity, cooling rate etc., during catalyst deactivation by $CH_4$ cracking.

## 3. Methodology

### 3.1 Model formulation

The suggested Sabatier reactor design is shown in Fig. 12. The reactor is a heat-exchanger type packed bed internally cooled by molten salt flowing in multiple cooling tubes. To minimize uncontrollable heat losses to the environment, the reactor is insulated by a layer of quartz wool. Both the external and internal tubes are made of stainless steel.

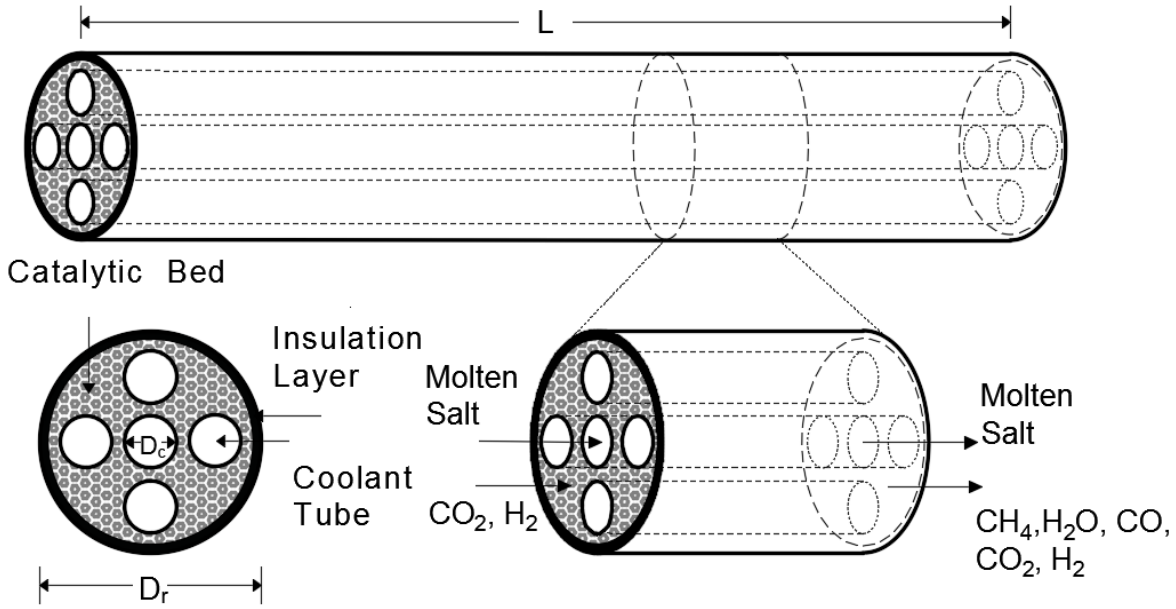


**Fig. 12.** Schematic of the molten salt-cooled, heat-exchanger type packed bed Sabatier reactor.

The dimensions used in numerical simulations are listed in Table 1. In order to minimize the heat transfer distance, the minimum number of cooling tubes was set to $N_c = 12$. For the dimensions described in Table 1 and evenly distributed tubes, the distance between any two adjusted cooling tubes will be $19 \pm 1$ mm for $N_c = 12$. Thermal conductivity of the packed bed should prevent large

radial gradients over that relatively small distance [61]. The maximum of $N_c = 22$ was set to allow space for catalytic pellets. Due to the high thermal conductivity of the molten salt, significant radial gradients are not expected to develop within the coolant tubes ($D_c = 0.02$ m) [9].

**Table 1.** Reactor dimensions

| $D_r$ (m) | $D_c$ (m) | $d_w$ (m) | $d_{iw}$ (m) | $d_p$ (m) | $N_c$ | L (m) | $V_{PB}$ ($m^3$) | $V_{MS}$ ($m^3$) |
|---|---|---|---|---|---|---|---|---|
| 0.2 | 0.02 | 0.002 | 0.05 | 0.003 | 12-22 | 1 | 0.0255 | 0.0041 |

*$D_r$ and $D_c$ denote the diameter of the packed bed ($D_r$) and coolant ($D_c$) compartments. L is the reactor length and $N_c$ is the number of the molten salt coolant tubes. $d_w$ denotes the thickness of the reactor wall and cooling tube, correspondingly; $d_{iw}$ is the insulation layer thickness. V denotes the volume of the packed bed ($V_{PB}$) and coolant (molten salt) ($V_{MS}$) compartments; $d_p$ is the catalytic pellet diameter.*

A transient, one-dimensional, pseudo-homogeneous mathematical model [62, 63] was used to simulate the reactor. As opposed to assuming constant coolant temperature [7, 8], the model accounts for temperature variations in the heat transfer fluid. The model also includes axial mass and heat dispersion and for the temperature dependence of thermo-physical properties, and the following assumptions are made to simplify analysis:

(1) All species in the gas mixture are ideal gas.

(2) Negligible radial mass and heat dispersion.

(3) The catalyst particles are assumed to be spherical with a diameter $d_p$ and the packed bed is treated as a porous medium with homogenous porosity $\varepsilon$.

(4) The gas mixture flowing in the reactor is treated as plug-flow.

Component mass balance and energy balance for the packed bed compartment are given by Eq. (7) and Eq. (8), respectively; the temperature distribution in a single molten salt tube is described by Eq. (9). The corresponding boundary and initial conditions are listed in Eqs (10, 11). Pressure drop was calculated using Ergun equation, Eq. (12), with a fixed inlet pressure (adjusted by a back pressure regulator in a practical situation). Variations in the gas velocity due to change in number of moles are considered by Eq. (13) [64]. Effective heat capacity in Eq. (8) is defined by Eq. (14); $N_c$ is the number of cooling tubes.

$$\varepsilon \frac{\partial C_i}{\partial t} = D_{ae} \frac{\partial^2 C_i}{\partial z^2} - \varepsilon v_g \frac{\partial C_i}{\partial z} + a\rho_s (1-\varepsilon) \sum_j \eta_j R_{ij} \tag{7}$$

$$\begin{aligned} &(\rho C_p)_{eff} \frac{\partial T}{\partial t} = k_{ae} \frac{\partial^2 T}{\partial z^2} - \varepsilon \rho_g C_{pg} v_g \frac{\partial T}{\partial z} + \\ &+ a\rho_s (1-\varepsilon) \sum_j (-\Delta H_j) \eta_j R_j - U_{w,HE} a_{r,HE} (T - T_c) - U_{w,HL} a_{r,HL} (T - T_e) \end{aligned} \tag{8}$$

$$\rho_c C_{pc} \frac{\partial T_c}{\partial t} = \lambda_c \frac{\partial^2 T_c}{\partial z^2} - \rho_c C_{pc} v_c \frac{\partial T_c}{\partial z} - U_{w,HE} a_{c,HE} (T_c - T) \tag{9}$$

$$\begin{aligned} z = 0 \qquad & \varepsilon v_g (C_{i,f} - C_i) = -D_{ae} \frac{\partial C_i}{\partial z} \qquad & z = L \qquad & \frac{\partial C_i}{\partial z} = 0 \\ & \varepsilon \rho_g v_g C_{pg} (T_f - T) = -k_{ae} \frac{\partial T}{\partial z} & & \frac{\partial T}{\partial z} = 0 \\ & \rho_c v_c C_c (T_{c,f} - T_c) = -\lambda_c \frac{\partial T_c}{\partial z} & & \frac{\partial T_c}{\partial z} = 0 \end{aligned} \tag{10}$$

$$\begin{aligned} t = 0 \qquad & C_i(0,z) = C_{i,\text{int}} \\ & T(0,z) = T_{\text{int}} \\ & T_c(0,z) = T_{c,\text{int}} \end{aligned} \tag{11}$$

$$\frac{dP}{dz} = -150 \frac{(1-\varepsilon)^2 \mu_g}{d_p^2 \varepsilon^3} v_g - 1.75 \frac{(1-\varepsilon)\rho_g}{d_p \varepsilon^3} v_g^2 \qquad P(0) = P_{tf} \tag{12}$$

$$v_g(z) = v_{gf} \frac{\sum_i C_i(z)}{\sum_i C_{i,f}} \tag{13}$$

$$(\rho C_p)_{eff} = \varepsilon \rho_g C_{pg} + (1-\varepsilon)\rho_s C_{ps} \tag{14}$$

### 3.2 Reaction kinetics

Reaction rates are calculated using the commonly adopted kinetics for methane steam reforming over the $Ni/Al_2O_3$ catalyst [65, 66], Eqs (15a-c). These kinetic expressions account for the reversibility of the reforming and water gas shift reactions and can be used therefore for modeling of the $CO_2$ methanation reaction system, Eqs (1-3). All parameters are tabulated in the Tables A.1 in Appendix [67]. Intraparticle and interphase transport limitations can be neglected for the size of catalytic pellets used in our simulations ($d_p$ = 3 mm, Table 1) [63].

$$R_3 = \frac{k_3}{p_{H_2}^{3.5}} \left( p_{CH_4} p_{H_2O}^2 - \frac{p_{H_2} p_{CO_2}}{K_{3,eq}} \right) \frac{1}{\text{den}^2} \tag{15a}$$

$$R_2 = \frac{k_2}{p_{H_2}} \left( p_{CO} p_{H_2O} - \frac{p_{H_2} p_{CO_2}}{K_{2,eq}} \right) \frac{1}{\text{den}^2} \tag{15b}$$

$$R_1 = \frac{k_1}{p_{H_2}^{2.5}} \left( p_{CH_4} p_{H_2O} - \frac{p_{H_2}^3 p_{CO}}{K_{1,eq}} \right) \frac{1}{\text{den}^2} \tag{15c}$$

$$\text{den} = 1 + K_{CO} p_{CO} + K_{H_2} p_{H_2} + K_{CH_4} p_{CH_4} + \frac{K_{H_2O} p_{H_2O}}{p_{H_2}}$$

$$k_j = A_j \exp\left( \frac{-E_j}{R_g T} \right) \qquad K_i = B_i \exp\left( \frac{-\Delta H_i}{R_g T} \right)$$

The internal effectiveness factor was calculated using the standard expression for a spherical pellet [68], with the Thiele modulus defined for each reaction in terms of the corresponding rate constant $k_j$ in Eq. (15):

$$\eta_j = \frac{3}{\phi_j}\left(\frac{1}{\tanh\phi_j} - \frac{1}{\phi_j}\right) \qquad \phi_j = \sqrt{\frac{\hat{k}_j d_p^2}{4D_m}}$$

$$\hat{k}_1 = \frac{k_1\rho_s(1-\varepsilon)}{\sqrt{P_{tf}}\,\rho_g\varepsilon} \qquad \hat{k}_2 = \frac{k_2\rho_s(1-\varepsilon)P_{tf}}{\rho_g\varepsilon} \qquad \hat{k}_3 = \frac{k_3\rho_s(1-\varepsilon)}{\sqrt{P_{tf}}\,\rho_g\varepsilon} \tag{16}$$

### 3.3 Deactivation kinetics

An activity factor is used to account for the change of the reaction rate as a function of time due to catalyst deactivation, assuming that the reaction rate of the fresh catalyst is a maximum. The activity factor is defined as:

$$a(t) = \frac{\text{actual reaction rate}}{\text{reaction rate with fresh catalyst}} \tag{17}$$

A general form of the activity factor equation is described by Eq. (18):

$$-\frac{da}{dt} = r_d a^d \tag{18}$$

Various catalyst deactivation models have been developed and reported in the literature. A random carbon deposition model was developed by Chen et al. [69] to determine the catalyst activity factor from measurement of the concentration of deposited coke on the catalyst:

$$a = \exp\left(-\alpha_C C_k\right) \tag{19}$$

$C_k$ is the concentration of deposited coke on the catalyst (g/g of catalyst). The deactivation constant $\alpha_C$ is 28.8 g of catalyst/g of coke. Models for determination of $C_k$ can be found in the relevant

literature[70, 71]. Other models for the activity factor were obtained by determination of the deactivation rate, assuming various deactivation orders, as given in Eq. (20) [72] and Eq. (21) [73]:

$$a = \left(1 - 1.2 r_d t\right)^{-1.2} \tag{20}$$

$$a = \left( \frac{1}{1 - 0.5 k_d \left( k_{d,C} + k_{d,CH_4} P_{CH_4} + k_{d,H_2} P_{H_2}^{0.83} \right) t} \right)^{-0.8} \tag{21}$$

In the presented herein (*Section 4.4*) analysis of the effect of the catalyst deactivation on the reactor performance, the deactivation expression developed by Borghei et al. (2010) [55] was employed. Assuming 1st order deactivation ( $d = 1$ ) [55] and integrating Eq. (18), a simple form of the activity factor expression can be derived:

$$a = \exp\left(-r_d t\right) \tag{22}$$

$$r_d = k_d P_{CH_4}^{\alpha} P_{H_2}^{\beta} \qquad \alpha = 1.8;\ \beta = -1.9 \qquad k_d = k_{d0} \exp\left( \frac{-E_d}{R_g T} \right) \tag{23}$$

As mentioned in the literature review on catalyst deactivation (*Section 2.2*), deactivation of the commercial Ni-based catalyst is mainly caused by the accumulation of filamentous carbon on the catalytic surface. The source of this carbon is mainly methane cracking that occurs at relatively high temperature. The reverse direction of the methane cracking, Eq. (4), is also considered in the catalyst deactivation expression above, Eq. (23). This process of carbon hydrogenation is expected to affect the catalyst activity via carbon removal and, therefore, regeneration. To sum up, the catalyst deactivation rate in Eq. (23) is a function of temperature, and the partial pressures of $CH_4$ and $H_2$; the dependence on partial pressures is calculated using an empirical power law expression [74]. Values of all corresponding parameters are tabulated in the Table A. 2 in Appendix[55].

### 3.4 Transport coefficients

The effective axial mass dispersion coefficient is calculated using the following correlation [75]:

$$D_{ae} = \varepsilon\left(\frac{D_m}{\tau_b} + 0.5 d_p v_g\right) \qquad \tau_b = \frac{1}{\varepsilon^{0.5}} \tag{24}$$

The expression for the effective axial heat dispersion coefficient ($k_{ae}$), Eq. (25), was derived from the heat conductivity correlations developed for catalytic fixed beds [62, 76, 77]. Values of $k_{ae}$ were calculated using original correlations [76, 77] in the relevant range of parameters, plotted versus particle Reynolds number ($Re_p$), and fitted using least squares analysis, resulting in the following correlation:

$$k_{ae} = \lambda_g\left(8 + 0.05\,\mathrm{Re}_p^{1.09}\right) \qquad \mathrm{Re}_p = \frac{v_g \rho_g d_p}{\mu_g} \tag{25}$$

Wall heat transfer coefficients are determined using the resistance-in-series approach:

$$U_{w,HE} = \left(\frac{1}{h_{wr}} + \frac{d_w}{\lambda_w} + \frac{1}{h_{wc}}\right)^{-1} \tag{26a}$$

$$U_{w,HL} = \left(\frac{1}{h_{wr}} + \frac{d_w}{k_w} + \frac{d_{iw}}{k_{iw}} + \frac{1}{h_{nc}}\right)^{-1} \tag{26b}$$

The wall heat exchange coefficient between the catalytic bed and the coolant tube, $U_{w,HE}$, accounts for resistances of the fixed bed, the coolant tube wall, and the molten salt, Eq. (26a). Similarly, the correlation for the wall heat loss coefficient, $U_{w,HL}$, accounts for resistances through the catalytic bed, the reactor wall, the quartz wool insulation layer (Fig. 12) [78], accounting also for natural convection ($h_{nc}$) [79]. Since the insulation layer natural convection resistances are dominant in Eq. (26b), the wall heat loss coefficient was nearly constant in all simulations: $U_{w,HL} \approx 0.01$ W/(m$^2$ K).

The effective wall heat transfer coefficient for the reaction compartment ($h_{wr}$) is estimated using the following correlation obtained in the similar way as Eq. (25), using a complete set of the original correlations [62, 63, 76, 77]:

$$Nu_p = \frac{h_{wr} d_p}{\lambda_g} = 24 + 0.34\,\mathrm{Re}_p^{0.77} \qquad \mathrm{Re}_p = \frac{v_g \rho_g d_p}{\mu_g} \tag{27}$$

The effective wall heat transfer coefficient for the coolant tube ($h_{wc}$) is estimated using the following correlations [80-82]:

$$\mathrm{Re}_c < 2030 \qquad Nu_c = 3.66 + \frac{0.065\,\mathrm{Re}_c\,\mathrm{Pr}_c (D_c / L)}{1 + 0.04[\mathrm{Re}_c\,\mathrm{Pr}_c (D_c / L)]^{2/3}} \tag{28a}$$

$$2030 < \mathrm{Re}_c < 4000 \qquad Nu_{wc} = 0.012(\mathrm{Re}_c^{0.87} - 280)\,\mathrm{Pr}_c^{0.4}\left[1 + (D_c / L)^{2/3}\right] \tag{28b}$$

$$\mathrm{Re}_c > 4000 \qquad Nu_c = 0.027\,\mathrm{Re}_c^{0.8}\,\mathrm{Pr}_c^{1/3} \tag{28c}$$

$$Nu_{wc} = \frac{h_{wc} D_c}{\lambda_c} \qquad \mathrm{Re}_c = \frac{v_c \rho_c D_c}{\mu_c} \qquad \mathrm{Pr}_c = \frac{C_{pc} \mu_c}{\lambda_c}$$

### 3.5 Numerical procedure

The model was solved using the MATLAB PDE solver with a second-order accurate spatial discretization based on a fixed set of user-specified nodes and time integration done by the stiff ODE solver (ode 15s). Dependences of thermophysical properties (density, viscosity, heat capacity, diffusivity, and thermal conductivity) on temperature, pressure and composition were accounted for using polynomial regressions fitted to the data on thermophysical properties from the literature [80, 83-85]. Molten salt properties were adopted from the data on commercially available molten salts (Dynalene, Inc. [86], Dynalene MS-2). All regression equations are listed in Appendix.

## 4. Results and discussion

Reactor performance was evaluated via numerical simulations as a function of operating parameters, in terms of $CO_2$ conversion ($X_{CO_2}$), selectivity to $CH_4$ ($S_{CH_4}$) and $CH_4$ yield ($Y_{CH_4}$):

$$X_{CO_2} = \frac{y_{CH_4} + y_{CO}}{y_{CH_4} + y_{CO} + y_{CO_2}} \tag{29}$$

$$S_{CH_4} = \frac{y_{CH_4}}{y_{CH_4} + y_{CO}} \tag{30}$$

$$Y_{CH_4} = \frac{y_{CH_4}}{y_{CH_4} + y_{CO} + y_{CO_2}} \tag{31}$$

Outlet conversion, selectivity and yield are calculated based on the outlet mole fractions. In all simulations, except those described in *Section 4.4*, the feed pressure was 500 kPa and feed composition was set to the molar stoichiometric ratio of $H_2/CO_2$ = 4. The molten salt feed temperature was set to its minimum operating temperature of 415 K [86]. The operating conditions assumed for these simulations are listed in Table 2.

**Table 2.** Operating conditions

| $P_f$ (kPa) | $H_2/CO_2$ | $T_{cf}$ (K) | $T_{int}$ (K) | $T_f$ (K) | GHSV ($h^{-1}$) | $G_{MS}/G_{MS,0}$ |
|---|---|---|---|---|---|---|
| 500 | 4/1 | 415 | 500-600 | 450-650 | 100-50,000 | 0.1-1 |

*$P_f$ denotes the feed pressure and $H_2/CO_2$ is the molar feed ratio of $H_2$ to $CO_2$. $T_{cf}$ stands for the coolant (molten salt) feed temperature. $T_{int}$ and $T_f$ are initial (start-up) and gas feed temperatures, respectively. GHSV is the gas hourly space velocity, Eq. (32). $G_{MS}/G_{MS,0}$ stands for the normalized gravimetric flow rate of the molten salt, Eq. (33).*

Variable operating parameters included initial temperature ($T_{int}$), gas stream feed temperature ($T_f$), gas hourly space velocity (GHSV) and the normalized cooling rate ($G_{MS}/G_{MS,0}$). The gas hourly space velocity is defined as follows:

$$GHSV = \frac{\varepsilon v_{gf}}{L} \tag{32}$$

The reference molten salt gravimetric flow rate is calculated assuming that the heat generation rate (for complete $CO_2$ conversion and no CO formation) is equal to the rate of heat removal by the molten salt (assuming that $\Delta T_{MS}$ = 300 K; the operating range of the molten salt is 415-758 K [86]):

$$G_{MS,0} = \frac{y_{CO_2} \Delta H_{SR} F_{tf}}{C_{pc} \Delta T_{MS}} \qquad F_{tf} = \rho_{gf} V_{PB} GHSV \tag{33}$$

### 4.1 Model validation

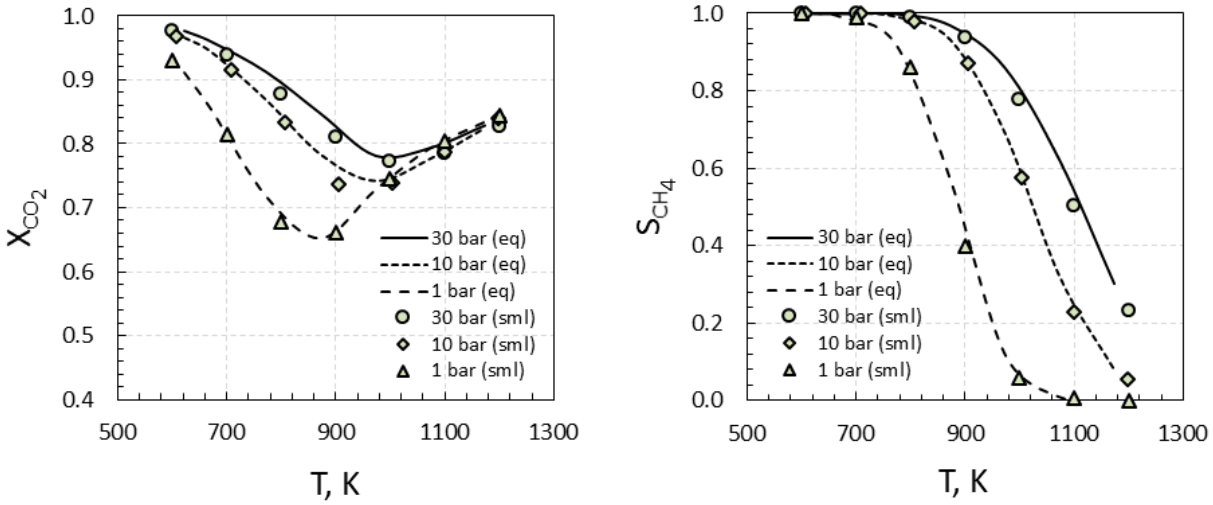


**Fig. 13.** Approach to equilibrium: $CO_2$ conversion ($X_{CO_2}$) and selectivity to $CH_4$ ($S_{CH_4}$) obtained in numerical simulations with low space velocity (symbols) are compared to equilibrium values (lines). *Parameters in numerical simulations: $T_{int}$ = 550 K, $T_f$ = 600 K, GHSV = 100 $h^{-1}$, $G_{MS} = G_{MS,0}$.*

For long residence times, i.e. low space velocity, it is expected that the reactor performance would approach to equilibrium. Comparison between the simulation results obtained at GHSV = 100 $h^{-1}$ and equilibrium data [87] is shown in Fig. 13, in terms of $CO_2$ conversion and selectivity to $CH_4$

formation (parameters are listed in the figure caption). Excellent agreement with the equilibrium data was obtained. $CO_2$ conversion is favored at high pressures and low temperatures; $CH_4$ selectivity drops rapidly at T > 850 K.

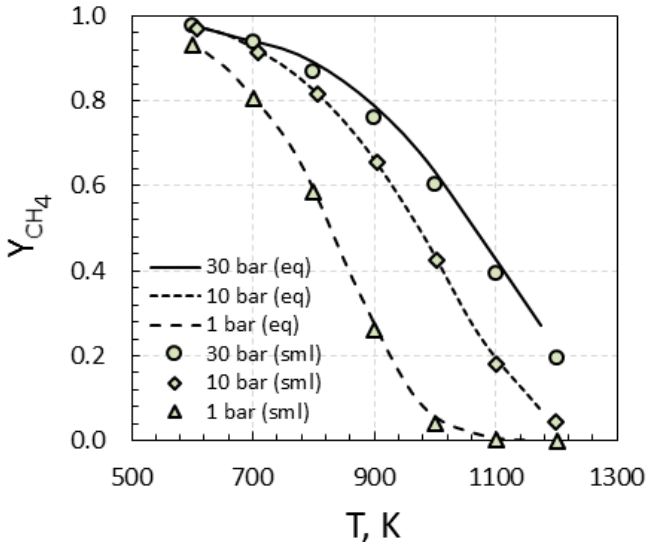


**Fig. 14.** Approach to equilibrium: $CH_4$ yield ($Y_{CH_4}$) obtained in numerical simulations with low space velocity (symbols) as compared to equilibrium values (lines). *Parameters in numerical simulations:* $T_{int}$ *= 550 K,* $T_f$ *= 600 K, GHSV = 100* $h^{-1}$, $G_{MS} = G_{MS,0}$.

Because of a combined effect of the decrease of conversion and selectivity with increasing temperatures, $CH_4$ yield drops rapidly for T > 800 K, Fig. 14. Therefore, thermal management of the Sabatier process is crucial. Reactor temperature should be kept sufficiently high to accelerate catalytic reactions, but below 900 K, when considerably high $CH_4$ yield is achievable at slightly elevated pressures, Fig. 14. Moreover, for the reactor configuration studied here, molten salt operating range becomes a crucial parameter. The coolant feed temperature should be obviously kept above the molten salt melting point but also well below the temperature of its thermal decomposition. The recommended operating range for the type of molten salt used in the

simulations is 415 - 758 K [86]. The upper range of this temperature regime is also favorable for $CH_4$ formation, Fig. 14.

### 4.2 Spatial profiles within the reactor

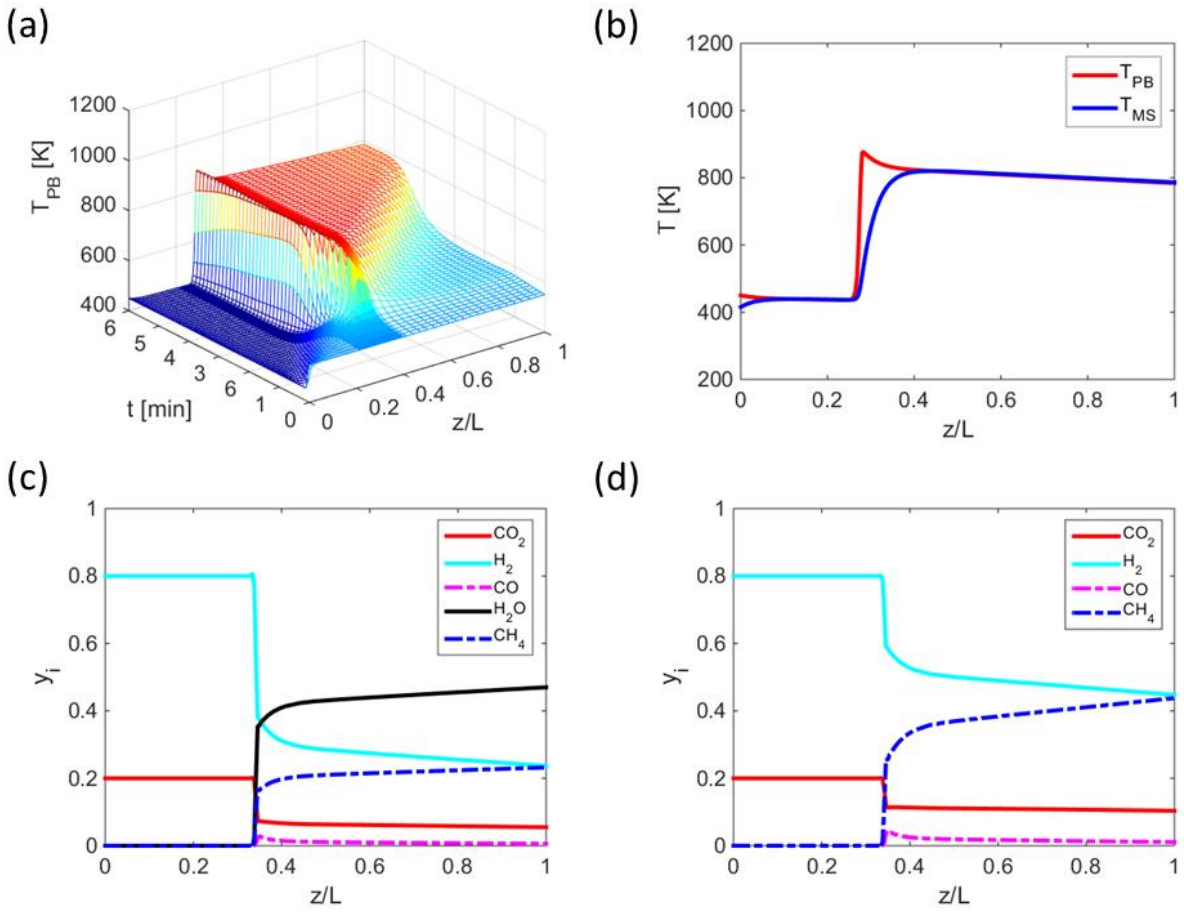


**Fig. 15.** The spatiotemporal profile of reactor ignition (a) and steady state spatial profiles of temperature (b), mole fractions (c), and mole fractions calculated on dry basis (d). $T_{PB}$ and $T_{MS}$ in panel (b) denote temperatures in the packed bed (PB) and molten salt (MS) compartments, respectively; $y_i$ denotes the mole fraction of a component *i*. *Parameters in numerical simulations:* $N_c = 22$, $T_{int} = 550$ K, $T_f = 450$ K, GHSV = 1,000 $h^{-1}$, $G_{MS} = 0.1G_{MS,0}$.

Typical spatial reactor profiles are presented in Fig. 15, showing the reactor ignition (Fig. 15a) and stationary spatial profiles of temperatures and mole fractions. For the set of parameters listed in Fig. 15, ignition occurs approximately at the first third of the reactor length, with subsequent formation of a stationary thermal front after approximately 5 minutes of simulated time, Fig. 15a. The simulation predicts that steady state temperatures are identical in the packed bed and molten salt compartments, except for the small area at the temperature front, Fig. 15b. Mole fraction profiles form a sharp front coinciding with temperature distribution, Fig. 15c, d. $CO_2$ and $H_2$ are mainly consumed at the front, producing mainly $CH_4$ and $H_2O$, as well as a small fraction of CO. Downstream the reactor, there is additional consumption of $H_2$, as CO is converted via methanation, Eq. (3). Since the methanation reaction is highly exothermic, downstream cooling will be crucial for reactor performance, as discussed in *Section 4.3.4*.

Increasing the inlet temperature of the feed gas mixture ($T_f$) shifts the location of the thermal front towards the reactor entrance, Fig. 16b. Reactor performance change accordingly (lower panels in Fig. 16). Slightly higher $CH_4$ yield is obtained for higher feed temperature, but in overall very similar performance is predicted in both cases, Fig. 16. However, the case shown in Fig. 16a is expected to be less beneficial for reactor operation. First, almost a third of the reactor stays cold with no reactions occurring there. Second, a thermal front located at some location within the reactor may be unstable and prone to downstream propagation which can result in reactor extinction, as discussed in *Section 4.3.2*.

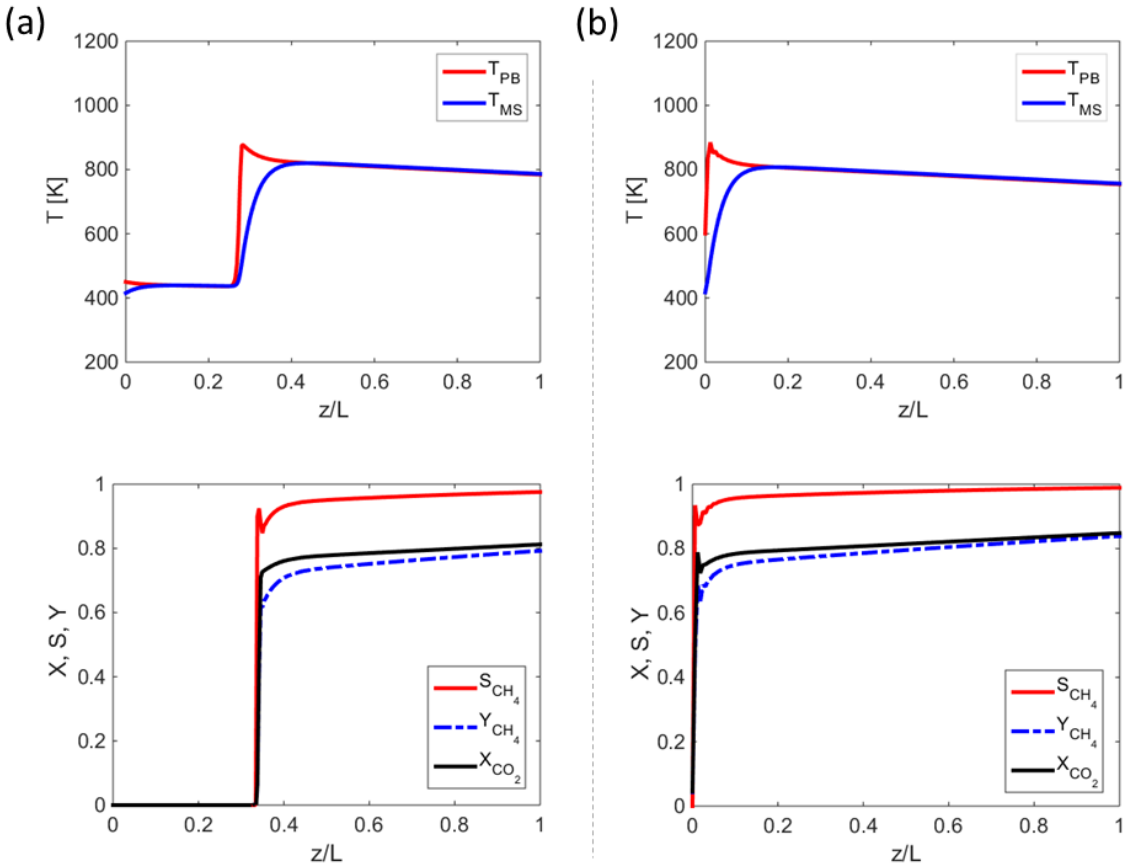


**Fig. 16.** Steady state spatial profiles of temperature (upper panels) and calculated reactor performance (lower panels) for gas stream feed temperatures of $T_f$ = 450 K (a) and $T_f$ = 600 K (b). $T_{PB}$ and $T_{MS}$ in panel (b) denote temperatures in the packed bed (PB) and molten salt (MS) compartments, respectively; $X_{CO_2}$, $S_{CH_4}$, and $Y_{CH_4}$ denote conversion, selectivity, and yield, Eqs. (29-31). *Parameters in numerical simulations: $N_c$ = 22, $T_{int}$ = 550 K, GHSV = 1,000 $h^{-1}$, $G_{MS} = 0.1G_{MS,0}$.*

### 4.3 Reactor performance

Reactor performance was evaluated as a function of variable parameters listed in Table 2: initial (start-up) temperature ($T_{int}$), inlet temperature of the feed mixture (the composition is $H_2/CO_2$ = 4, Table 2) ($T_f$), gas hourly space velocity (GHSV), and the molten salt gravimetric flow rate ($G_{MS}$) normalized to the reference rate ($G_{MS}/G_{MS,0}$). Initial and feed temperatures are expected to affect

the reactor performance significantly because of the high exothermicity of the Sabatier reaction system, Eqs (1-3). Feed flow rates in the reaction and coolant compartments (GHSV and $G_{MS}$) should be crucial in determining the rates of heat generation and removal. To investigate the effects of operation parameters on reactor performance without the disturbance of catalyst deactivation, catalyst activity $a$ is assumed to be 1 in this section (no catalyst deactivation).

### 4.3.1 Start-up temperature

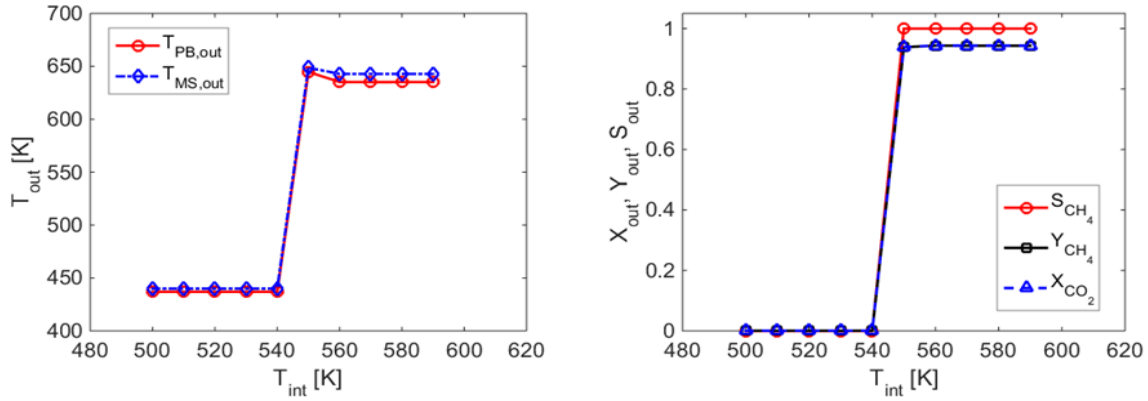


**Fig. 17.** Effect of the initial reactor temperature (pre-heating, start-up temperature) on reactor performance in terms of the outlet temperature (left panel) and outlet conversion, selectivity, and yield (right panel). *Parameters:* $N_c = 13$, $T_f = 520$ *K*, *GHSV* $= 1{,}000\ h^{-1}$, $G_{MS} = 0.38G_{MS,0}$.

Though the Sabatier reaction is highly exothermic, preheating will be required in a practical situation in order to ignite the reactor (an example of the simulated reactor ignition is shown in Fig. 15a). The effect of the initial (start-up) temperature is shown in Fig. 17: outlet temperatures, conversion, selectivity, and yield are plotted versus initial temperature. It is assumed that the entire reactor is heated to the same temperature, which can be achievable by flowing the molten salt through the cooling tubes before feeding the gas mixture. There is a sharp threshold temperature

of 545 K. Above this temperature, reaction ignition takes place, while further increase in the preheating temperature has virtually no effect on the reactor performance.

### 4.3.2 Effect of feed temperature

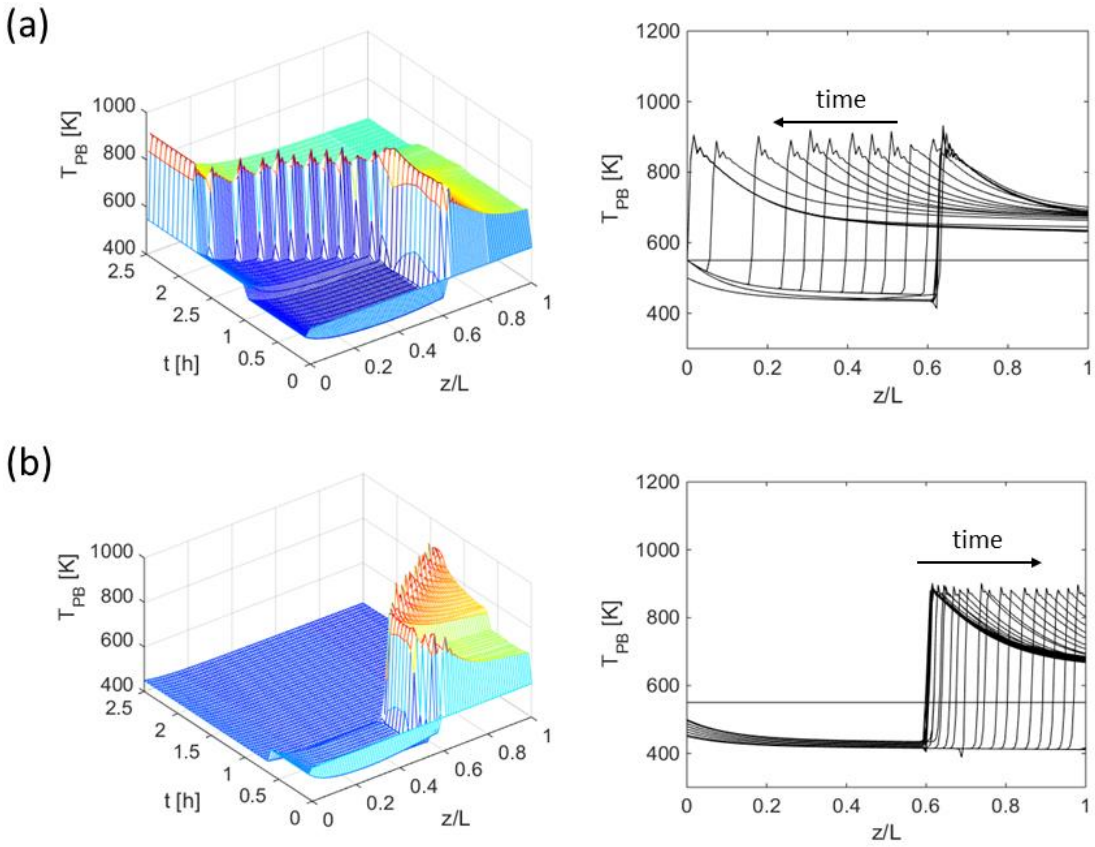


**Fig. 18.** Moving thermal fronts propagating upstream (a), as a result of increasing feed temperature from $T_f$ = 510 K to $T_f$ = 550 K, and downstream (b), as a result of switching feed temperature from $T_f$ = 510 K to $T_f$ = 450 K. Right panels show 2D representation of the spatiotemporal 3D patterns shown in left panels. *Parameters:* $N_c = 13$, $T_{int} = 550$ K, $GHSV = 1{,}000\ h^{-1}$, $G_{MS} = 0.38G_{MS,0}$.

The gas feed temperature ($T_f$) is a crucial operating parameter affecting the temperature distribution within the reactor, Fig. 16. It is expected that below a certain threshold feed temperature reactions will not take place, similarly to the effect of preheating, Fig. 17. On the other

hand, exceedingly high feed temperatures can result in reactor overheating, negatively affecting product distribution of the highly exothermic Sabatier reaction system, Eqs (1-3). In a practical situation, it is desirable to keep the feed temperature as low as possible to save energy. Another important consideration is feed temperature fluctuations which are unavoidable in real systems.

The effect of a step-wise change of the feed temperature is demonstrated in Fig. 18. For parameters listed in Fig. 18 and a feed temperature of $T_f = 510$ K, the simulation predicts formation of a stationary thermal front in the second half of the packed bed, left panels in Fig. 18 for $t < 1$ h. A step-wise increase of the feed temperature to $T_f = 550$ K immediately induces upstream front propagation with subsequent stabilization of the thermal front at the reactor entrance, Fig. 18a. If the feed temperature is abruptly decreased to $T_f = 450$ K, the front propagates downstream, eventually leading to the reactor extinction, Fig. 18b. Such moving thermal fronts are known to form in packed bed reactors with catalytic exothermic reactions; the propagation is due to the combine effect of heat generation, axial heat dispersion, and convection [62, 63]. Understanding this phenomenon is important from the practical point of view, in order to avoid operating under conditions that can lead to the formation of downstream propagating thermal fronts that result in reactor extinction.

Ignition-extinction curves obtained by the gradual increase or decrease of the feed temperature are shown in Fig. 19, in terms of the maximum and outlet packed bed temperature as a function of the feed temperature. For low feed temperatures, which are below the ignition threshold, both the maximum and outlet temperatures increase linearly, until the ignition threshold of $T_f > 500$ K is reached. A small increase in the feed temperature beyond this threshold leads to reactor ignition, Fig. 19. Further increase in the feed temperature results in a moderate decrease of the maximum

and outlet temperature, which can be attributed to the complex coupling of the reaction heat generation, inter-compartment heat transfer, and heat removal by the molten salt. When the feed temperature is gradually decreased following the top branch of the ignition-extinction curve, extinction occurs at T < 480 K.

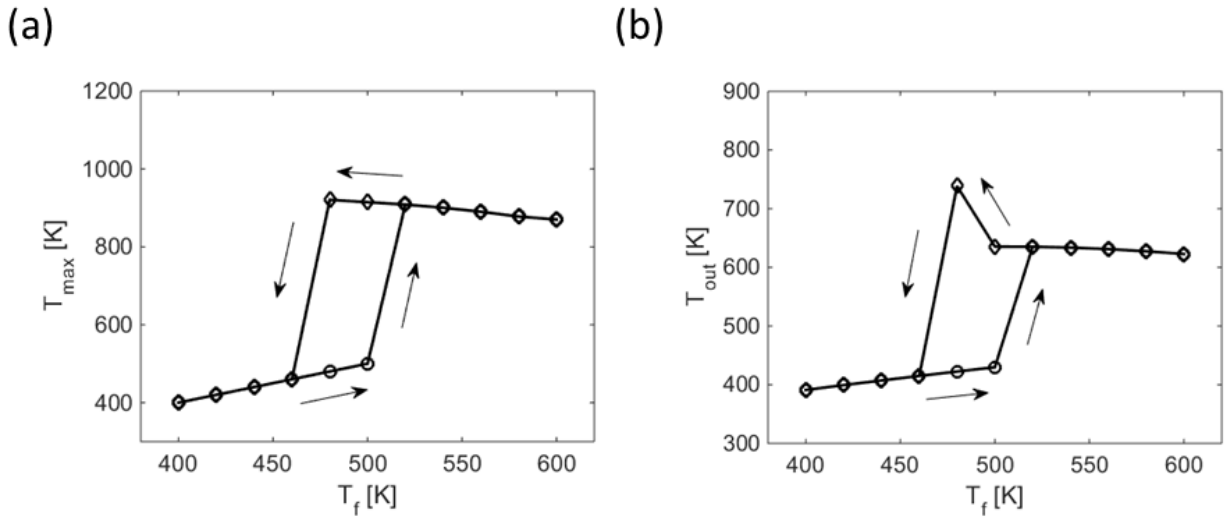


**Fig. 19.** Ignition-extinction curves showing the packed bed maximum temperature (a) and the packed bed outlet temperature (b) as a function of the gas feed temperature. *Parameters:* $N_c = 13$, $T_{int} = 550$ *K*, *GHSV* = 1,000 $h^{-1}$, $G_{MS} = 0.38G_{MS,0}$.

Since the extinction temperature is different from the ignition threshold, there is a small region of bi-stability, where both the ignited and extinguished states co-exists. For practical applications, it is favorable to operate the reactor well outside the region of bi-stability where sudden reactor extinctions can occur as a result of fluctuations in the feed temperature. Fluctuations in operating parameters are expected to occur in real situations and other operating parameters can affect the extinction-ignition behavior as well, such as space velocity [62, 63].

### 4.3.3 Effect of space velocity

Increasing space velocity is beneficial from the point of view of maximizing reactor throughput. However, in the reactor configuration analyzed herein, Fig. 12, the coupling of the reaction heat generation with the heat transfer between the compartments and heat removal by the molten salt can result in nontrivial behavior. The effect of increasing space velocity on reactor profiles is demonstrated in Fig. 20, where elevated cooling rate was used ($G_{MS} = 0.5G_{MS,0}$). At low space velocity, Fig. 20a, the inter-compartment heat transfer is very efficient, resulting in equal temperatures in the packed bed and molten salt compartment, except for the small temperature difference at the reactor entrance, Fig 20 (upper panel). For the parameters used in Fig. 20a, the simulation predicted highly efficient cooling. Both the gas stream and molten salt leave the reactor at the temperature which is only slightly higher than the molten salt feed temperature. Note, that heat losses to the environment was accounted for in the current study, last term in Eq. (8).

Increasing the space velocity ten-folds leads to a very different distribution within the reactor, Fig. 20b. Though for the most of the reactor, the temperatures are equal in both compartments, a very significant temperature gradient exists in the first quarter of the reactor, upper panel in Fig. 20b. The cooling is much less efficient, though same ratio of $G_{MS} = 0.5G_{MS,0}$ is kept; the outlet temperature is ~ 600 K. The exceedingly high packed bed temperature at the reactor entrance affects the mole fraction distribution within the reactor. As a result of less efficient cooling, the outlet mole fraction of $CH_4$ is lower, lower panel in Fig. 20b. For high space velocities, the heat removal could be limited by the heat transfer between the compartments, which is represented in the model by the heat exchange terms, in Eqs (8, 9).

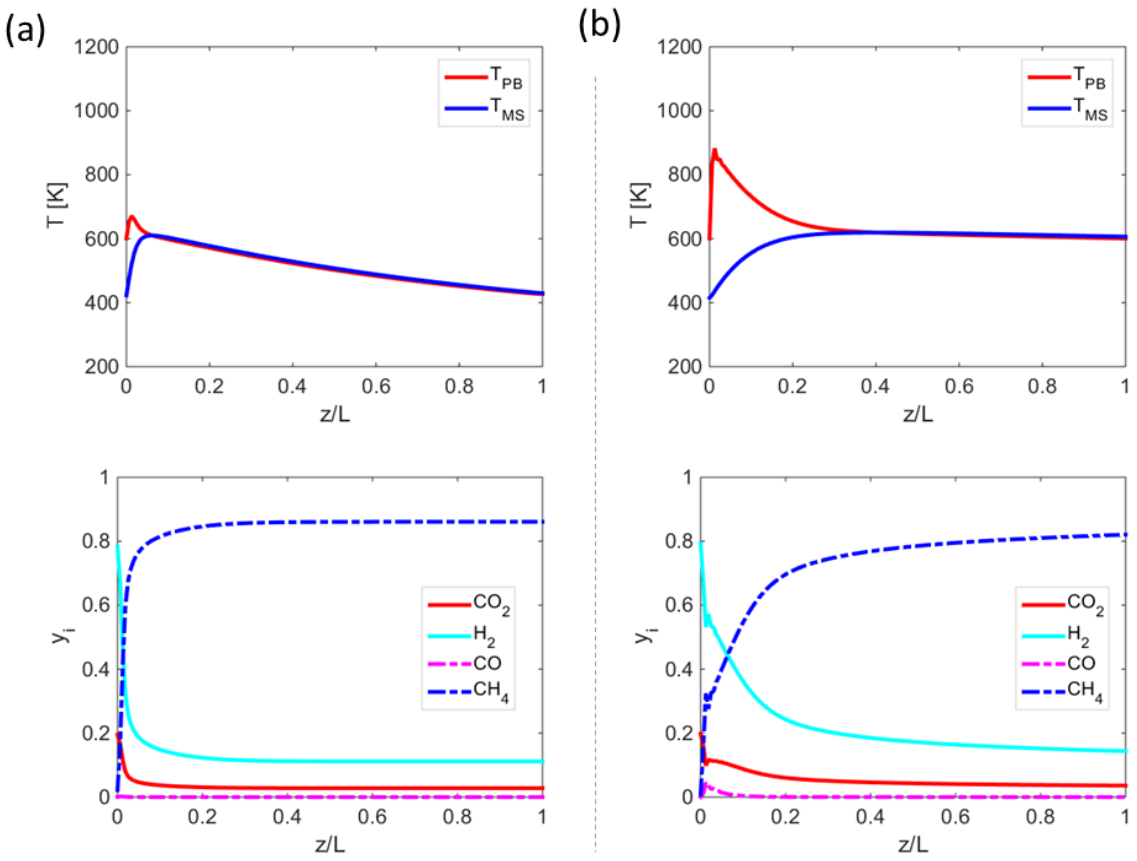


**Fig. 20.** Temperature profiles (upper panels) and mole fraction distributions (lower panels) for low space velocity, GHSV = 100 $h^{-1}$ (a) and for elevated space velocity, GHSV = 1,000 $h^{-1}$ (b). *Parameters:* $N_c = 22$, $T_{int} = 550\ K$, $T_f = 600\ K$, $G_{MS} = 0.5G_{MS.0}$.

Wall heat transfer coefficients ($U_{w,HL}$, $U_{w,HE}$) are calculated from correlations, Eqs (26-28), and, therefore, cannot be arbitrary manipulated. The reactor geometry is fixed in this study except for the number of cooling tubes ($N_c$) which can be varied within the restriction of the reactor design, Table 1. The effect of the number of coolant tubes on the reactor performance at high space velocity (GHSV = 10,000 $h^{-1}$) is demonstrated in Fig. 21. For $N_c$ = 22, which was used in all simulations presented until this point, both streams (the reaction mixture and the coolant) exit the reactor at same temperature. Decreasing the number of cooling tubes leads to slightly lower outlet temperatures, until a significant difference between the outlet temperatures appear for $N_c < 12$. As

molten salt gravimetric flow rate is constant and molten salt should be distributed evenly in all of coolant tubes, the increase of the number of cooling tubes leading to the increase of total cross-sectional area of coolant compartment will result in a decrease of the molten salt velocity in each coolant tube. Thus, more heat is transferred from packed-bed compartment to coolant compartment due to sufficient heat exchange and molten salt temperature increases. However, for $N_c$>12, less heat is removed from the reactor system due to the lower residence time of molten salt in the coolant compartment, so the packed-bed compartment temperature increases accordingly. So for $N_c$>12, higher molten salt gravimetric flow rate is recommended. Although $CO_2$ conversion and $CH_4$ yield are not affected to a significant extent by the inefficient heat transfer (right panel in Fig. 21), the heat removal appears to be limited by the insufficient heat exchange area for $N_c$ < 12. Note that the simulations predict $CH_4$ yields over 90% at the elevated space velocity of GHSV = 10,000 $h^{-1}$.

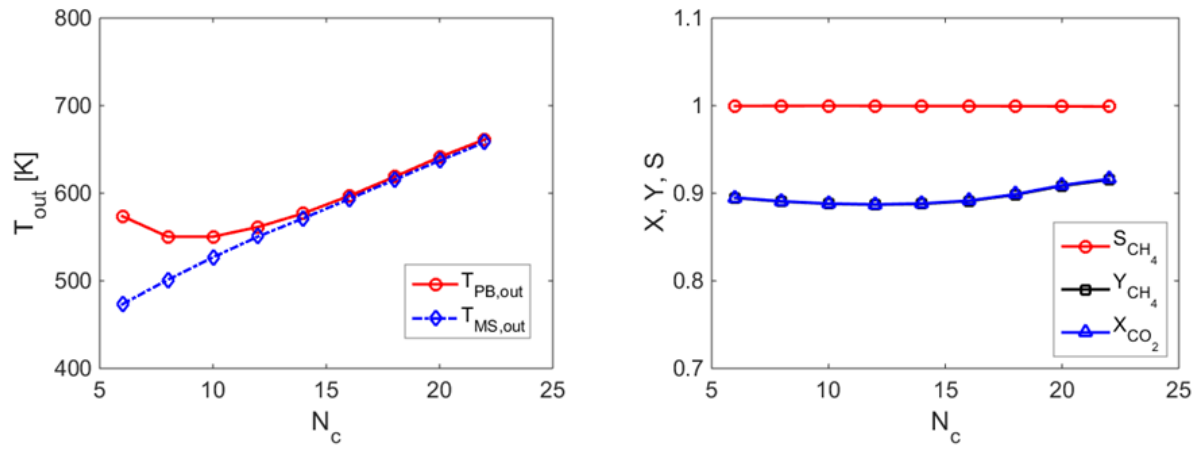


**Fig. 21.** Effect of the number of cooling tubes on the reactor performance at high space velocity. Outlet temperatures of the packed bed (PB) and coolant, molten salt (MS) compartments (a) and outlet conversion, selectivity, and yield (b) are plotted versus the number of cooling tubes ($N_c$) in the reactor. *Parameters:* $T_{int}$ *= 550 K,* $T_f$ *= 650 K, GHSV = 10,000* $h^{-1}$, $G_{MS} = G_{MS,0}$.

As it is highly desirable to maximize the reactor throughput to increase the rate of $CH_4$ production and thus to reduce the capital cost investment, reactor performance should be investigated over the range of space velocities. In Fig. 22, the reactor performance is evaluated as a function of space velocity ranging from 1,000 1/h to 25,000 1/h using $N_c$ = 13, as reducing number of tubes will simplify reactor manufacturing and operation. Elevated rate of cooling was used, $G_{MS} = 0.4G_{MS,0}$, as previous simulations showed insufficient heat removal for $G_{MS} = 0.1G_{MS,0}$ (compare Fig. 16 and Fig. 20). The effect of the space velocity on the outlet $CO_2$ conversion, selectivity to $CH_4$, $CH_4$ yield is demonstrated in the left panel of Fig. 22; showing also the normalized pressure drop, $\Delta P_N = (P_f - P_{out})/P_f$. Corresponding outlet temperatures are shown on the right panel of Fig. 22.

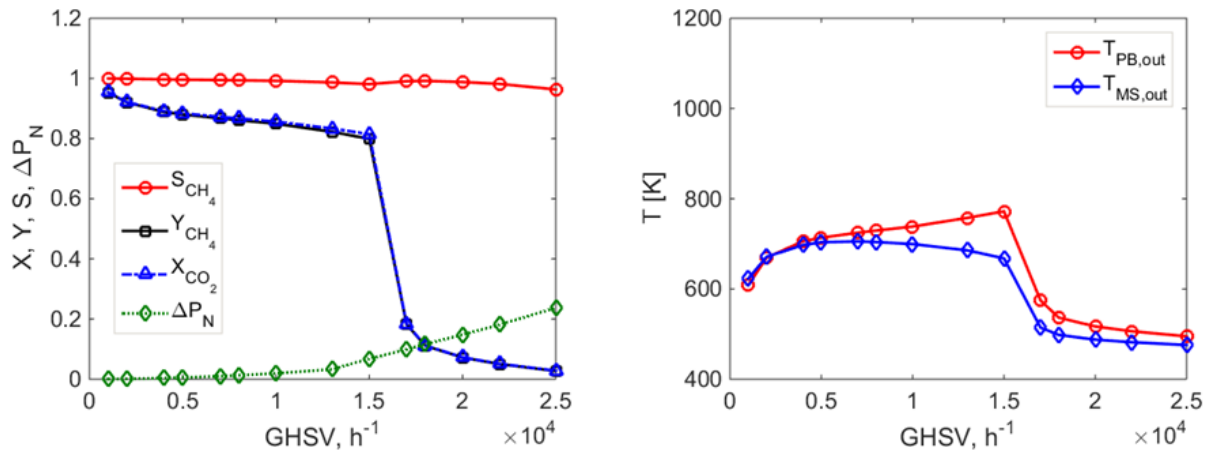


**Fig. 22.** Effect of space velocity on the reactor performance. Outlet conversion, selectivity, yield, and normalized pressure drop (left panel) and outlet temperatures in the packed bed and molten salt compartments (right panel) are plotted versus gas space velocity. Normalized pressure drop is defined as $\Delta P_N = (P_f - P_{out})/P_f$. *Parameters:* $N_c = 13$, $T_{int} = 550$ *K*, $T_f = 600$ *K*, $G_{MS} = 0.4G_{MS,0}$.

For relatively low space velocities (GHSV < 5,000 $h^{-1}$), outlet $CO_2$ conversions and $CH_4$ yields higher than 90% are achieved, while full selectivity to the formation of $CH_4$ is predicted at the

reactor outlet. These results indicate that the cooling is sufficient to prevent the formation of CO. Indeed, as it can be seen from Fig. 22 (right panel), the outlet packed bed temperatures are below 700 K for GHSV < 5,000 $h^{-1}$, for which the equilibrium predicts virtually no CO formation. Even though some CO can still be formed in the hottest part of the reactor, it is converted into $CO_2$ downstream.

As space velocity is further increased, the conversion and yield drop below 90% and the pressure drop starts to be significant, left panel of Fig. 22. The packed bed outlet temperature gradually increase, while the outlet molten salt temperature decreases. For GHSV > 7,000 $h^{-1}$, there is a substantial difference between outlet temperatures, indicating insufficient heat removal due to the transport limitations, i.e., the rate of heat transfer through the walls of the cooling tubes is significantly lower than the rate of reaction heat generation. Importantly, the 80% $CH_4$ yield is still achieved at a high space velocity of GHSV = 15,000 $h^{-1}$, while the outlet molten salt temperature is well above the solidification point and below the thermal decomposition threshold; the operating range of the molten salt is 415-758 K [86]. Above the threshold of GHSV > 15,000 $h^{-1}$, the reactor performance drops sharply, which can be attributed to overcooling. Note that the gas feed, which enters the reactor at a relatively low temperature of $T_f$ = 600 K, also contributes to the cooling, especially at high space velocities. Pressure drop also increases considerably for GHSV > 15,000 $h^{-1}$, which can also contribute to the performance drop, as low pressures are thermodynamically unfavorable for the Sabatier reaction, Figs 13, 14. Note that in all simulations the inlet pressure was fixed to $P_f$ = 500 kPa, Table 2.

### 4.3.4 Optimization of cooling rate

For process optimization, it is highly desirable to maximize the reactor throughput, while keeping high $CH_4$ yields. At the same time, the molten salt flow rate should be minimized in order to reduce energy investment in pumping and storage. However, decreasing the rate of cooling will lead to the increase of the reactor temperature reducing $CO_2$ conversion and, therefore, $CH_4$ production. Therefore, optimization of the molten salt flow rate, i.e., cooling rate, will be crucial for the reactor performance improvement and, therefore, for system optimization.

Effect of the cooling rate on the reactor performance is first examined for a fixed space velocity, Fig. 23. For low cooling rate of $G_{MS} = 0.1G_{MS,0}$, Fig. 23a, the heat removal is insufficient and $CO_2$ is only consumed at the reactor entrance. There is further consumption of $H_2$ downstream the reactor, but only due to the CO conversion, lower panel of Fig. 23a. Importantly, the molten salt temperature is above 800 K for the most of the reactor, which is outside the operating range and thus will lead to thermal decomposition of the molten salt. Increasing the cooling rate ten-fold, to $G_{MS} = G_{MS,0}$, changes reactor profiles dramatically, Fig. 23b. The molten salt temperature is within its operating range, upper panel in Fig. 23b and the packed bed temperature is cooled down along the reactor. As a result, in addition to the $CO_2$ consumption at the reactor entrance, there is additional $CO_2$ consumption downstream the reactor, resulting in a dramatic improvement of $CH_4$ production, lower panel in Fig. 23b. Once can conclude that a declining temperature profile is highly favorable for $CH_4$ production via Sabatier reaction. From the thermodynamic point of view, relatively high temperatures in the first part of the packed bed favor $CO_2$ conversion into $CH_4$ but also to CO, Fig. 13. As temperature declines downstream the reactor, the CO formed is converted into more $CH_4$, as it is predicted by the equilibrium, Fig. 13.

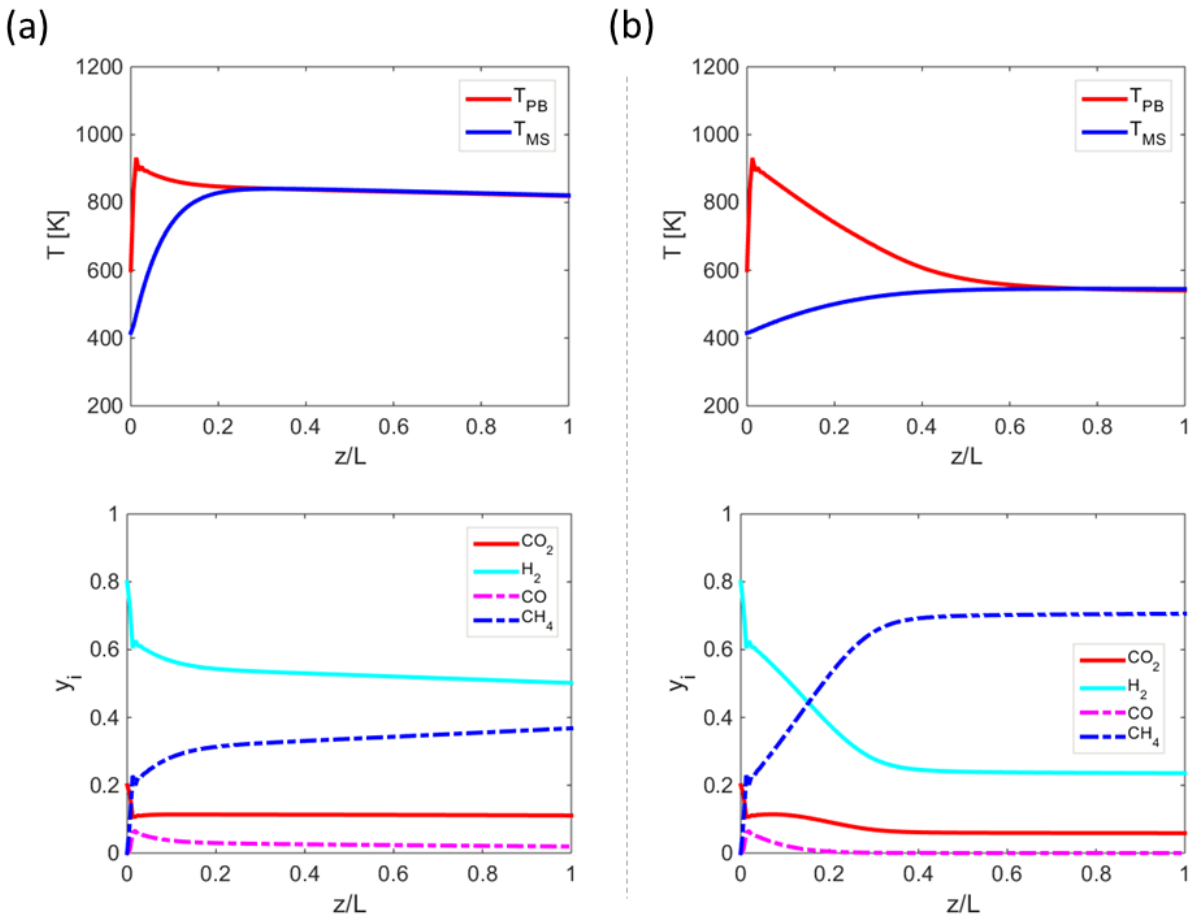


**Fig. 23.** Effect of the cooling rate on the reactor performance. Spatial temperature profiles (upper panels) and mole fraction distributions (lower panels) for low cooling rate, $G_{MS} = 0.1G_{MS,0}$ (a), and elevated cooling rate, $G_{MS} = G_{MS,0}$ (b). *Parameters:* $N_c = 22$, $T_{int} = 550$ *K*, $T_f = 600$ *K*, *GHSV* = *2,000* $h^{-1}$.

The reactor performance for low and high cooling rates is analyzed in Fig. 24 over a wide range of space velocities, in terms of outlet conversion, selectivity, and yield (also showing pressure drop). From analyzing Fig. 24 in comparison with Fig. 22 (intermediate cooling rate), one can conclude that the sharp drop in the reactor performance can be rather attributed to overcooling by the molten salt. As the cooling rate is increased from low ($G_{MS} = 0.08G_{MS,0}$, left panel in Fig.

24) to intermediate ($G_{MS} = 0.38G_{MS,0}$, left panel in Fig. 22), and to high ($G_{MS} = 0.77G_{MS,0}$, right panel in Fig. 24), the performance drop threshold decreases from GHSV = 36,000 $h^{-1}$, to GHSV = 15,000 $h^{-1}$, and GHSV = 8,000 $h^{-1}$.

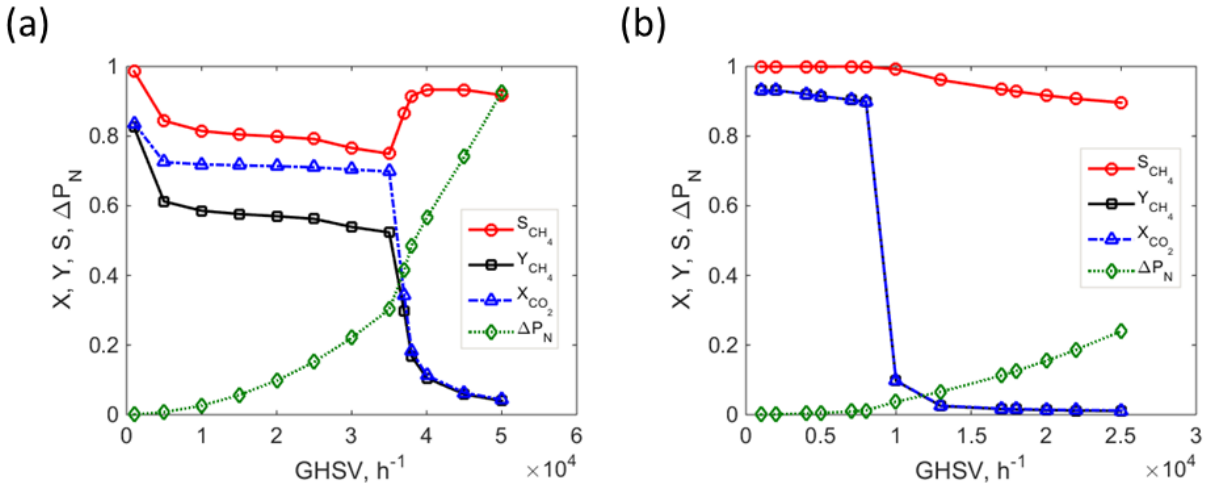


**Fig. 24.** Effect of the heat removal rate on the reactor performance. Outlet conversion, selectivity, yield, and normalized pressure drop are plotted versus space velocity for relatively low cooling rate, $G_{MS} = 0.08G_{MS,0}$ (a) and elevated cooling rate, $G_{MS} = 0.77G_{MS,0}$ (b). *Parameters:* $N_c = 13$, $T_{int} = 550$ *K*, $T_f = 600$ *K*.

Pressure drop can also contribute to the drop in performance, particularly for the case of the low cooling rate: the pressure drop becomes very significant at the threshold space velocity of GHSV = 36,000 $h^{-1}$ (Fig. 24, left panel). Since $CH_4$ production is favored by high pressures (Figs 13, 14), it is desirable to keep the entire reactor at high pressure. Operation at low cooling rate is also disadvantageous from the point of view of conversion and selectivity. High conversion and selectivity are only attainable for low space velocity. As the space velocity is increased, both $CO_2$ conversion and selectivity to $CH_4$ drop significantly, resulting in $CH_4$ yields below 60%. This can be attributed to insufficient cooling that results in exceedingly high temperatures that suppress $CH_4$

production. Overcooling, i.e. high cooling rate (Fig. 24, right panel) is also disadvantages. Though high $CH_4$ yield is obtained, operation is limited to GHSV < 10,000 $h^{-1}$.

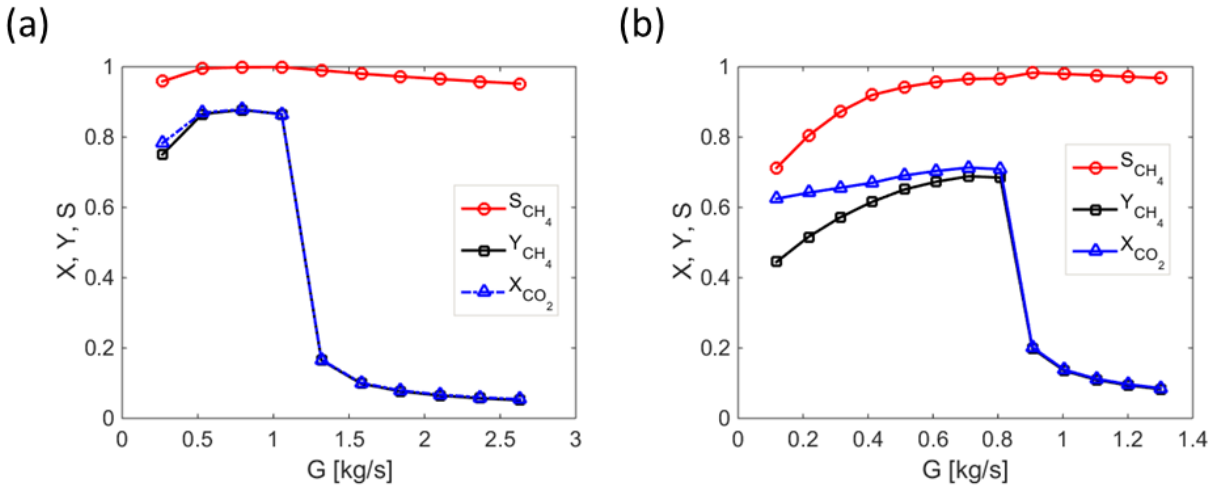


**Fig. 25**. Effect of the cooling rate on the reactor performance at high space velocities. Outlet conversion, selectivity, and yield are plotted versus the molten salt flow rate for GHSV = 20,000 $h^{-1}$ (a) and GHSV = 45,000 $h^{-1}$ (b). Ranges of the molten salt flow rate correspond to $G_{MS}$ = (0.2-2.3)$G_{MS,0}$ (a) and $G_{MS}$ = (0.05-0.4)$G_{MS,0}$ (b). *Parameters:* $N_c = 13$, $T_{int} = 550$ *K*, $T_f = 650$ *K*.

Since the reactor performance is strongly affected by the rate of heat removal, cooling rate optimization is of crucial importance. The effect of the cooling rate at high (fixed) space velocities is examined in Fig. 25. Outlet conversion, selectivity, and yield are plotted versus the molten salt flow rate for GHSV = 20,000 $h^{-1}$ (Fig. 25a) and GHSV = 45,000 $h^{-1}$ (Fig. 25b). The increase in the molten salt gravimetric flow rate initially leads to a considerable improvement in $CH_4$ production, which is followed by a sharp drop after a certain threshold, similarly to the effect of space velocity, Figs 22, 24. While for GHSV = 20,000 $h^{-1}$ the selectivity to $CH_4$ remains almost complete over the entire range, GHSV = 45,000 $h^{-1}$ increasing the molten salt flow rate results in a very significant improvement, right panel in Fig. 25. In both cases, the optimum in the $CH_4$ yield is observed, more

pronounced for the higher space velocity. Also, the sharp drop in the reactor performance occurs at a lower $G_{MS}/G_{MS,0}$ ratio for GHSV = 45,000 $h^{-1}$.

To summarize the findings discussed in two last sub-sections, it can be concluded that both space velocity and cooling rate (molten slat flow rate) are crucial parameters affecting the reactor performance. The (desirable) increase in the space velocity unavoidably leads to the declining $CH_4$ yield and, eventually, a threshold-like drop in performance leading to conversions and yields which cannot be considered practical (below 20%). Moderately elevated (GHSV < 10,000 $h^{-1}$) space velocities with intermediate cooling rates ($G_{MS} \approx 0.5G_{MS,0}$) are recommended for the reactor configuration analyzed here.

### 4.3.5 Techno-economic evaluation

The economic viability of the reactor configuration analyzed in this study should be discussed at the level of the entire system, Fig. 1. Herein, we only provide a preliminary techno-economic evaluation. One of the important considerations is the reactor compactness, which can be evaluated by calculating the power density as a function of the reactor throughput:

$$P = \frac{F_{CH_4,out} LHV_{CH_4}}{V_r} \tag{34}$$

The calculated power densities shown in Fig. 26 (left panel) correspond to the results presented in Fig. 22. The power density increases nearly linearly for increasing reactor throughputs, as the rate of $CH_4$ production increases, for the fixed reactor size. Very high power density is achieved at the optimum, before the reactor performance declines sharply, resulting in a drop of $CH_4$ production.

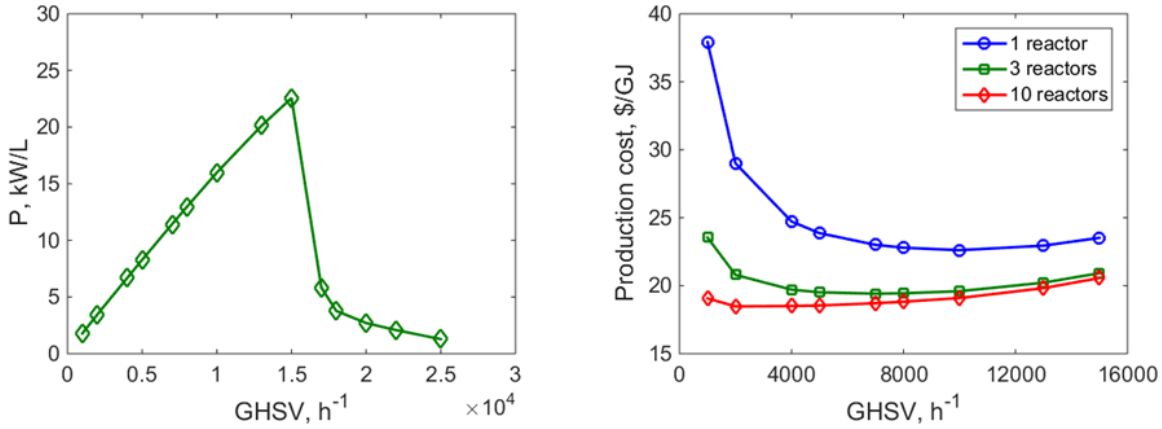


**Fig. 26.** Techno-economic evaluation in terms of the reactor power density, Eq. (34), and the renewable natural gas production cost, Eq. (35), as a function of the reactor throughput. The production cost (right panel) is shown for a single reactor, three reactors, and 10 reactors, for the cumulative 10,000 h of operation. *Parameters:* $N_c = 13$, $T_{int} = 550$ *K*, $T_f = 600$ *K*, $G_{MS} = 0.38G_{MS,0}$.

To evaluate $CH_4$ production cost, we consider the most essential elements of the synthetic methane generation system shown in Fig. 1: a molten salt pump, a steam turbine, and the reactor itself. The $H_2$ production infrastructure cost is lumped in the price of $H_2$. It is assumed that a pure stream of $CO_2$ is available. The production cost was calculated using the following equation:

$$\begin{aligned} &production\ cost = capital\ investement + pumping\ cost \times t + \\ &+[F_{H_2,f} \times H_2\ price - \eta_{ST} G_{MS} C_{P,MS} (T_{MS,out} - T_{MS,f}) \times electricity\ price] \times t \end{aligned} \tag{35}$$

The capital investment includes the cost of the reactor, molten salt pump, and steam turbine. The reactor cost will not be a significant contribution, since the price of Ni-based catalysts considered herein is less than 10 $/kg and the reactor construction material is stainless steel. The packed bed volume is ~ 25 L, which will result in approximately $3,000 cost of a single reactor. The molten salt pump and steam turbine costs were assumed to be $40,000 and $58,000, respectively. These are typical prices for the small-to-medium scale equipment (http://www.rh-pumps.com/pump-application/molten-salts/, http://wabashpower.com/inventory/turbine-generators/steam-turbines/510-kw-

dresser-rand-turbodyne). The electricity consumption for pumping is considered in Eq. 35 as well, but this contribution was found to be rather insignificant to another time-dependent cost which is $H_2$ consumption. A (rather optimistic) projection of 2 $/kg was used as a price of renewable $H_2$. The cost of $H_2$ consumed can be partially recovered by electricity generation by a steam turbine, Fig. 1, using the reactor outlet molten salt to generate steam. The overall efficiency of the electricity generation from the molten salt heat ($\eta_{ST}$) was assumed to be 30% and the electricity celling price was fixed to 0.13 $/kWh.

The obtained production costs, right panel in Fig. 26, clearly cannot compete with the current low prices of natural gas (~2.5 $/GJ), though historically the price of natural gas fluctuated well above 10 $/GJ (in 2008). Also, the process analyzed in this study consumes $CO_2$, which can be potentially used for carbon trading. Even though the produced renewable natural gas (RNG) will be eventually burned to generate electricity and heat, the use of RNG reduces the consumption of the fossil natural gas, reducing therefore $CO_2$ emissions. This is particularly beneficial if the source of $CO_2$ is not fossil, such as fermentation flue gas or biogas.

As it can be seen from Fig. 26, increasing the number of reactors reduces the production cost substantially. For the relatively small reactor size analyzed herein, no additional molten salt pump or steam turbine is required up to ten reactors, and the cost of reactors is low. As a result, when the number of reactors is increased, the capital cost remains almost same, reducing the production cost. For a small number of reactors, it is beneficial to operate at high space velocities. For ten reactors, similar price is obtained over the entire range, though there is a slight optimum for moderately high space velocity. Importantly, the production cost drops down below 20 $/GJ, starting to approach the price of $H_2$: 2 $/kg is equivalent to 16.6 $/GJ for $H_2$, using the low heating

value. From the thermodynamic point of view, the maximum of 83% of the $H_2$ energy content can be recovered via the Sabatier reaction (low heating values of $CH_4$ and $H_2$ are 802.3 kJ/mol and 241.8 kJ/mol, respectively); the rest is dissipated as heat, Eq. (1). In this case, the $CH_4$ production cost will be ~ 20 $/GJ. Because some heat is recovered from the molten salt stream for electricity generation, Fig. 1, Eq. (35), it is possible to reduce the production cost even below 20 $/GJ even for incomplete $CO_2$ conversion and $CH_4$ yield.

### 4.4 Effect of catalyst deactivation on the reactor performance

The analysis of the catalyst deactivation-dependent reactor operation was conducted via evaluating the reactor performance in the range of operating parameters listed in Table 3: feed pressure ($P_f$), steam feed mole fraction (SFMF), gas hourly space velocity (GHSV), and the normalized molten salt flow rate ($G_{MS}/G_{MS,0}$). As the partial pressure of $CH_4$ can influence the catalyst activity, Eq. (23), the effect of catalyst deactivation was analyzed for two different feedstocks. The first case, denoted as "pure $CO_2$ feed", is the feed gaseous mixture that contains only $CO_2$ and $H_2$. In the second case, denoted as "biogas feed", $H_2$ is fed into reactor along with a raw biogas (60% $CH_4$ and 40% $CO_2$) instead of pure $CO_2$; it is assumed that impurities that can cause deactivation (e.g., $H_2S$) are removed from the raw biogas feed upstream to the reactor. In all simulations, the molar stoichiometric ratio of $H_2/CO_2 = 4$ was kept. All relevant parameters are listed in Table 3.

**Table 3.** Operating conditions for catalyst deactivation analysis

| $H_2/CO_2$ | $T_f$ (K) | $T_{cf}$ (K) | $G_{MS}/G_{MS,0}$ | $P_f$ (bar) | *SFMF* | GHSV ($h^{-1}$) | TOS(h) |
|---|---|---|---|---|---|---|---|
| 4/1 | 650 | 415 | 0.08-0.77 | 1-20 | 0-0.5 | 1000-25,000 | 10-10,000 |

*$H_2/CO_2$ denotes the ratio of feed mole fraction of $H_2$ to $CO_2$. $T_f$ and $T_{cf}$ stand for the feed temperature of reactants and coolant. $G_{MS}/G_{MS,0}$ stands for the normalized gravimetric flow rate of the molten salt, Eq. (33). $P_f$ denotes the feed pressure and SFMF is the steam feed mole fraction. GHSV is the gas hourly space velocity, Eq. (32). TOS stands for time-on-stream.*

### 4.4.1 Reactor fed with pure $CO_2$

#### 4.4.1.1 Catalyst deactivation effect

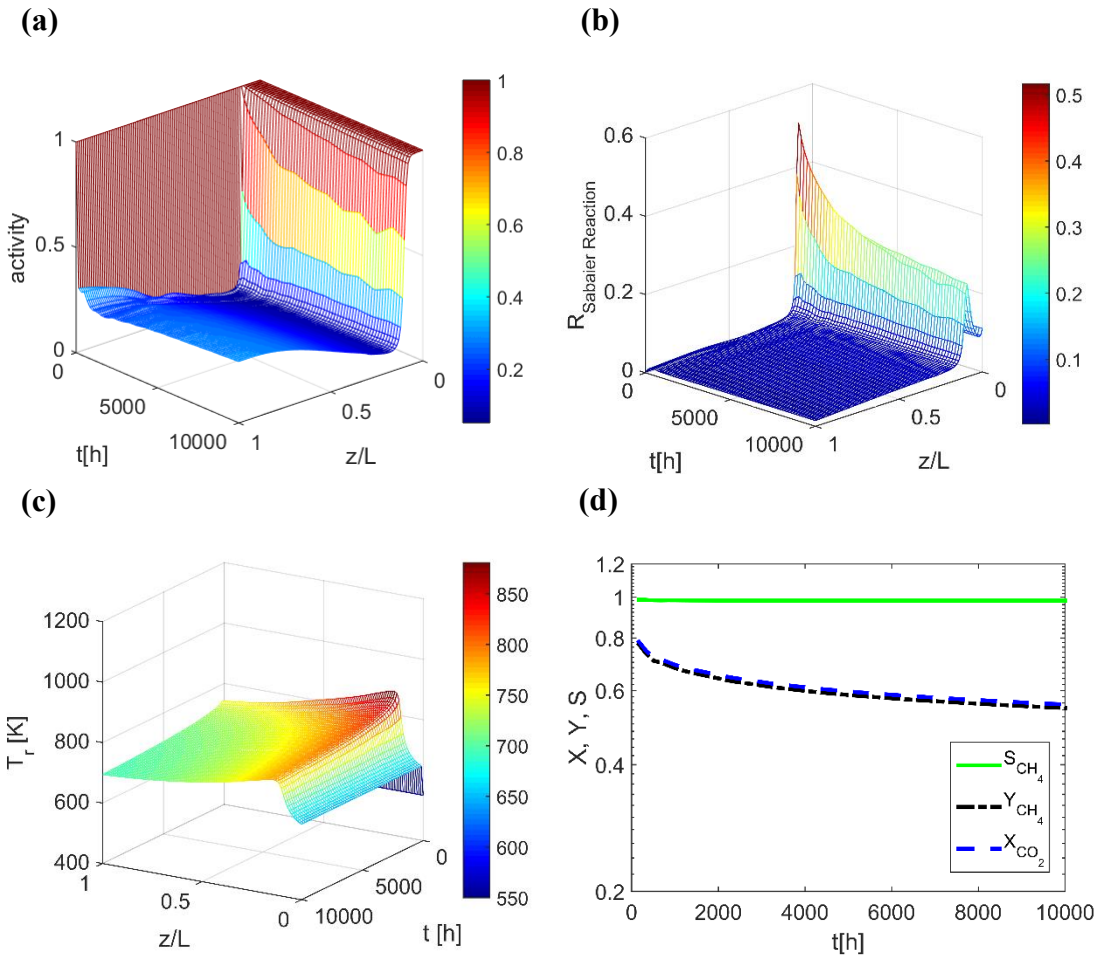


**Fig. 27.** The spatiotemporal profile of activity (a), normalized reaction rate (b), catalyst activity (c) and calculated reactor performance as a function of operation period (d). $X_{CO_2}$, $S_{CH_4}$, and $Y_{CH_4}$ denote conversion, selectivity, and yield, Eqs. (29-31). *Parameters: $P_f$ = 5 bar, $T_f$ = 650 K, GHSV = 25,000 $h^{-1}$, $G_{MS} = 0.40G_{MS,0}$*

An example of the spatiotemporal profiles of catalyst activity, normalized Sabatier reaction rate, and reactor temperature, and the dynamic reactor performance are illustrated in Fig. 27. Catalyst activity at the entrance of the reactor is ~100% since no $CH_4$ is present in the feed gas,

and a substantial decrease of activity appears when a thermal front is subsequently formed, Fig. 27c. However, activity increases slightly downstream the reactor due to the reaction temperature drop caused by heat removal. Deactivation influencing catalyst activity is also a major parameter affecting reactor temperature, performance, etc. The deactivation effect on reactor performance is presented in Fig. 27d, showing $CO_2$ conversion and $CH_4$ yield experience a sharply decrease initially and a graduated decrease afterwards.

The trend of reactor performance is expected to coincide with the catalyst activity variation. Summarizing the findings in Fig. 27, one can conclude that a considerable rise of temperature along with large amount of $CH_4$ production and $H_2$ consumption lead to a significant catalyst deactivation. However, the decrease of catalyst activity can result in the decrease of reactor temperature. Therefore, deactivation rate will also decrease due to the exponential dependence of the deactivation rate on temperature, Eqs (22, 23).

Spatial profiles of temperatures in the reactor and cooling compartments and mole fractions at TOS = 10 h and TOS = 10,000 h are shown in Fig. 28; TOS stands for time on stream. At TOS = 10 h, when catalyst activity is still high, the reactor performs very well and deactivation barely affect it, Fig. 28a. However, when TOS is up to 10,000 h, reactor temperature, and corresponding $CH_4$ production and $H_2$ consumption are much lower than those at TOS = 10 h, which can be attributed to catalyst deactivation. In addition, by comparing the spatiotemporal profile of activity, Fig. 27a, with the mole fraction distribution, Fig. 28 (right panel), it can be seen that the catalyst activity at the reactor outlet is higher. Since the $CH_4$ mole fraction is actually higher at the reactor outlet than at the location of the thermal front, the catalyst deactivation can be mainly attributed to the effect of high temperature. Indeed, analysis of the catalyst deactivation expression, Eqs (22,

23), shows the strong, exponential dependence of the deactivation rate on temperature, while the dependence on the $CH_4$ mole fraction is less steep.

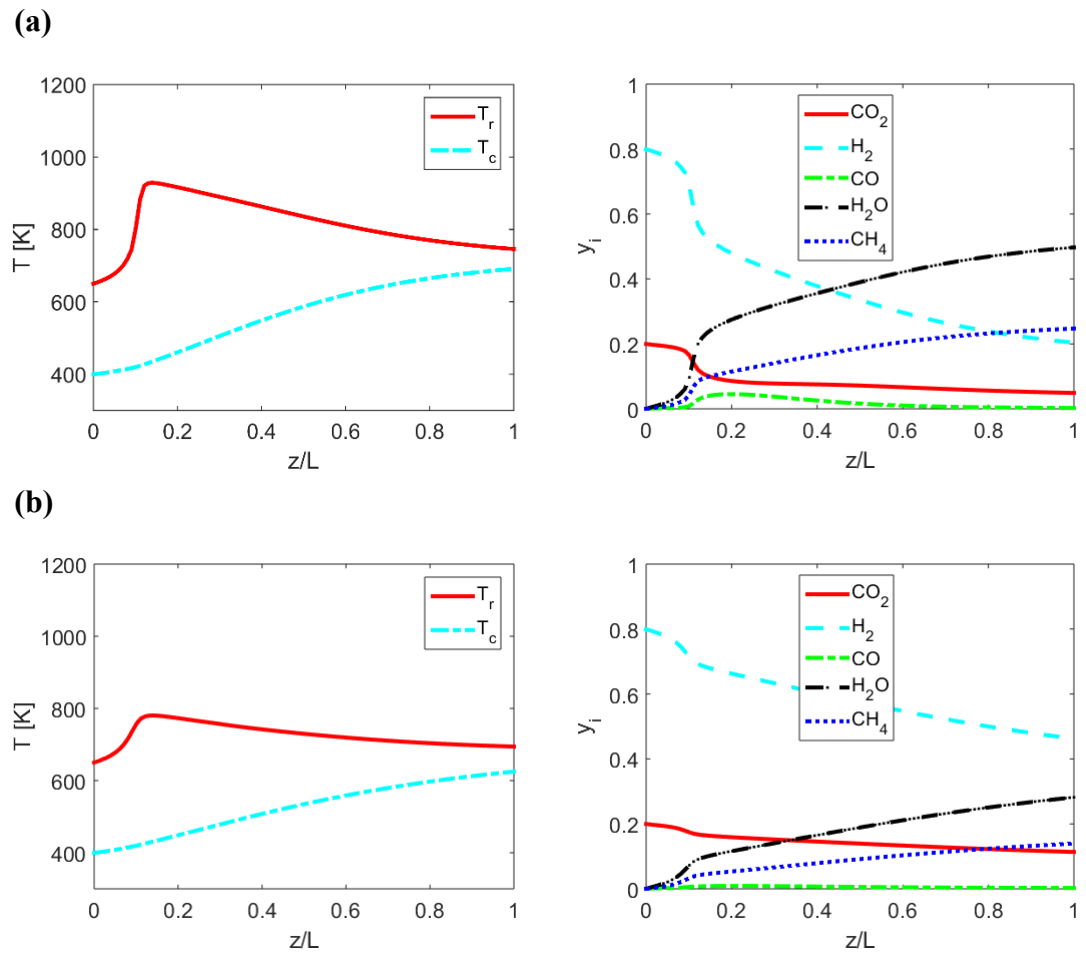


**Fig. 28.** Spatial temperature profiles (left panel) and mole fraction distribution (right panel) for short-term operation, TOS=10 h (a) and long-term operation, TOS=10,000 h (b). $T_r$ and $T_c$ in left panel denote temperatures in the reactor and coolant compartments, respectively; *Parameters:* $P_f = 5$ *bar*, $T_f = 650$ *K*, *GHSV* $= 25{,}000\ h^{-1}$, $G_{MS} = 0.40G_{MS,0}$

### 4.4.1.2 Effect of steam addition

Since deactivation rate is strongly dependent on temperature, as discussed in *Section 4.4.1.1*, feed gas diluted by steam is suggested herein to use for prevention of catalyst deactivation via

suppressing reaction heat and shifting products distribution. Steam is advantageous over other gas, such as inert gas and $N_2$, due to low-cost and recyclability in the methanation system, Eqs. (1-3). Therefore, although the effect of steam gasification, Eq. (6), is not included in the catalyst deactivation kinetics used herein, the addition of steam still can affect the deactivation rate.

The effects of steam addition in feed gas on temperature, mole fractions distributions and catalyst activity are shown in Fig. 29. It can be seen that steam diluting feed gas can suppress reaction and then decrease the temperature, Fig. 29 (upper panel), furthermore, steam addition can change mole fractions distribution via shifting reaction equilibrium, Eqs. (1-3), Fig. 29 (middle panel). In addition, the difference of catalyst activity in Fig. 29 (lower panel) indicates that steam addition in feed gas can prevent catalyst deactivation.

More apparent effects of steam addition on temperature, mole fractions distributions and prevention of catalyst deactivation can be found at high space velocity (SV=25,000 $h^{-1}$) due to more efficient heat removal, Fig. 30. In addition, steam addition preventing the formation of thermal front can lead to nearly isothermal operation of the reactor, also resolving the overheating issues, Fig. 30b (upper panel). Therefore, despite suppressing reaction and decreasing $CH_4$ production, steam addition can prevent catalyst deactivation, leading to longer operation period.

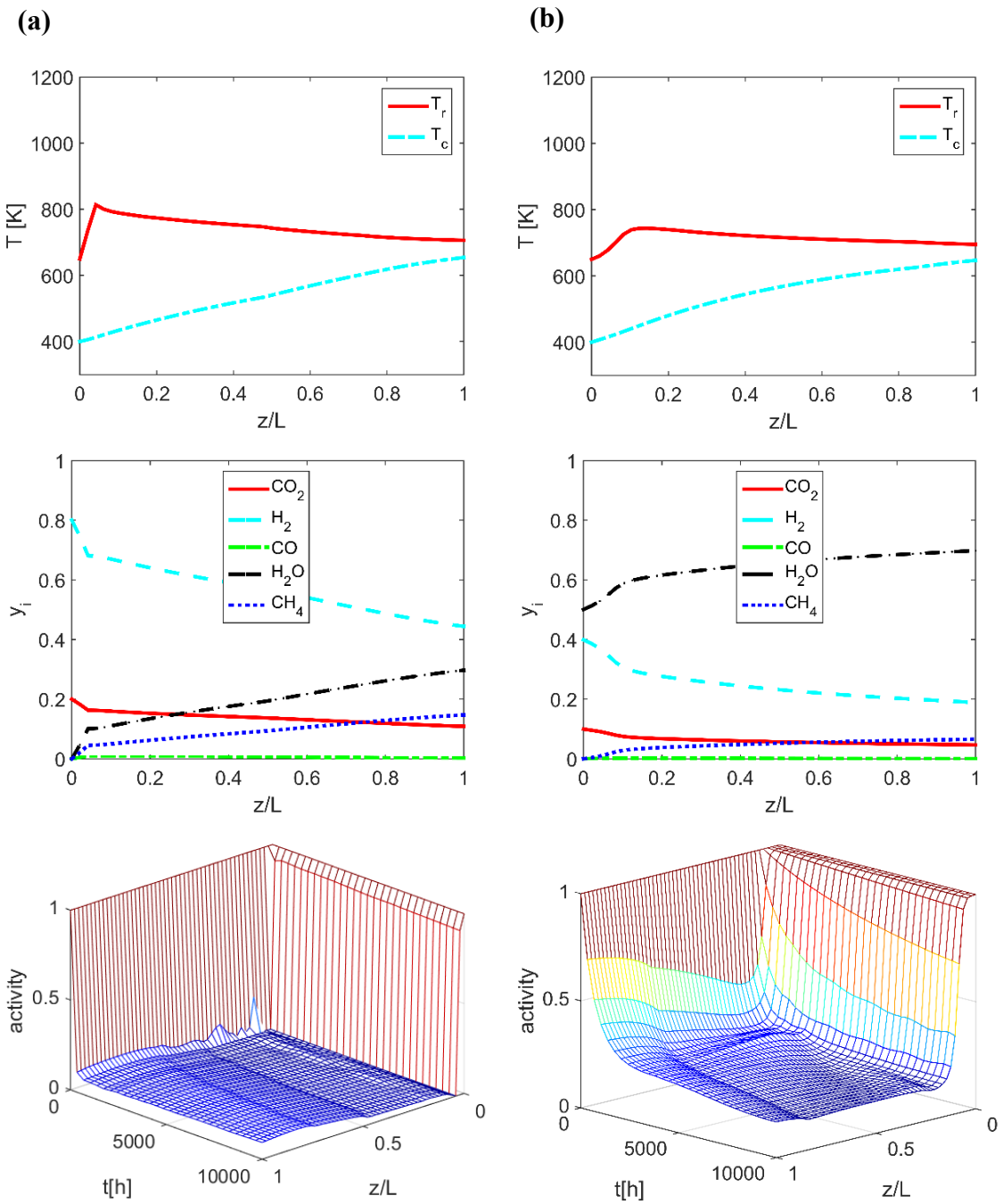


**Fig. 29.** Spatial profiles of temperature and mole fractions and the spatiotemporal profile of catalyst activity at SFMF = 0 (a) and SFMF = 0.5 (b) and GHSV=10,000 $h^{-1}$; *Parameters:* $P_f = 5$ *bar,* $T_f = 650$ *K,* $G_{MS} = 0.40G_{MS,0}$*, TOS = 10,000 h*

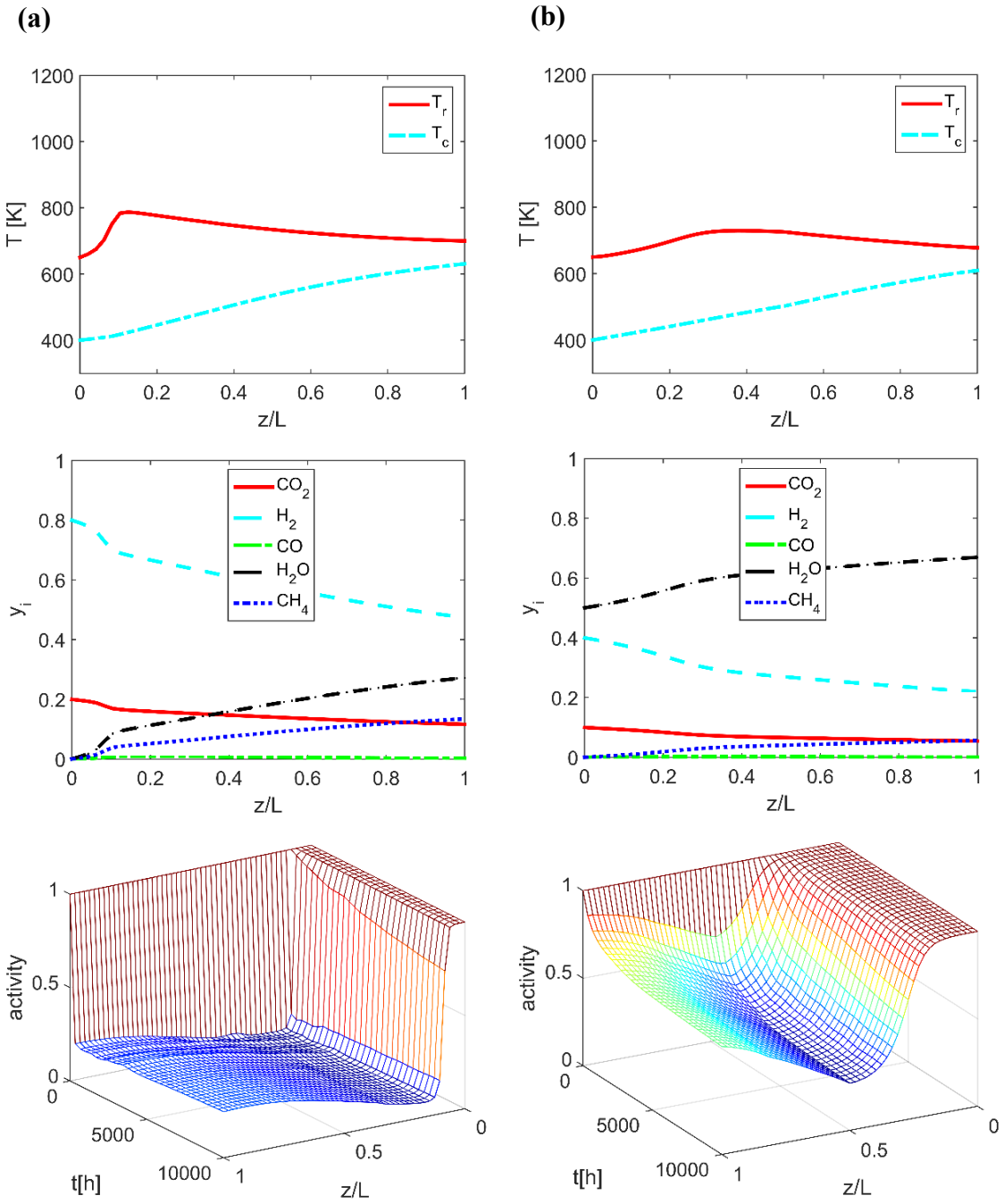


**Fig. 30.** Spatial profiles of temperature and mole fractions and the spatiotemporal profile of catalyst activity at SFMF = 0 (a) and SFMF = 0.5 (b) and GHSV=25,000 $h^{-1}$; *Parameters:* $P_f = 5$ *bar,* $T_f = 650$ *K,* $G_{MS} = 0.40G_{MS,0}$*,* $TOS = 10{,}000$ *h*

The influence of the steam feed mole fraction (SFMF) on $CH_4$ yield is shown in Fig. 31. It can be seen that for the short-term operation (TOS = 100 h), $CH_4$ yield decrease with the increase of SFMF, whereas, for longer term operation (TOS = 1,000 h and TOS = 10,000 h), SFMF influences $CH_4$ yield very slightly, Fig. 31a. In Fig. 31b, it can be seen that the sharp decrease of $CH_4$ yield indicates that deactivation influence reactor performance significantly at SFMF = 0 (i.e. no steam in feed gas), and increasing SFMF from 0 to 0.3 can lead to $CH_4$ yield decrease gradually, indicating steam addition in feed gas can prevent catalyst deactivation. When SFMF is further increased to 0.5, the effect on preventing catalyst deactivation become more apparent. Despite steam addition in feed gas will decrease $CH_4$ yield and the decrease become more significant as SFMF increase, but this negative effect can only influence reactor performance at initial operation period. Therefore, one can conclude that steam addition in feed gas can prevent catalyst deactivation, even though it will reduce the $CH_4$ production for short-term operation, but the decrease is negligible for long-term operation, indicating steam addition in feed gas can extend reactor operation period.

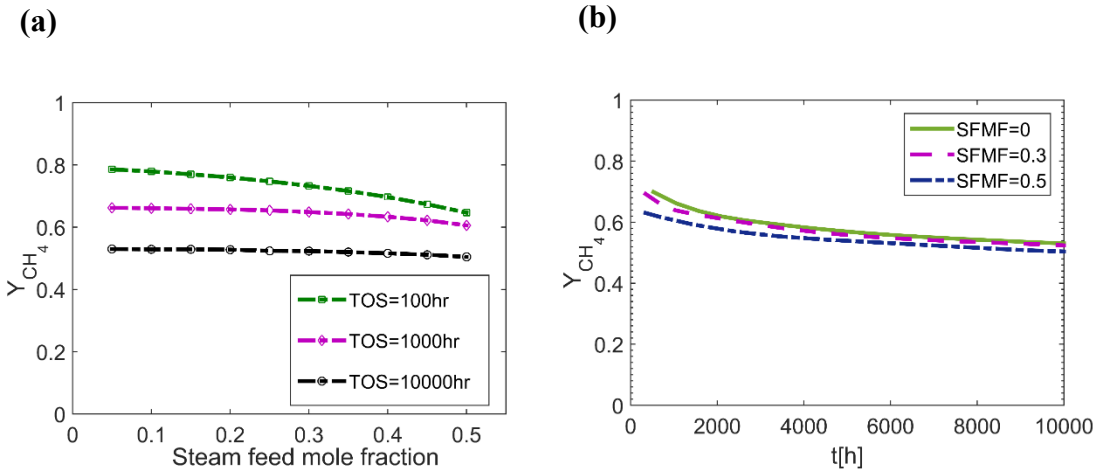


**Fig. 31.** Effect of the steam mole fraction in the feed on $CH_4$ yield (a), and $CH_4$ yield variation with time (b); *Parameters:* $P_f = 5bar$, $T_f = 650K$, $GHSV = 25{,}000\ h^{-1}$, $G_{MS} = 0.40G_{MS,0}$

### 4.4.2 Reactor fed with biogas feed

#### 4.4.2.1 Effect of feed pressure effect

Using raw biogas as a feed could be an attractive alternative to the use of pure $CO_2$ as a feedstock, since it does not require costly $CO_2$ separation; gas clean-up to remove $H_2S$ will be still required. However, raw biogas contains a high fraction of $CH_4$ (~60%) which can cause catalyst deactivation immediately at the reactor entrance due to high partial pressure of $CH_4$ accompanied by a relatively high feed temperature. For biogas feed conditions, feed pressure will affect the $CH_4$ partial pressure affecting the catalyst deactivation rate. In practical applications, processes are frequently conducted at elevated pressures in order to maximize the process throughput.

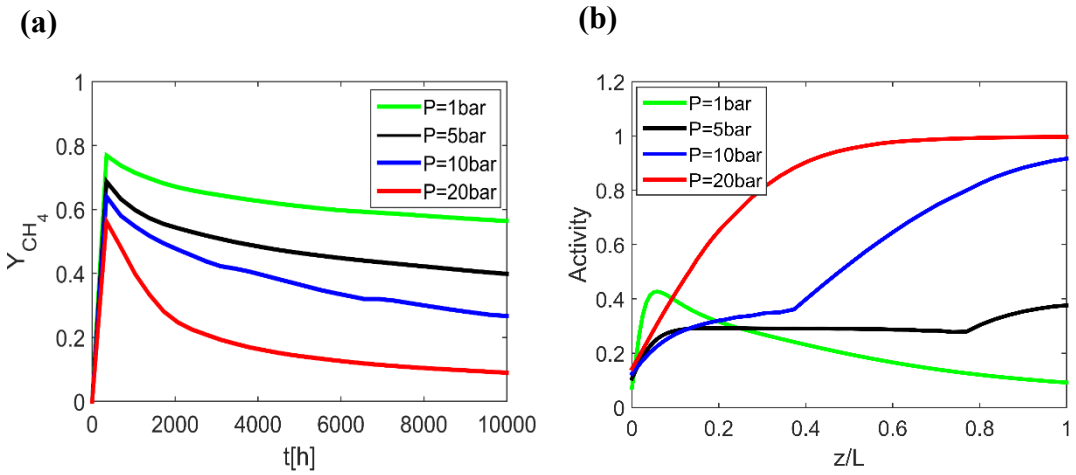


**Fig. 32.** Effect of feed pressure on methane yield (a), and spatial profile of catalyst activity (b); *Parameters: $T_f$ = 700 K, GHSV = 10,000 $h^{-1}$, $G_{MS}$ = 0.40 $G_{MS,0}$, TOS =10,000 h*

Fig. 32 demonstrates the effect of feed pressure on the catalyst activity and reactor performance. It can be seen that increasing of feed pressure results in the $CH_4$ yield decrease and high pressures accelerate the catalyst deactivation, Fig. 32a. Higher pressures increase the gas mixture density resulting in higher molar flow rate for a fixed space velocity. As a result, increasing feed pressure leads to more heat generation and thus higher reactor temperatures that suppress $CH_4$

formation via the exothermic Sabatier reaction. Therefore, though high pressures favor $CH_4$ production according to the equilibrium, Fig. 14, the resulted higher reactor temperatures shift the reaction equilibrium towards less $CH_4$ production, Fig 32a. Moreover, high operating pressures result in high $CH_4$ partial pressure, accelerating catalyst deactivation and reducing the reactor lifetime.

Spatial profiles of the catalyst activity at TOS=10,000 h at various feed pressure are shown in Fig. 32b. At the reactor entrance, catalyst deactivation is significant, due to the high partial $CH_4$ pressure in the reactor feed. At relatively low pressures, catalyst is deactivated in the entire reactor. However, for elevated feed pressures, catalyst activity increases downstream the reactor, which can be attributed to the catalyst regenerated by $H_2$ at low $CH_4$ yields. Low $CH_4$ yields could result from the reactor overcooling; catalyst downstream the reactor is then regenerated by excess $H_2$, leading to the catalyst activity recovery.

#### 4.4.2.3 Effect of space velocity

It is highly desirable to operate reactor at elevated space velocities in order to maximize reactor throughput. However, higher $CH_4$ production will also accelerate catalyst deactivation. In addition, in some cases, high space velocity can result in reactor overcooling, causing reactor extinction, Fig. 22. In Fig. 33, reactor performance is evaluated as a function of space velocity to investigate the effect of high throughput operation on catalyst deactivation. It can be seen that $CH_4$ yield is up to 90% at low space velocity, while increasing space velocity leads to reactor overcooling and, as a result, decreasing $CH_4$ yields, as discussed in *Section 4.3.3*.

The effect of catalyst deactivation is apparent for long-term operation, which can be attributed to decaying catalyst activity, Fig. 33a. At low space velocity (1,000 $h^{-1}$), catalyst deactivation is slower, however, faster deactivation and significant decline in $CH_4$ yield occur as space velocity is increased, Fig. 33b. At SV > 20,000 $h^{-1}$, a larger decrease occurs in $CH_4$ yield due to rapid catalyst deactivation. The corresponding trends of outlet mole fractions (on dry basis) at different space velocities are shown in Fig. 34. Similarly to $CH_4$ yield, $CH_4$ mole fraction decreases with time, and with increasing space velocity which leads to faster catalyst deactivation.

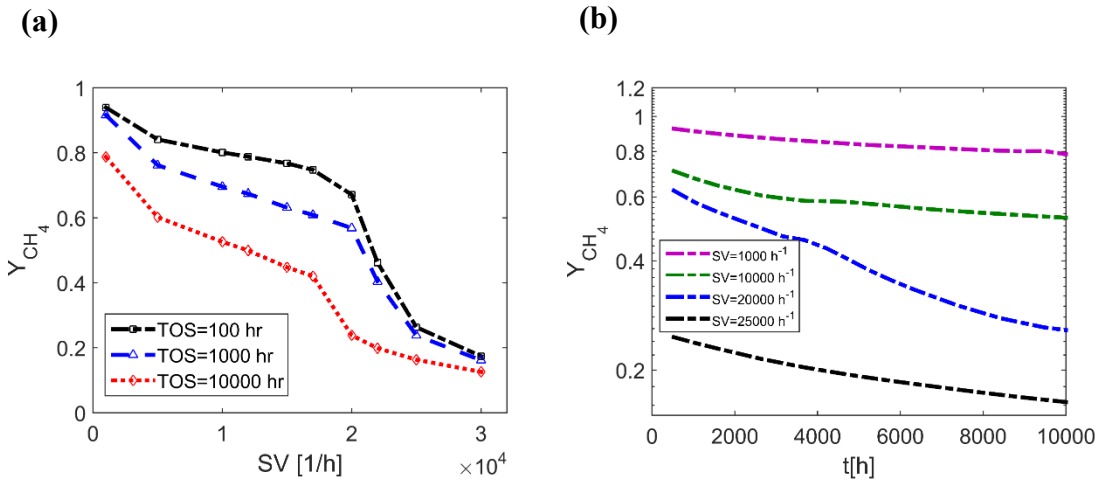


**Fig. 33.** Effect of space velocity on reactor performance (a), and methane yield as a function of operation time (b); *Parameters:* $P_f = 2$ *bar*, $T_f = 650$ *K*, $G_{MS} = 0.40G_{MS,0}$, *TOS = 10,000 h*

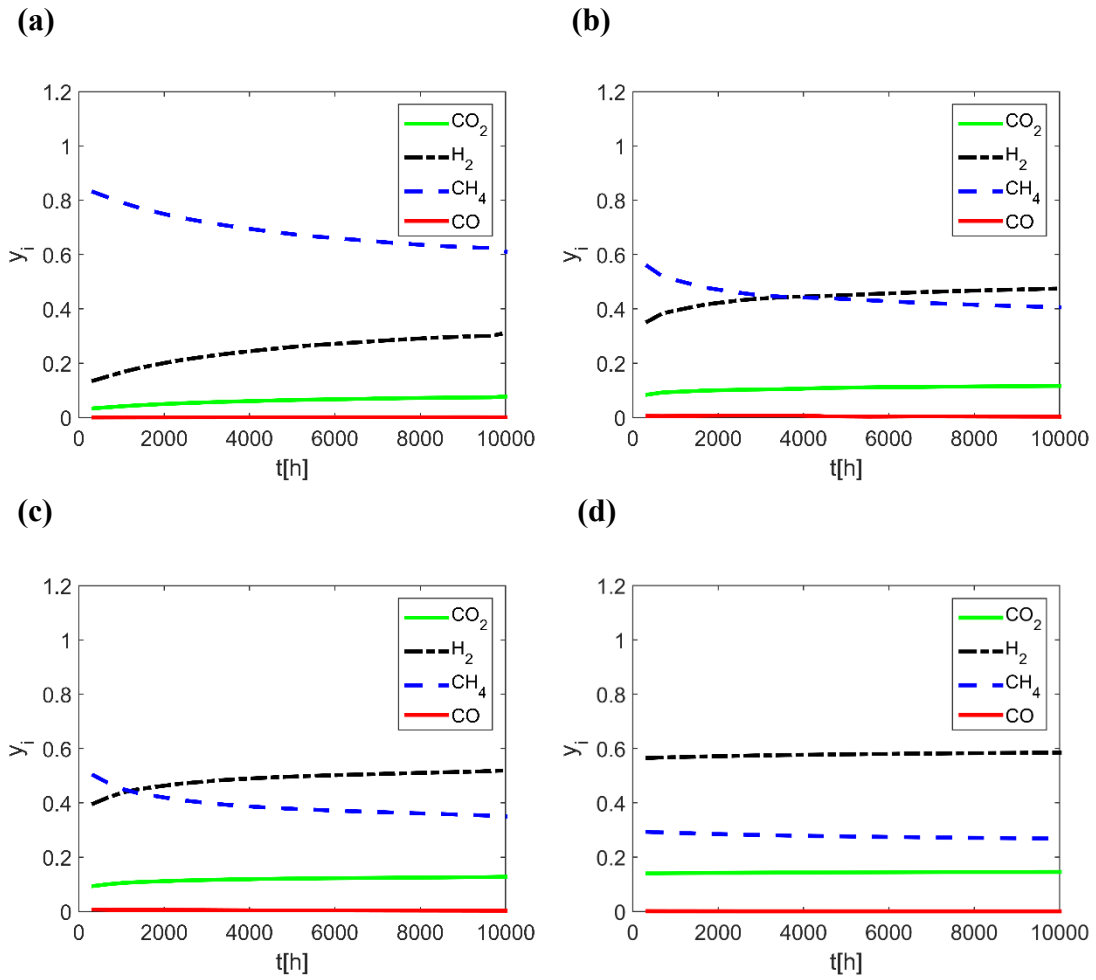


**Fig. 34.** Reactor outlet mole fractions (on dry basis) as a function of time at GHSV = 1,000 $h^{-1}$ (a), GHSV=10,000 $h^{-1}$ (b), GHSV=20,000 $h^{-1}$ (c), GHSV= 25,000 $h^{-1}$ (d); *Parameters:* $P_f = 2bar$, $T_f = 650\ K$, $G_{MS} = 0.40\ G_{MS,0}$, $TOS = 10{,}000\ h$

At relatively low space velocity (GHSV = 1,000 $h^{-1}$) heat removal is very effective, leading to equal temperatures in both the reaction and cooling compartments, except for the small temperature difference at the reactor entrance, Fig. 35a. Despite highly-efficient cooling, catalyst deactivation is still affecting the reactor performance but a relatively higher $CH_4$ production (more than 40% of methane at the reactor outlet) can be achieved under the influence of deactivation even after 10,000 h of operation, Fig. 35b.

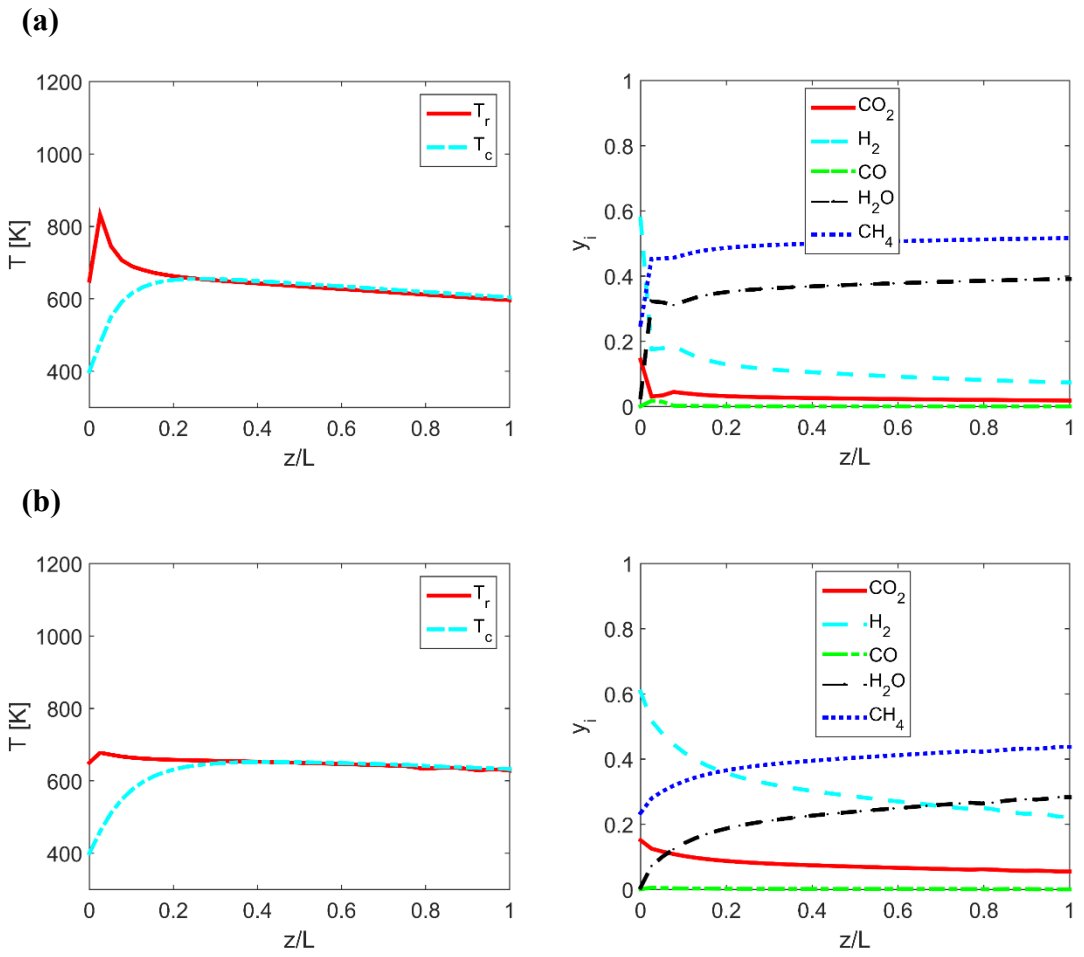


**Fig. 35.** Spatial profiles of temperatures and mole fractions for TOS = 100 h (a) and TOS = 10,000 h (b) and GHSV = 1000 $h^{-1}$; *Parameters:* $P_f = 2$ *bar*, $T_f = 650$ *K*, $G_{MS} = 0.40G_{MS,0}$

For high space velocities (GHSV = 20,000 $h^{-1}$), there is a substantial difference between outlet temperatures, Fig. 36a, indicating insufficient heat removal due to the heat transfer limitations. The higher outlet reactor temperature results in the decrease of $CH_4$ yield and, at the same time, accelerated catalyst deactivation. After 10,000 h of operation, $CH_4$ production is extremely low, Fig. 36b.

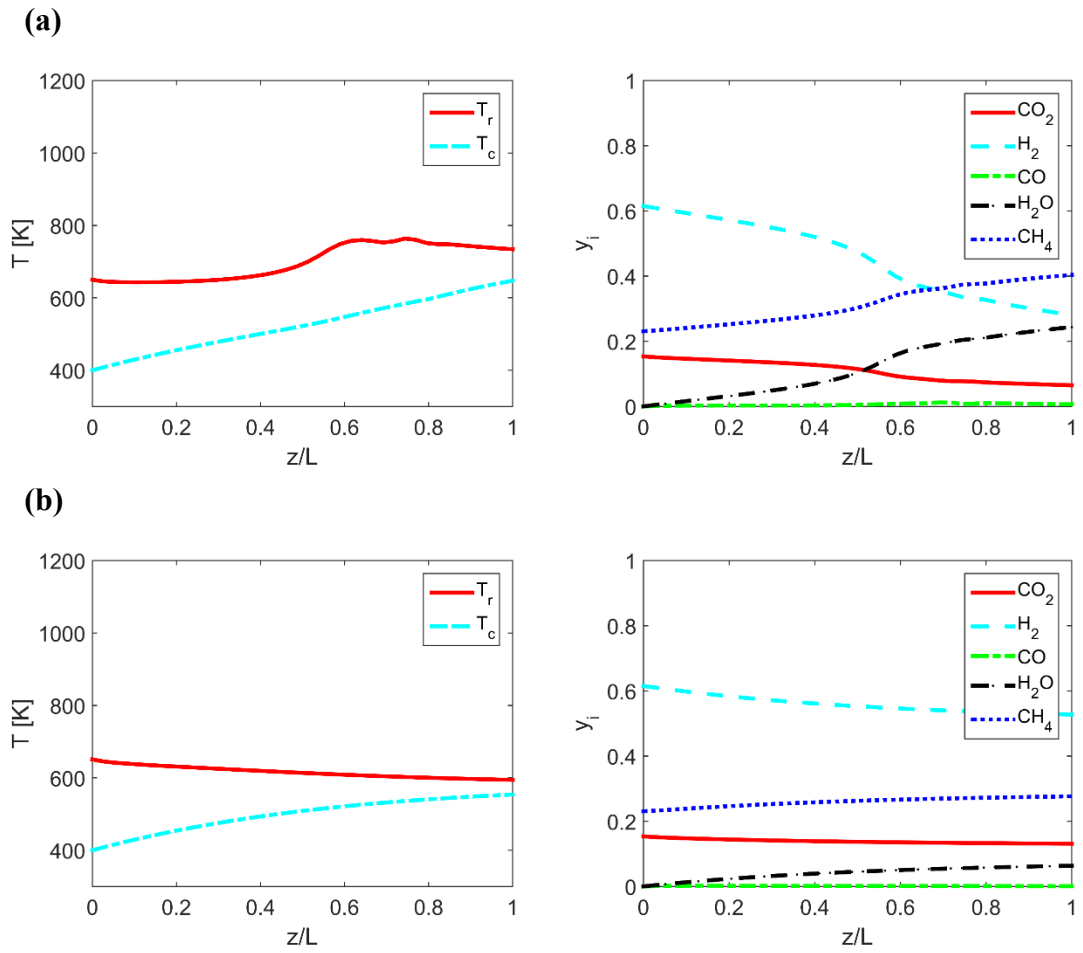


**Fig. 36**. Spatial profiles of temperatures and mole fractions for TOS = 100 h (a) and TOS = 10,000 h (b) and GHSV = 20,000 $h^{-1}$; *Parameters:* $P_f = 2$ *bar*, $T_f = 650$ *K*, $G_{MS} = 0.40G_{MS,0}$

#### 4.4.2.4 Effect of cooling rate

Cooling rate is of vital importance to the improvement of methanation reactor throughput, as discussed in *Section 4.3.4*, but it will also affect catalyst activity. Effective heat removal can decrease reactor temperature favoring $CH_4$ production according to the thermodynamic equilibrium, Fig. 14. However, in some cases increased $CH_4$ production can lead to faster catalyst deactivation due to $CH_4$ cracking and coking of the catalyst surface, as discussed in *Section 4.4.2.3*. Therefore, cooling rate is a crucial parameter for the reactor performance.

In Fig. 37, reactor performance is evaluated as a function of the normalized cooling rate ($G_{MS}/G_{MS,0}$). It can be seen that increasing cooling rate can promote $CH_4$ production due to the effective heat removal. However, above the threshold of $G_{MS}/G_{MS,0} = 0.54$, further increase of the cooling rate results in reduced $CH_4$ yield, which can be seen after TOS = 10,000 h, Fig. 37a; TOS denotes time on stream, i.e. time of operation. In some cases, increasing cooling rate can lead to faster catalyst deactivation, Fig. 37b. High molten salt flow rate leads to efficient heat removal that promotes $CH_4$ production. However, increased $CH_4$ production can also lead to accelerated catalyst deactivation due to methane cracking and carbon deposition. The effect of cooling rate on deactivation at fixed space velocities is analyzed in Fig. 37b. For TOS < 4,000 h, $CH_4$ yield increases with cooling rate, with the highest yield achieved at $G_{MS}/G_{MS,0}$=0.88. However, for TOS > 4000 h, the yield at $G_{MS}/G_{MS,0}$=0.88 drops sharply.

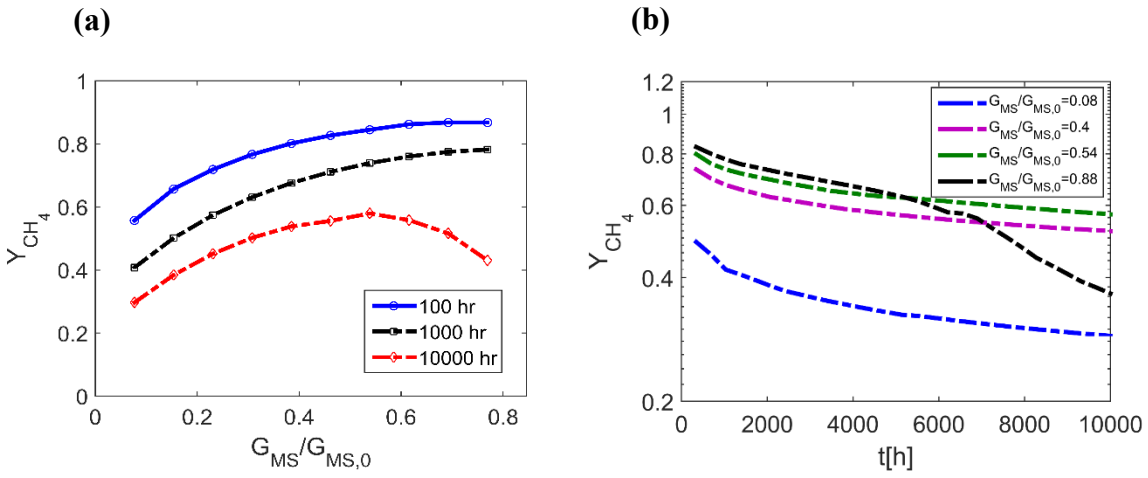


**Fig. 37.** Methane yield as a function of the normalized molten salt flow rate (a), and methane yield variation with operation time (b); *Parameters: $P_f$ = 2 bar, $T_f$ = 650 K, GHSV = 10,000 $h^{-1}$, TOS = 10,000 h*

For the threshold cooling rate of $G_{MS}/G_{MS,0}$=0.54, heat removal is efficient and outlet temperatures are almost equal in the reaction and cooling compartments, leading to 50% of $CH_4$ at the reactor

outlet for TOS = 100 h, Fig. 38a. As cooling rate is further increased to $G_{MS}/G_{MS,0}$=0.88, the reactor performs well at TOS = 100 h, Fig. 39a, but catalyst deactivation become more serious and reaction extinction happens at TOS = 10,000 h due to the rate of heat generation is significantly lower than heat transfer through the walls of the cooling tubes, Fig. 39b.

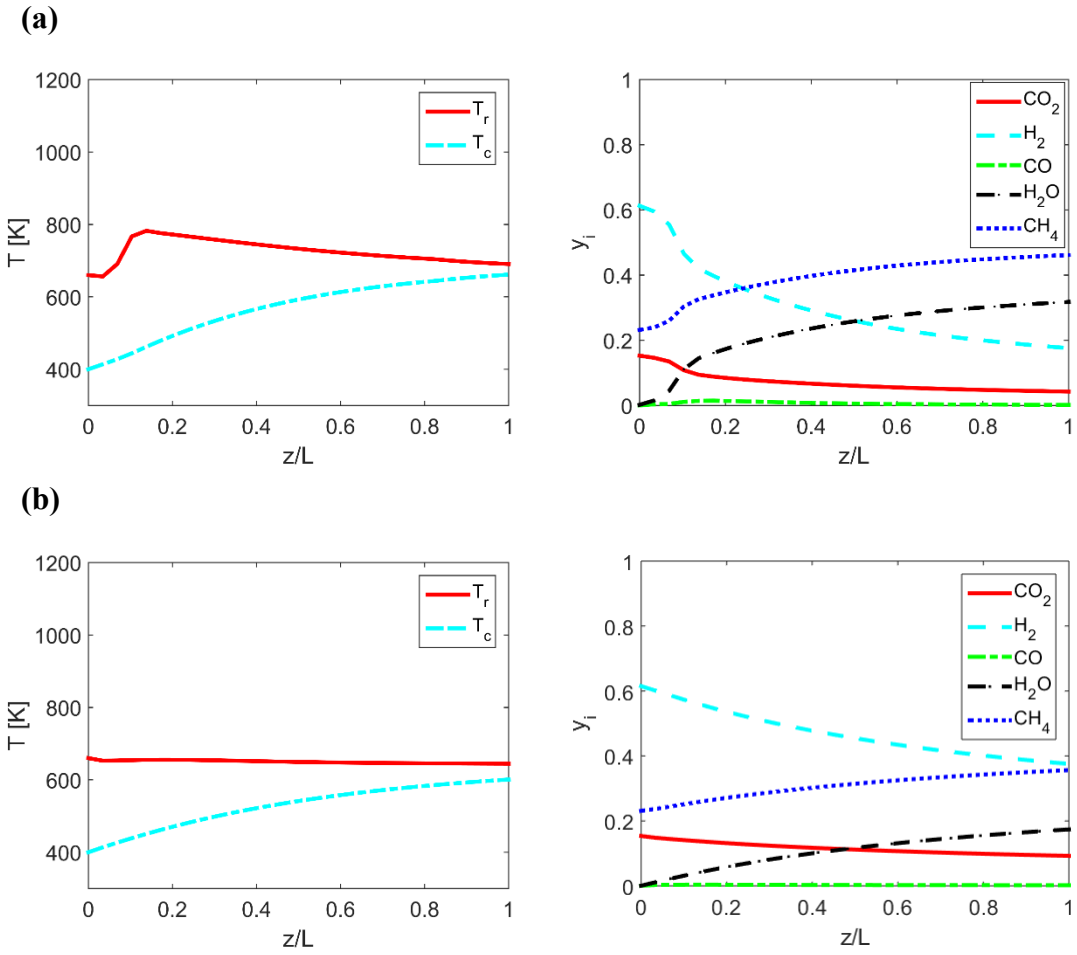


**Fig. 38.** Spatial profiles of temperatures and mole fractions for TOS = 100 h (a) and TOS = 10,000 h (b) and $G_{MS}$ = 0.54$G_{MS,0}$ ; *Parameters:* $P_f$ *= 2 bar,* $T_f$ *= 650 K, GHSV = 10,000* $h^{-1}$

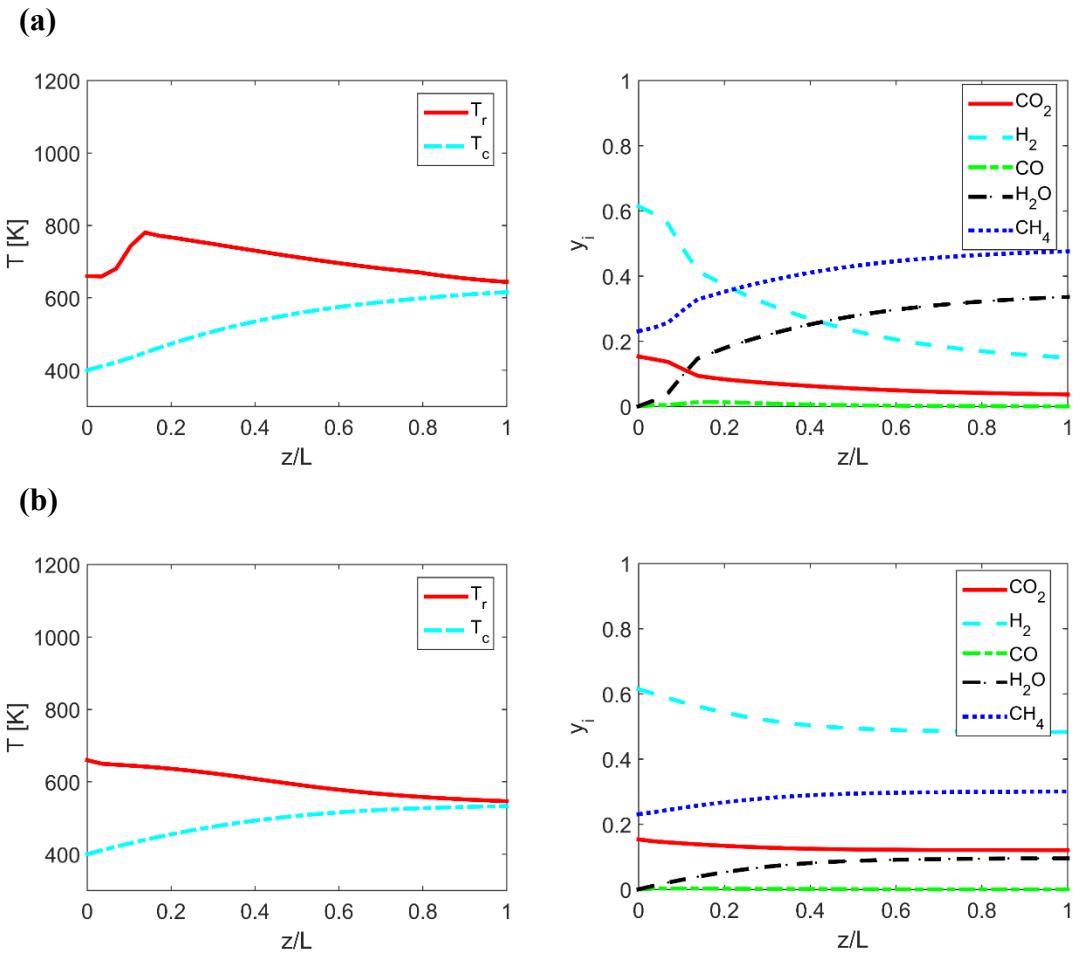


**Fig. 39.** Spatial profiles of temperatures and mole fractions for TOS = 100 h (a) and TOS = 10,000 h (b) and $G_{MS} = 0.88G_{MS,0}$; *Parameters:* $P_f = 2$ *bar*, $T_f = 650$ *K*, *GHSV* = 10,000 $h^{-1}$

#### 4.4.2.5 Optimization of operating parameters

The existence of catalyst deactivation makes the problem of the reactor performance optimization very complicated, since optimum operating conditions can change during the course of reactor operation. The two important and relatively easily adjustable operating conditions are space velocity (reactor throughput) and molten salt flow rate (cooling rate). Elevated space velocities increase reactor throughput, but can lead to short catalyst lifetime requiring frequent catalyst replacement and, thus, increased maintenance cost. On the other hand, for low space velocities,

less $CH_4$ is produced per unit time, but longer reactor service life can be achieved. Increasing molten salt flow rate at a fixed space velocity can increase $CH_4$ yield by improving heat removal, but more $CH_4$ production can accelerate catalyst deactivation and decrease reactor service life. Therefore, elevated cooling rates are not always adaptable for long-term operation. In addition, high molten salt flow rate is not desirable for elevated space velocities due to reactor overcooling, Fig. 39b. Therefore, optimization of operation parameters at various conditions is crucial for reactor performance improvement.

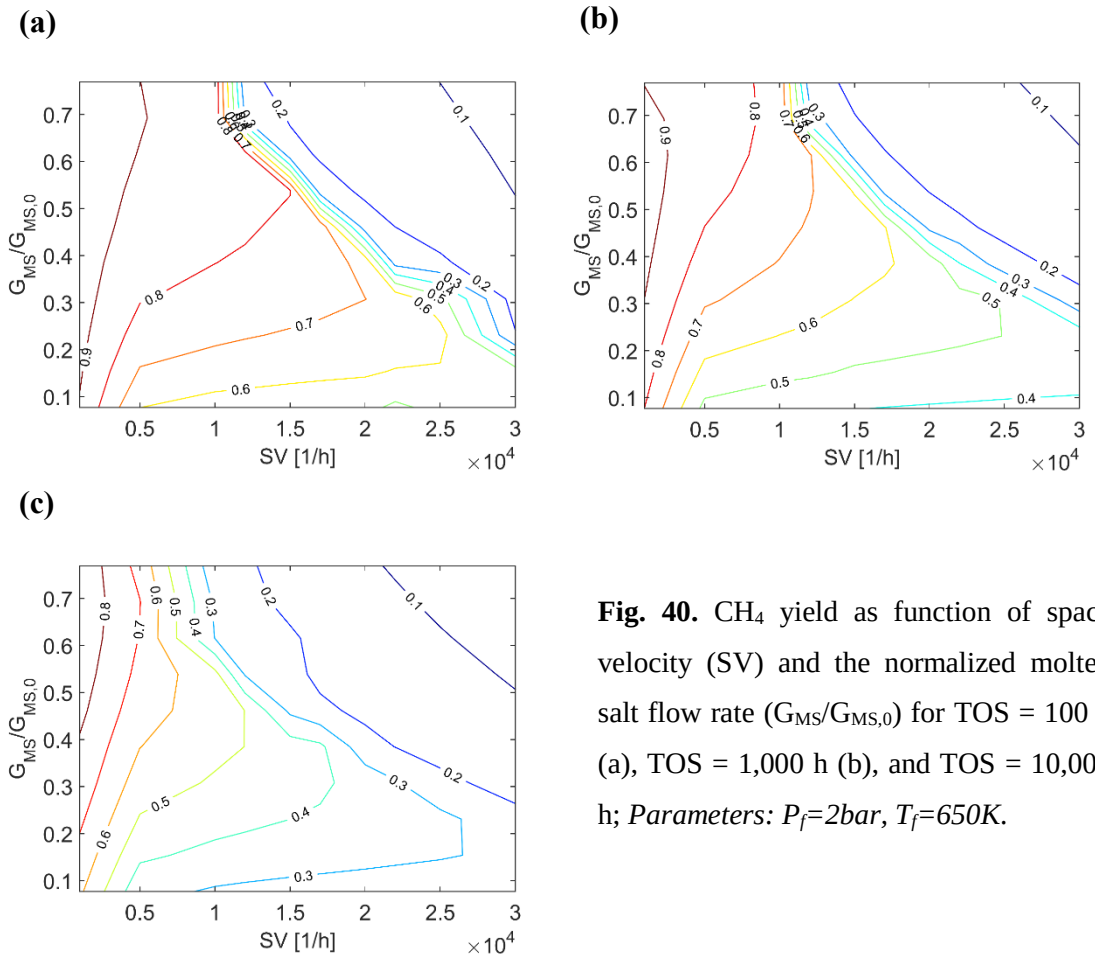


**Fig. 40.** $CH_4$ yield as function of space velocity (SV) and the normalized molten salt flow rate ($G_{MS}/G_{MS,0}$) for TOS = 100 h (a), TOS = 1,000 h (b), and TOS = 10,000 h; *Parameters: $P_f$=2bar, $T_f$=650K.*

In Fig. 40, $CH_4$ yield is evaluated as a function of the space velocity (SV) and normalized molten salt flow rate ($G_{MS}/G_{MS,0}$). It was found that even though $CH_4$ yield is relatively low, elevated space velocities (20,000 $h^{-1}$ – 25,000 $h^{-1}$) are still recommended for short-term operation in order to maximize $CH_4$ production per unit time. At high space velocities, relatively lower cooling rate ($0.2 < G_{MS}/G_{MS,0} < 0.4$) is necessary for ensuring a high $CH_4$ yield (~60%) and avoiding reactor overcooling, Fig. 40a. When TOS is up to 1,000 h, high $CH_4$ yield (more than 50%) is still achievable at elevated space velocities with relatively lower cooling rate, Fig. 40b. However, as TOS is further increased up to 10,000 h, $CH_4$ yield is decreased to around 30%, Fig. 40c, which indicates that elevated space velocities are not adaptable for long-term operation due to rapid catalyst deactivation.

At low space velocities, $CH_4$ yield increases with molten salt flow rate and decreases very slightly (~10%) as TOS increases from 100 h to 10,000 h, Fig. 40a and Fig. 40c. Therefore, low space velocities with high molten salt flow rate are recommended to be applied for long-term operation due to higher $CH_4$ yield and longer reactor service life.

For the intermediate region of space velocities, $CH_4$ yield increases with cooling rate, and after the threshold of cooling rate, increasing molten salt flow rate further will decrease $CH_4$ yield due to reactor overcooling. At the same time, higher molten salt flow rate for the intermediate space velocities will accelerate catalyst deactivation due to more methane production, resulting in short reactor service time, as discussed in *Section 4.4.2.4*. Therefore, relatively low cooling rate (e.g. $G_{MS}/G_{MS,0} \sim 0.4$) is recommended for long-term operation at intermediate space velocities, because lower molten salt space velocity can reduce operation cost and increase operation period.

To summarize the findings discussed above, one can conclude that space velocity and cooling rate (molten slat flow rate) are crucial parameters affecting the reactor performance and catalyst activity. Elevated space velocities with low cooling rates are recommended to apply for short-term operations, and relatively lower space velocities with higher cooling rates are beneficial for long-term operations. Moderately elevated space velocities (GHSV $\approx$ 10,000 $h^{-1}$) with intermediate cooling rates ($G_{MS} \approx 0.4G_{MS,0}$) are the most appropriate from the point of view of both short-term and long-term operation.

## 5. Concluding remarks

The molten salt-cooled heat exchanger type packed bed reactor was suggested as a novel design configuration for synthetic methane production via Sabatier reaction. A mathematical model was defined and analyzed using numerical simulations in order to determine the effects of operating parameters and to find optimal operation regimes. The reactor performance was evaluated in terms of $CO_2$ conversion and $CH_4$ yield, as a function of various parameters including feed temperature, space velocity and cooling rate, which were found to be of crucial importance for the reactor performance. The simulations predicted that under certain optimized operating conditions it is possible to obtain $CH_4$ yields of more than 90% at elevated, industrially relevant space velocities.

Optimizing the rate of cooling, i.e. the molten salt flow rate, is a challenging task. On one hand, high cooling rates produce a declining temperature profile in the packed bed which is beneficial from the thermodynamic point of few: low temperatures facilitate methane formation in the exothermic Sabatier reaction. On the other hand, overcooling can lead to a sharp performance drop and even to reactor extinction. Low cooling rates should be avoided because they result in exceedingly high temperatures that negatively affect $CH_4$ formation and can lead, in a practical situation, to the thermal decomposition of the molten salt. Increasing space velocity is beneficial from the point of view of increased reactor throughputs and, therefore, higher rate of $CH_4$ production. However, high space velocities can lead to reactor extinction in a threshold-like manner similar to the effect of the overcooling by molten salt.

The effect of catalyst deactivation on the reactor performance was also investigated, by evaluating reactor performance as a function of the simulated time-on-stream, while accounting for catalyst deactivation by methane cracking and carbon deposition on the catalytic surface. It was found that feed pressure, space velocity and cooling rate (molten salt flow rate) are the most crucial parameters affecting the rate of catalyst deactivation. High pressures, which are favorable for methane production according to the equilibrium, actually causes faster catalyst deactivation. This rather complicated phenomenon results from several competing contributions, including the effect of high gas density and higher partial pressure of methane that promote catalyst deactivation and the positive effect of pressure on the equilibrium methane production. Elevated space velocities with low cooling rates are recommended to be applied for short term operations, while relatively lower space velocities with higher cooling rates are beneficial for long-term operation.

A preliminary techno-economic evaluation predicted renewable natural gas (RNG) production costs below 20 $/GJ, for multiple reactors and the optimized cooling rate and reactor throughput. Most of the energy content of $H_2$ consumed in the reaction is recovered in RNG produced and electricity co-generated (up to 80%). Since renewable $H_2$ produced in a distributed manner is less suitable for storage and transportation, converting it into RNG could be an attractive avenue. The most significant contribution to the production cost of RNG is expected to be the price of renewable $H_2$. Therefore, reducing the production cost of renewable $H_2$ can lead to a widespread introduction of RNG into the markets.

# Reference


[1] B. Kumar, M. Llorente, J. Froehlich, T. Dang, A. Sathrum, C.P. Kubiak, Photochemical and photoelectrochemical reduction of $CO_2$, Annu. Rev. Phys. Chem. 63 (2012) 541–569.
[2] Y. Chen, N.S. Lewis, C. Xiang, Operational constraints and strategies for systems to effect the sustainable, solar-driven reduction of atmospheric $CO_2$, Energy Environ. Sci. 8 (2015) 3663-3674.
[3] W. Wang, S. Wang, X. Ma, J. Gong, Recent advances in catalytic hydrogenation of carbon dioxide, Chem. Soc. Rev. 40 (2011) 3703–3727.
[4] W. Wang, J. Gong, Methanation of carbon dioxide: an overview, Front. Chem. Sci. Eng. 5 (2011) 2-10.
[5] J. Kopyscinski, T.J. Schildhauer, S.M.A. Biollaz, Production of synthetic natural gas (SNG) from coal and dry biomass – a technology review from 1950 to 2009, Fuel 89 (2010) 1763-1783.
[6] T. Schaaf, J. Grünig, M.R. Schuster, T. Rothenfluh, A. Orth, Methanation of CO2 - storage of renewable energy in a gas distribution system, Energy Sustain. Soc. 4 (2014).
[7] D. Schlereth, O. Hinrichsen, A fixed-bed reactor modeling study on the methanation of $CO_2$, Chem. Eng. Res. Des. 92 (2014) 702-712.
[8] L. Kiewidt, J. Thöming, Predicting optimal temperature profiles in single-stage fixed-bed reactors for $CO_2$-methanation, Chem. Eng. Sci. 132 (2015) 59-71.
[9] S.A.M. Said, D.S.A. Simakov, M. Waseeuddin, Y. Roman-Leshkov, Solar molten salt heated membrane reformer for natural gas upgrading and hydrogen generation: A CFD model, Sol. Energy 124 (2016) 163-176.
[10] G. Gahleitner, Hydrogen from renewable electricity: an international review of power-to-gas pilot plants for stationary applications, Int. J. Hydrogen Energ. 38 (2013) 2039-2061.
[11] M. Götz, J. Lefebvre, F. Mörs, A. McDaniel Koch, F. Graf, S. Bajohr, R. Reimert, T. Kolb, Renewable power-to-gas: a technological and economic review, Renew. Energ. 85 (2016) 1371-1390.
[12] J.H. Chiang, J.R. Hopper, Kinetics of the hydrogenation of carbon dioxide over supported nickel, Ind. Eng. Chem. Prod. Res. Dev. 22 (1983) 225-228.
[13] G.D. Weatherbee, C.H. Bartholomew, Hydrogenation of CO2 on group VIII metals: II. Kinetics and mechanism of CO2 hydrogenation on nickel, J. Catal. 77 (1982) 460-472.
[14] S. Fujita, H. Terunuma, M. Nakamura, N. Takezawa, Mechanisms of methanation of carbon monoxide and carbon dioxide over nickel, Ind. Eng. Chem. Res. 30 (1991) 1146-1151.
[15] F. Logist, I.Y. Smets, J.F. Van Impe, Derivation of generic optimal reference temperature profiles for steady-state exothermic jacketed tubular reactors, J. Process Contr 18 (2008) 92-104.
[16] I. Smets, Dochain, D., & Van Impe, J., Optimal temperature control of a steady-state exothermic plug-flow reactor, AIChE J. 48 (2002) 279-286.
[17] I. Kiendl, M. Klemm, A. Clemens, A. Herrman, Dilute gas methanation of synthesis gas from biomass gasification, Fuel 123 (2014) 211-217.
[18] Y.-L. Kao, P.-H. Lee, Y.-T. Tseng, I.L. Chien, J.D. Ward, Design, control and comparison of fixed-bed methanation reactor systems for the production of substitute natural gas, J. Taiwan Inst. Chem. Eng. 45 (2014) 2346-2357.
[19] J. Strakey, A. Forney, W. Haynes, Methanation in coal gasification processes, Pittsburgh Energy Research Center, Pittsburgh (1975).
[20] J. Panek, J. Grasser, Practical experience gained during the first twenty years of operation of the great plains gasification plant and implications for future projects, US Department of Energy-Office of Fossil Energy, Washington (2006).
[21] H. Topsoe, From solid fuels to substitute natural gas (SNG) using TREMP, Technocal Report, Halder Topsoe (2009).

[22] G. White, The RMProcess-A methanation system, Proceedings of ninth synthetic pipeline gas symposium, Chicago, American Gas Association, 1977, pp. 129-135.
[23] M.V. Twigg, M. Twigg, Catalyst handbook, CSIRO1989.
[24] M. Sudiro, A. Bertucco, Synthetic natural gas (SNG) from coal and biomass: a survey of existing process technologies, open issues and perspectives, INTECH Open Access Publisher, 2010.
[25] R. Lohmüller, Methansynthese mit kombinierten isothermen und adiabaten Reaktoren, Berichte aus Technik und Wissenschaft (1977).
[26] K.P. Brooks, J. Hu, H. Zhu, R.J. Kee, Methanation of carbon dioxide by hydrogen reduction using the Sabatier process in microchannel reactors, Chem. Eng. Sci. 62 (2007) 1161-1170.
[27] M. Sudiro, A. Bertucco, G. Groppi, E. Tronconi, Simulation of a structured catalytic reactor for exothermic methanation reactions producing synthetic natural gas, Comput. Aided Chem. Eng. 28 (2010) 691-696.
[28] J. Li, L. Zhou, P. Li, Q. Zhu, J. Gao, F. Gu, F. Su, Enhanced fluidized bed methanation over a Ni/Al2O3 catalyst for production of synthetic natural gas, Chem. Eng. J. 219 (2013) 183-189.
[29] M.C. Seemann, T.J. Schildhauer, S.M. Biollaz, Fluidized bed methanation of wood-derived producer gas for the production of synthetic natural gas, Ind. Eng. Chem. Res. 49 (2010) 7034-7038.
[30] J. Kopyscinski, T.J. Schildhauer, S.M. Biollaz, Fluidized-Bed methanation: Interaction between kinetics and mass transfer, Ind. Eng. Chem. Res. 50 (2010) 2781-2790.
[31] W. Lommerzheim, C. Flockenhaus, One stage combined shift-conversion and partial methanation process for upgrading synthesis gas to pipeline quality, Proceeding of tenth synthetic pipeline gas symposium, Chicago, American Gas Association, 1978, pp. 439-451.
[32] J. Kopyscinski, T.J. Schildhauer, S.M.A. Biollaz, Methanation in a fluidized bed reactor with high initial CO partial pressure: Part I—Experimental investigation of hydrodynamics, mass transfer effects, and carbon deposition, Chem. Eng. Sci. 66 (2011) 924-934.
[33] D. Kunii, O. Levenspiel, Fluidization EngineeringButterworth Heinemann series in Chemical Engineering, 1991.
[34] M. Götz, F. Ortloff, R. Reimert, O. Basha, B.I. Morsi, T. Kolb, Evaluation of Organic and Ionic Liquids for Three-Phase Methanation and Biogas Purification Processes, Energ. Fuel 27 (2013) 4705-4716.
[35] J. Lefebvre, M. Götz, S. Bajohr, R. Reimert, T. Kolb, Improvement of three-phase methanation reactor performance for steady-state and transient operation, Fuel Process. Technol. 132 (2015) 83-90.
[36] M. Götz, J. Lefebvre, D. Schollenberger, S. Bajohr, R. Reimert, T. Kolb, Novel methanation concepts for the production of Substitute Natural Gas.
[37] C. Bartholomew, Catalyst deactivation and regeneration, Kirk-Othmer Encyc. Chem. Technol (2003).
[38] G.D. Weatherbee, C.H. Bartholomew, Hydrogenation of CO2 on group VIII metals: IV. Specific activities and selectivities of silica-supported Co, Fe, and Ru, J. Catal 87 (1984) 352-362.
[39] Y. Zhang, G. Jacobs, D.E. Sparks, M.E. Dry, B.H. Davis, CO and CO 2 hydrogenation study on supported cobalt Fischer–Tropsch synthesis catalysts, Catal. today 71 (2002) 411-418.
[40] P.J. Lunde, F.L. Kester, Carbon dioxide methanation on a ruthenium catalyst, Ind. Eng. Chem. Proc. DD 13 (1974) 27-33.
[41] K.R. Thampi, J. Kiwi, M. Graetzel, Methanation and photo-methanation of carbon dioxide at room temperature and atmospheric pressure, Nature 327 (1987) 506-508.
[42] F. Solymosi, A. Erdöhelyi, T. Bansagi, Methanation of CO 2 on supported rhodium catalyst, J. Catal 68 (1981) 371-382.
[43] G.A. Mills, F.W. Steffgen, Catalytic Methanation, Cataly. Rev 8 (2006) 159-210.
[44] J. Gao, Q. Liu, F. Gu, B. Liu, Z. Zhong, F. Su, Recent advances in methanation catalysts for the production of synthetic natural gas, RSC Adv. 5 (2015) 22759-22776.

[45] M. Agnelli, M. Kolb, C. Mirodatos, CO hydrogenation on a nickel catalyst.: 1.kinetics and modeling of a low-temperature sintering process, J. Catal 148 (1994) 9-21.
[46] H. Gierlich, M. Fremery, A. Skov, J. Rostrup-Nielsen, Deactivation phenomena of a Ni-based catalyst for high temperature methanation, Stud. in Surf. Sci. Catal. 6 (1980) 459-469.
[47] S. Appari, V.M. Janardhanan, R. Bauri, S. Jayanti, Deactivation and regeneration of Ni catalyst during steam reforming of model biogas: An experimental investigation, Int.l J. Hydrogen Energ. 39 (2014) 297-304.
[48] C. Bartholomew, G. Weatherbee, G. Jarvi, Sulfur poisoning of nickel methanation catalysts: I. in situ deactivation by H2S of nickel and nickel bimetallics, J Catal 60 (1979) 257-269.
[49] R.P. Struis, T.J. Schildhauer, I. Czekaj, M. Janousch, S.M. Biollaz, C. Ludwig, Sulphur poisoning of Ni catalysts in the SNG production from biomass: A TPO/XPS/XAS study, Appl. Catal. A- Gen 362 (2009) 121-128.
[50] K. Nikooyeh, R. Clemmer, V. Alzate-Restrepo, J.M. Hill, Effect of hydrogen on carbon formation on Ni/YSZ composites exposed to methane, Appl. Catal. A-Gen. 347 (2008) 106-111.
[51] F. Frusteri, L. Spadaro, F. Arena, A. Chuvilin, TEM evidence for factors affecting the genesis of carbon species on bare and K-promoted Ni/MgO catalysts during the dry reforming of methane, Carbon 40 (2002) 1063-1070.
[52] M.N. Pedernera, J. Pina, D.O. Borio, Kinetic evaluation of carbon formation in a membrane reactor for methane reforming, Chem. Eng. J. 134 (2007) 138-144.
[53] J.B. Claridge, M.L. Green, S.C. Tsang, A.P. York, A.T. Ashcroft, P.D. Battle, A study of carbon deposition on catalysts during the partial oxidation of methane to synthesis gas, Catal Lett 22 (1993) 299-305.
[54] J.-W. Snoeck, G. Froment, M. Fowles, Steam/CO2 reforming of methane. carbon filament formation by the Boudouard reaction and gasification by CO2, by H2, and by steam: kinetic study, Ind. Eng. Chem. Res. 41 (2002) 4252-4265.
[55] M. Borghei, R. Karimzadeh, A. Rashidi, N. Izadi, Kinetics of methane decomposition to CO x-free hydrogen and carbon nanofiber over Ni–Cu/MgO catalyst, Int. J Hydrogen Energ. 35 (2010) 9479-9488.
[56] M. Ermakova, D.Y. Ermakov, G. Kuvshinov, L. Plyasova, New nickel catalysts for the formation of filamentous carbon in the reaction of methane decomposition, J. Catal. 187 (1999) 77-84.
[57] J.R. Rostrup-Nielsen, Steam reforming catalysts: an investigation of catalysts for tubular steam reforming of hydrocarbons: a contribution from the Research Laboratory of Haldor Topsøe A/S, Teknisk Forlag1975.
[58] M. Krämer, K. Stöwe, M. Duisberg, F. Müller, M. Reiser, S. Sticher, W. Maier, The impact of dopants on the activity and selectivity of a Ni-based methanation catalyst, Appl. Catal. A-Gen. 369 (2009) 42-52.
[59] Z. Kowalczyk, K. Stołecki, W. Rarog-Pilecka, E. Miśkiewicz, E. Wilczkowska, Z. Karpiński, Supported ruthenium catalysts for selective methanation of carbon oxides at very low CO x/H 2 ratios, Appl. Catal. A-Gen. 342 (2008) 35-39.
[60] K.-P. Yu, W.-Y. Yu, M.-C. Kuo, Y.-C. Liou, S.-H. Chien, Pt/titania-nanotube: A potential catalyst for CO 2 adsorption and hydrogenation, Appl. Catal. B-Environ. 84 (2008) 112-118.
[61] B. Hou, Y. Huang, X. Wang, X. Yang, H. Duan, T. Zhang, Optimization and simulation of the Sabatier reaction process in a packed bed, AIChE J. 62 (2016) 2879-2892.
[62] D.S.A. Simakov, M. Sheintuch, Design of a thermally balanced membrane reformer for hydrogen production, AIChE J. 54 (2008) 2735-2750.
[63] D.S.A. Simakov, M. Sheintuch, Model-based optimization of hydrogen generation by methane steam reforming in autothermal packed-bed membrane reformer, AIChE J. 57 (2011) 525-541.
[64] R. Güttel, Study of unsteady-state operation of methanation by modeling and simulation, Chem. Eng. Technol. 36 (2013) 1675–1682.

[65] J. Xu, G.F. Froment, Methane steam reforming, methanation and water‐gas shift: I. intrinsic kinetics, AIChE J. 35 (1989) 88-96.
[66] S.S.E.H. Elnashaie, A.M. Adris, A.S. Al-Ubaid, M.A. Soliman, On the non-monotonic behaviour of methane—steam reforming kinetics, Chem. Eng. Sci. 45 (1990) 491-501.
[67] M.L. Rodríguez, M.N. Pedernera, D.O. Borio, Two dimensional modeling of a membrane reactor for ATR of methane, Catal. Today 193 (2012) 137-144.
[68] G.F. Froment, K.B. Bischoff, Chemical Reactor Analysis and Design, Wiley, New York, 1979.
[69] Z. Chen, Y. Yan, S.S. Elnashaie, Hydrogen production and carbon formation during the steam reformer of heptane in a novel circulating fluidized bed membrane reformer, Ind. Eng. Chem. Res. 43 (2004) 1323-1333.
[70] J.-W. Snoeck, G. Froment, M. Fowles, Kinetic study of the carbon filament formation by methane cracking on a nickel catalyst, J. Catal. 169 (1997) 250-262.
[71] J.-W. Snoeck, G. Froment, M. Fowles, Filamentous carbon formation and gasification: thermodynamics, driving force, nucleation, and steady-state growth, J. Catal. 169 (1997) 240-249.
[72] M.N. Uddin, W.W. Daud, H.F. Abbas, Kinetics and deactivation mechanisms of the thermal decomposition of methane in hydrogen and carbon nanofiber Co-production over Ni-supported Y zeolite-based catalysts, Energ. Convers. Manage. 87 (2014) 796-809.
[73] A. Amin, W. Epling, E. Croiset, Reaction and deactivation rates of methane catalytic cracking over Nickel, Ind. Eng. Chem. Res. 50 (2011) 12460-12470.
[74] M. Demicheli, E. Ponzi, O. Ferretti, A. Yeramian, Kinetics of carbon formation from CH 4-H 2 mixtures on nickel-alumina catalyst, Chem. Eng. J. 46 (1991) 129-136.
[75] R.J. Berger, J. Pérez-Ramírez, F. Kapteijn, A. Moulijn, Catalyst performance testing: radial and axial dispersion related to dilution in fixed-bed laboratory reactors, Appl. Catal. A Gen. 227 (2002) 321-333.
[76] A.G. Dixon, D.L. Cresswell, Theoretical prediction of effective heat transfer parameters in packed beds., AIChE J. 25 (1979) 663-676.
[77] O.R. Derkx, A.G. Dixon, Effect of the wall Nusselt number on the simulation of catalytic fixed bed reactors, Catal. Today 35 (1997) 435-442.
[78] O.A. Sergeev, A.G. Shashkov, A.S. Umanskii, Thermophysical properties of quartz glass, J. Eng. Phys. Thermophys. 43 (1982) 1375-1383.
[79] S.W. Churchill, H.H. Chu, Correlating equations for laminar and turbulent free convection from a horizontal cylinder, Int. J. Heat and Mass Tran. 18 (1975) 1049-1053.
[80] A.F. Mills, Heat transfer second edition, Prentice-Hall, New Jersey, 1999.
[81] V. Gnielinski, New equations for heat and mass transfer in turbulent pipe and channel flow, Int. Chem. Eng. 16 (1976) 359-368.
[82] J.P. Holman, Heat transfer 9th edition, McGraw-Hill, Inc, New York, Boston, 2002.
[83] Y.S. Touloukian, R.K. Kirby, E.R. Taylor, T.Y.R. Lee, Thermophysical properties of matter, The TPRC Data Series, Purdue University, 1977.
[84] R. Morrell, Handbook of properties of technical and engineering ceramics, Stationery Office Books, London, 1987.
[85] G.J. Janz, Molten salts handbook, Elsevier, New York, 1967.
[86] Dynalene Molten Salts, Dynalene, Inc., https://www.dynalene.com/Molten-Salts-s/1831.htm, 2016.
[87] J. Gao, Y. Wang, Y. Ping, D. Hu, G. Xu, F. Gu, F. Su, A thermodynamic analysis of methanation reactions of carbon oxides for the production of synthetic natural gas, RSC Adv. 2 (2012) 2358.

# Appendix

## A. 1 Dimensionless model

$$\frac{\partial u_{CO_2}}{\partial \tau}=\left(\frac{1}{Pe_m}\right)\frac{\partial^2 u_{CO_2}}{\partial \xi^2}-\frac{\partial u_{CO_2}}{\partial \xi}+Da(\hat{k}_2\ f_2\eta_2+\hat{k}_3\ f_3\eta_3)$$

$$\frac{\partial u_{H_2}}{\partial \tau}=\left(\frac{1}{Pe_m}\right)\frac{\partial^2 u_{H_2}}{\partial \xi^2}-\frac{\partial u_{H_2}}{\partial \xi}+Da(3\hat{k}_1\ f_1\eta_1+\hat{k}_2\ f_2\eta_2+4\hat{k}_3\ f_3\eta_3)$$

$$\frac{\partial u_{CO}}{\partial \tau}=\left(\frac{1}{Pe_m}\right)\frac{\partial^2 u_{CO}}{\partial \xi^2}-\frac{\partial u_{CO}}{\partial \xi}+Da(\hat{k}_1\ f_1\eta_1-\hat{k}_2\ f_2\eta_2)$$

$$\frac{\partial u_{H_2O}}{\partial \tau}=\left(\frac{1}{Pe_m}\right)\frac{\partial^2 u_{H_2O}}{\partial \xi^2}-\frac{\partial u_{H_2O}}{\partial \xi}+Da(-\hat{k}_1\ f_1\eta_1-\hat{k}_2\ f_2\eta_2-2\hat{k}_3\ f_3\eta_3)$$

$$\frac{\partial u_{CH_4}}{\partial \tau}=\left(\frac{1}{Pe_m}\right)\frac{\partial^2 u_{CH_4}}{\partial \xi^2}-\frac{\partial u_{CH_4}}{\partial \xi}+Da(-\hat{k}_1\ f_1\eta_1-\hat{k}_3\ f_3\eta_3)$$

$$\sigma\frac{\partial \theta}{\partial \tau}=\frac{1}{Pe_r}\frac{\partial^2 \theta}{\partial \xi^2}-\frac{\partial \theta}{\partial \xi}+\beta Da[k_1 f_1\left(\Delta H_1\right)\eta_1+k_2 f_2\left(\Delta H_2\right)\eta_2+k_3 f_3\left(\Delta H_3\right)\eta_3]-nSt_{r1}\left(\theta-\theta_c\right)-St_{r2}\left(\theta-\theta_e\right)$$

$$\frac{\partial \theta_c}{\partial \tau}=\frac{1}{Pe_c}\frac{\partial^2 \theta_c}{\partial \xi^2}-\frac{\partial \theta_c}{\partial \xi}-nSt_c\left(\theta_c-\theta\right)$$

$$P=1-J\left(150S\hat{v}_g+1.75\,\mathrm{Re}\hat{v}_g^2\right)\xi$$

*Dimensionless parameters:*

$$\theta=\frac{T}{T_f};\qquad \theta_c=\frac{T_c}{T_f};\qquad \theta_e=\frac{T_e}{T_f};\qquad \theta_{cf}=\frac{T_{cf}}{T_f};\qquad \tau=\frac{t}{L/v_g};\qquad \xi=\frac{z}{L};\qquad u_t=\frac{C_t}{C_{tf}}$$

$$P=\frac{P_t}{P_{tf}};\qquad P=\frac{P_t}{P_{tf}};\qquad u_f=\frac{C_f}{C_{tf}};\qquad \hat{v}_g=\frac{v_g}{v_{gf}};\qquad \left(\Delta H_j\right)=\frac{-\Delta H_j}{-\Delta H_1};$$

$$f_1=\left(\frac{y_{CH_4}y_{H_2O}}{y_{H_2}^{2.5}}-\frac{y_{H_2}^{0.5}y_{CO}}{\hat{K}_{eq1}}\right)/\left(\hat{DEN}\right)^2;\qquad f_2=\left(\frac{y_{CO}y_{H_2O}}{y_{H_2}}-\frac{y_{CO_2}}{K_{eq2}}\right)/\left(\hat{DEN}\right)^2;$$

$$f_3=\left(\frac{y_{CH_4}y_{H_2O}^2}{y_{H_2}^{3.5}}-\frac{y_{H_2}^{0.5}y_{CO2}}{\hat{K}_{eq3}}\right)/\left(\hat{DEN}\right)^2;\qquad \hat{DEN}=1+\hat{K}_{CO}\,y_{CO}+\hat{K}_{H_2}\,y_{H_2}+\hat{K}_{CH_4}\,y_{CH_4}+\frac{K_{H_2O}P_{H_2O}}{P_{H_2}};$$

$$k_{1ad} = A_1 \exp\left(-\gamma_{1ad}\right);\ \gamma_{1ad} = \frac{Ea_1}{RT_{ad}};\ k_1 = \frac{k_1}{k_{1ad}};\ k_2 = \frac{P^{1.5}k_2}{k_{1ad}};\ k_3 = \frac{k_3}{k_{1ad}};\ K_{eq1} = \frac{K_{eq1}}{P_t^2};\ K_{eq3} = \frac{K_{eq3}}{P_t^2};$$

$$\sigma = \frac{\varepsilon\rho_g C_{pg} + (1-\varepsilon)\rho_s C_{ps}}{\varepsilon\rho_g C_{pg}};\quad \beta = \frac{(-\Delta H_1)}{C_{pg}T_f u_t};\quad Da = \frac{\rho_s(1-\varepsilon)k_{1ad}}{P_t^{0.5}(v_g / L)\varepsilon C_{tf}};\quad \mathrm{Re} = \frac{L\rho_{gf}v_{gf}}{\mu_g};$$

$$Pe_m = \frac{\varepsilon v_g L}{D_{ae}};\quad Pe_r = \frac{Lv_g\varepsilon\rho_g C_{pg}}{k_{ae}};\quad Pe_c = \frac{Lv_c\rho_c C_{pc}}{\lambda_c};\quad J = \frac{v_{gf}\mu_g(1-\varepsilon)}{P_{tf}\varepsilon^3 d_p};\quad S = \frac{(1-\varepsilon)L}{d_p};$$

$$St_c = \frac{U_{cw}a_{c,he}}{\rho_c C_{pc} v_c / L};\quad St_{r1} = \frac{U_{cw}a_{v,he}}{\varepsilon\rho_g C_{pg} v_g / L};\quad St_{r2} = \frac{U_{rw}a_{v,hl}}{\varepsilon\rho_g C_{pg} v_g / L}$$

*Dimensionless initial and boundary conditions:*

$$\xi = 0:\ -\frac{1}{Pe_m}\frac{\partial u_i}{\partial \xi} = (u_{fi} - u_i);\qquad \xi = 1:\ \frac{\partial u_i}{\partial \xi} = 0;\qquad \tau = 0:\ u_i(0,\xi) = u_{\mathrm{i,int}};$$

$$-\frac{1}{Pe_r}\frac{\partial \theta}{\partial \xi} = (1-\theta);\qquad \frac{\partial \theta}{\partial \xi} = 0;\qquad \theta(0,\xi) = \theta_{\mathrm{int}};$$

$$-\frac{1}{Pe_c}\frac{\partial \theta_c}{\partial \xi} = (\theta_{cf} - \theta_c)\qquad \frac{\partial \theta_c}{\partial \xi} = 0\qquad \theta_c(0,\xi) = \theta_{c,\mathrm{int}}$$

## A.2 Kinetic data

$$K_{1,eq} = 1.198\times10^{17}\exp(-\frac{26830}{T})\ \mathrm{kPa}^2$$

$$K_{2,eq} = 1.767\times10^{-2}\exp(\frac{4400}{T})\ \mathrm{Dimensionless}$$

$$K_{3,eq} = 2.117\times10^{15}\exp(-\frac{22430}{T})\ \mathrm{kPa}^2$$

**Table. A. 1.** Reaction kinetic parameters

| Constant | $A_j$ and $B_i$ | Ea and ΔH (kJ/mol) |
|---|---|---|
| $k_1$ | $9.49\times10^{15}$ | 240.1 |
| $k_2$ | $4.39\times10^{6}$ | 67.13 |
| $k_3$ | $2.29\times10^{15}$ | 243.90 |
| $K_{CO}$ | $8.23\times10^{-5}$ | -70.65 |
| $K_{CH4}$ | $6.65\times10^{-4}$ | -38.82 |
| $K_{H2O}$ | $1.77\times10^{5}$ | 88.68 |

| | | |
|---|---|---|
| $K_{H2}$ | $6.12\times10^{-9}$ | -82.90 |

*The units in the table are as follows: $k_1$, $k_3$ = kmol·bar$^{0.5}$/kg cat·h; $k_2$=kmol/kg cat·h·bar; $K_{CH4}$, $K_{CO}$, $K_{H2}$ = bar$^{-1}$.*

**Table. A. 2.** Catalyst deactivation kinetic parameters

| $K_{d0}$ | $E_d$ | α | β |
|---|---|---|---|
| $2.35\times10^{8}$ | $1.74\times10^{5}$ | 1.8 | -1.9 |

## A.3 Regression equations of thermophysical properties

*Gas components[83]:*

*Heat capacity (kJ/mol-K):*

$C_{p,CO_2} = -2\times10^{-8}T^2 - 5\times10^{-5}T + 0.0256$;

$C_{p,H_2} = 3\times10^{-9}T^2 - 2\times10^{-6}T + 0.0297$;

$C_{p,CO} = 10^{-8}T^2 - 7\times10^{-6}T + 0.0301$;

$C_{p,H_2O} = 10^{-8}T^2 - 5\times10^{-6}T + 0.0356$;

$C_{p,CH_4} = 0.03\ln(T) - 0.1394$

*Thermal Conductivity (kW/m-K):*

$\lambda_{CO_2} = 8\times10^{-8}T - 4\times10^{-6}$ ;

$\lambda_{H_2} = 5\times10^{-7}T + 4\times10^{-5}$;

$\lambda_{CO} = 6\times10^{-8}T + 8\times10^{-6}$;

$\lambda_{H_2O} = 10^{-7}T - 2\times10^{-5}$;

$\lambda_{CH_4} = 2\times10^{-7}T - 3\times10^{-5}$

*Viscosity (Pa s):*

$\mu_{CO_2} = 4\times10^{-8}T + 6\times10^{-6}$; $\mu_{H_2} = 2\times10^{-8}T + 5\times10^{-6}$; $\mu_{CO} = 4\times10^{-8}T + 7\times10^{-6}$

$\mu_{H_2O} = 4\times10^{-8}T - 3\times10^{-6}$; $\mu_{CH_4} = 3\times10^{-8}T + 4\times10^{-6}$

*Alumina support[84]:*

*Heat Capacity (kJ/kg-K):* $C_{ps} = 1.0446 + 1.742\times10^{-4}T - 2.796\times10^{4}T^{-2}$ ;

*Thermal Conductivity (kW/m-K):* $\lambda_s = 5.5\times10^{-3} + 34.5\times10^{-3}\exp[-0.0033\times(T-273)]$;

*Density (kg/m$^3$):* $\rho_s = 3.85\times10^{3}$

*Solar molten salt[86]:*

*Heat Capacity (kJ/kg-K):* $C_{pc} = 2\times10^{-4}T + 1.2738$ ;

*Thermal Conductivity (kW/m-K):* $\lambda_c = 2\times10^{-7}T - 4\times10^{-4}$ ;

*Density (kg/m$^3$):* $\rho_c = -0.5572T + 2219.1$